Organic Scintillation Detectors for Spectroscopic Radiation Portal Monitors

by
Marc Gerrit Paff

A dissertation submitted in partial fulfillment
of the requirements for the degree of
Doctor of Philosophy
(Nuclear Engineering and Radiological Sciences)
in the University of Michigan
2017

Doctoral Committee:

Professor Sara A. Pozzi, Chair
Associate Professor Christine A. Aidala
Associate Research Scientist Shaun D. Clarke
Dr. Richard T. Kouzes, Pacific Northwest National Laboratory
Assistant Professor Martha M. Matuszak

Marc G. Paff

mpaff@umich.edu

ORCID iD: 0000-0002-4554-9916

Acknowledgements

There are numerous people I would like to thank for guiding me through graduate school. Thank you Dr. Robert Bean and Dr. Richard Metcalf for introducing me to the fields of nuclear safeguards and security by offering me two amazing summer internships at the Idaho National Laboratory when I was just a young nuclear engineering undergraduate student at Purdue University. Thank you to the two of you for recommending Professor Sara Pozzi's group at University of Michigan. Thank you to Scott Ambers and Dr. Jennifer Dolan for chatting with me at the 2010 INMM Annual Meeting in Baltimore about what it was like working in Professor Pozzi's research group. Professor Pozzi, thank you for all of your guidance and the many opportunities you have opened to me.

I also thank Marc Ruch, Dr. Alexis Poitrasson-Riviere and Athena Sagadevan and everybody else in the Detection for Nuclear Nonproliferation Group for their contributions to this radiation portal monitor research project and the friendships that will last well past our joint years in graduate school. I also thank Gustav Eklund, Carlos Carrapico, Paolo Peerani, Bent Pedersen and all of my other friends at the European Commission Joint Research Centre in Ispra, Italy. My time spent at the JRC for my practicum and the SCINTILLA benchmark measurements were definite highlights of my years in graduate school.

Thank you to the National Nuclear Security Administration for supporting my research through the Nuclear Nonproliferation International Safeguards fellowship. The name of the fellowship might be a tongue twister, but Craig Williamson, Nancy Carder and Nicole Huchet at SCUREF have been such a fantastic source of support throughout the years.

Finally, I would like to thank Sabrina Hadinoto, Kirsten Paff, Diane Paff, Joseph Morris, Sandy Morris and Beth Morris for their constant and unwavering moral support in my academic endeavors. Grandpa, I know how proud you always were to have a new generation of engineers in the family. This dissertation is dedicated to you and the love of science and engineering you instilled into your grandchildren.

This research was performed under appointment to the Nuclear Nonproliferation International Safeguards Fellowship Program sponsored by the Nation Nuclear Security Administration's Office of International Nuclear Safeguards (NA-241).

It is also funded in-part by the Consortium for Verification Technology under Department of Energy National Nuclear Security Administration award number DE-NA0002534.

Table of Contents

Acknowledgements i

List of Figures vi

List of Tables xiv

List of Appendices xix

List of Abbreviations xx

Abstract xxiii

Chapter 1 Introduction 1

1.1. Problem Description 4

1.2. Contributions from this Work 8

Chapter 2 Gamma-Ray Photon and Neutron Detection for RPMs 10

2.1. Inorganic Scintillation Detectors 10

2.2. Organic Scintillation Detectors 12

2.2.1. Pulse-Shape Discrimination via the Charge Integration Method 15

2.2.2. Types of organic scintillation detectors used 19

2.2.3 Digital acquisition systems 21

2.3. ^{3}He neutron proportional counters 24

Chapter 3 Modeling and Designing RPMs with MCNPX-PoliMi and Benchtop Experiments 27

3.1. Modeling RPMs with MCNPX-PoliMi 27

3.1.1. The Particle Transport Code MCNPX-PoliMi 27

3.1.2. Modeling Light Output for Organic Scintillators 29

3.1.3. Modeling Moving Sources with MCNPX-PoliMi 30

3.2. Establishing System False Alarm Rate and Minimum Detectable Activity Using Receiver Operating Characteristic Curves 32

3.2.1. What are Receiver Operating Characteristics Curves? 32

3.2.2. Experimental Setup for Comparing Different Detectors for RPM Suitability 34

3.2.3. Receiver Operating Characteristics Curve Results for Comparing Different Organic Liquid Scintillation Detector Shapes and Volumes 35

3.3. Designing a Complete RPM System Architecture 40
Chapter 4 Testing RPM Prototypes Under Real-World Conditions 43
4.1. The European Commission SCINTILLA RPM Testbed Facility 43
4.2. RPM False Alarm Tests 45
4.3. RPM Neutron Alarm Tests 46
4.3.1. Pedestrian RPM Neutron Alarm Results 46
4.3.2. Vehicle RPM Neutron Alarm Results 52
4.4. RPM Gamma-Ray Photon Alarm Tests 53
4.4.1. Pedestrian RPM Gamma-Ray Photon Alarm Results 53
4.4.2. Vehicle RPM Gamma-Ray Photon Alarm Results 58
Chapter 5 Reducing Nuisance Alarms Through On-The-Fly Radionuclide Identification 60
5.1. Challenges for On-The-Fly Identification 60
5.2. Identification Using Least Squares Comparison with Modified PHDs 62
5.3. Identification Using Least Squares Comparison with Cumulative Distribution Functions 67
5.4. Adding Medical Isotopes to the Mix 72
5.5. Identification Using Power Spectral Density and Spectral Angular Mapping 75
5.6 Comparison of radionuclide identification methods using F-scores 81
5.7 Identifying Multiple Isotopes Simultaneously 83
Chapter 6. Summary and Conclusions 91
Appendices 95
References 100

List of Figures

Fig. 2-1. (a) Examples of ^{137}Cs PHDs obtained with a variety of organic liquid scintillation detectors such as liquids (EJ309), plastics (BB3) and crystals (stilbene). Pulse heights are still in digitizer units of volts, and no energy calibration has taken part yet. (b) MCNP6 simulated un-broadened and resolution broadened PHDs for measurements of ^{137}Cs with a 25 cm by 25 cm by 10 cm BC501A liquid organic scintillation detector reveal that a calibration value of 96% of the Compton edge peak should be set to equal the 478 keV Compton edge. This conversion is used to convert the measured ^{137}Cs PHD from volts to light output in keVee.....14

Fig. 2-2. (a) On the left is one of the first measurements showing increasing delayed scintillation light component with increasing mass (stopping power) of incident radiation on organic scintillator (stilbene) (Bollinger & Thomas, 1961); (b) On the right, typical pulses for EJ309 organic liquid scintillation detector showing increased delayed light component for neutron vs gamma-ray photon interaction, thus forming basis for PSD.....15

Fig. 2-3. Energy levels for organic molecule with π-electron structure with singlet and triplet excited states. The de-excitation of these states (fluorescence and phosphoresence) cause the prompt and delayed scintillation light components in organic scintillators (Birks, 1964). 17

Fig. 2-4. Pulse shape discrimination for measurement of ^{252}Cf with 7.62 cm diameter EJ309 liquid (Marc Gerrit Paff et al., 2015)(Marc G Paff, Clarke, & Pozzi, 2016). 17

Fig. 2-5. Histogram of tail-to-total integral ratio for ^{252}Cf data acquired with 25 cm by 25 cm by 10 cm BC501A organic liquid scintillation detector. Fitted Gaussian distributions for gamma-ray photons (left, blue) and neutrons (right, yellow) are used for calculating FOM using equation (2-7) (Marc G Paff et al., 2016). 19

Fig. 2-6. Example of standard composition of an organic scintillation detector coupled to a PMT. Detector cell could be a crystal (stilbene), plastic (BB3, EJ299-33,) or, as in this cases, a liquid cell (EJ309). 21

Fig. 2-7. Examples of the detectors used in measurements in this dissertation including from left to right: 7.62 cm ∅ EJ309 organic liquid scintillation detector, 12.7 cm ∅ EJ309 organic liquid scintillation detector, 25 cm by 25 cm by 10 cm BC501A organic liquid scintillation detector, 7.62 cm ∅ stilbene crystal couple to PMT (7.62 cm ∅ BB3 plastic scintillator looks identical when wrapped and coupled to PMT). Pictures are not to scale relative to each other. 21

Fig. 2-8. Block diagram of a multi-detector setup, where the PMTs are powered by a high voltage (HV) power supply. Detector anode output signals are fed to a digitizer, and packets of digitized pulses with time stamps are fed via USB link or optical link to a data acquisition system (DAQ). Pulses are processed on the DAQ using PSD to determine parameters such as neutron and gamma-ray photon count rates or PHDs or any other user desired information. 22

Fig. 2-9. CAEN V1730 (top) and DT5720 (bottom) digitizers. 23

Fig. 2-10. Opened ^{3}He RPM containing three ^{3}He proportional tubes embedded in HDPE. 26

Fig. 3-1. (a) Side and (b) front view of an eight 7.62 cm diameter EJ309 cylindrical liquid scintillator RPM modeled in MCNPX-PoliMi and later built as a prototype (c). A 0.59 MBq 137Cs line source is situated 75 cm parallel to RPM front face. The source is assumed to be moving at 1.2 m/s, and the length of the line source therefore represents the simulated measurement time [61].. 31

Fig. 3-2. (a) Simulated RPM gamma-ray photon count rates for setup from figure 3-1 for a range of different measurement times simulated via changing the length of the line source. (b) Comparison count rates of a static versus a dynamic source measurement to establish that a 3 s measurement for a source moving at 1.2 m/s can be reproduced in the laboratory with a 2 s static source measurement [61].. 32

Fig. 3-3. Example of the probability of an RPM detecting N neutrons per second from a background and some MDA neutron Poisson distributions. For a user defined alarm threshold neutron count rate, t_n, the true negative rate, TN, is the probability of correctly not neutron alarming on neutron background, whereas the false negative rate, FN, is the probability of not alarming on the MDA neutron source. The false positive rate, FP, the false alarm rate probability on neutron background, whereas the true positive rate, TP, is the correct alarm rate on the neutron MDA source. [45]. 33

Fig. 3-4. Example of an ROC curve for the sample background and MDA source neutron Poisson distributions from Figure 3-3 [45]. 34

Fig. 3-5. (a) ^{3}He RPM, (b) 7.62 cm Ø cylindrical EJ309, (c) 12.7 cm Ø cylindrical EJ309, and (d) 25 cm x 25 cm x 10 cm BC501A; 110,000 n/s ^{252}Cf + 10 cm HDPE at 100 cm from detector front face [45]. 35

Fig. 3-6. Measured and MCNPX-PoliMi simulated neutron pulse height distributions for moderated 252Cf measurement with 25x25x10 cm BC501A shown in Figure 3-5d[45]. 36

Fig. 3-7. Fractional difference plot for measured and simulated PHDs from Figure 3-6, showing 10-15 percent agreement between measurement and simulation at light output over 300 keVee [45]. 37

Fig. 3-8. ROC curve comparison of three different organic liquid scintillators and a ^{3}He RPM for the moderated 252Cf setup from Figure 3-5 [45]. 38

Fig. 3-9. ROC curve comparison of different number of 7.62 cm diameter EJ309 cylindrical active volume organic scintillation detectors for the moderated 252Cf setup from Figure 3-5b [45]. A 1 in 10,000 desired neutron false alarm rate is indicated by the dashed vertical black line [34]. 39

Fig. 3-10. ROC curve comparison of different number of 12.7 cm diameter EJ309 cylindrical active volume organic scintillation detectors for the moderated 252Cf setup from Figure 3-5c [45]. A 1 in 10,000 desired neutron false alarm rate is indicated by the dashed vertical black line [34]. 39

Fig. 3-11. (a) Pedestrian RPM consisting of eight 7.62 cm diameter cylindrical volume EJ309 organic liquid scintillation detectors; (b) vehicle RPM consisting of four 12.7 cm diameter EJ309 cylindrical active volume organic scintillation detectors and one 25x25x10 cm^3 BC501A liquid detector. Both RPMs used two web-cameras and motion detection software as a makeshift occupancy sensor [36,37]. 41

Fig. 3-12. (a) Example of a trigger picture captured by the vehicle RPM occupancy sensor [36]. (b) The motion detection software [63] will signal that motion has been detected if the image in the white portion of this mask changes. Separate masks are used to detect motion approaching from the left and right of the RPM. 42

Fig. 4-1. RPM testing facility at European Commission JRC Ispra, Italy. Left: 2nd SCINTILLA benchmark campaign in February 2014. Right: Electric rail cart system. (Photo credit: JRC Ispra). 44

Fig. 4-2. Histograms of measured (a) neutrons and (b) gamma-ray photons in 2,739 three second measurements for the false alarm test for the pedestrian RPM during the 2nd SCINTILLA benchmark in February 2014 at the European Commission JRC in Ispra, Italy. The alarm thresholds shown are set five standard deviations above the mean background count rates. 46

Fig. 4-3. Histograms of measured neutrons for 30 three second measurements of an unshielded 20,000 n/s ^{252}Cf moving at 1.2 m/s (red) or 3 m/s (blue). These histograms correspond to the data from folders 2 (red) and 3 (blue) in Table B-1 in Appendix B. These measurements were part of the pedestrian RPM neutron alarm testing during the 2nd SCINTILLA benchmark in February 2014 at the European Commission JRC in Ispra, Italy [35,37]. The 9 neutrons alarm threshold shown is set five standard deviations above the mean background count rate. 48

Fig. 4-4. Histograms of measured neutrons for 30 three second measurements of a 20,000 n/s ^{252}Cf moving at 1.2 m/s past the pedestrian RPM. Histograms are shown for tests with different amounts of HDPE shielding around the neutron source: (a) unshielded, (b) 4 cm thick HDPE, and (c) 8 cm thick HDPE. These histograms correspond to the data from folders (a) 2, (b) 16, and (c) 10 in Table B-1 in Appendix B. These measurements were

part of the pedestrian RPM neutron alarm testing during the 2nd SCINTILLA benchmark in February 2014 at the European Commission JRC in Ispra, Italy [35,37]. The 9 neutrons alarm threshold shown is set five standard deviations above the mean background count rate. 49

Fig. 4-5. Histograms of measured neutrons for 30 three second measurements of a ^{252}Cf source from the pedestrian RPM neutron alarm testing during the 2nd SCINTILLA benchmark in February 2014 at the European Commission JRC in Ispra, Italy [35,37]. All three cases involve test scenarios well beyond ANSI standard neutron alarming test conditions [34] and a majority of runs resulted in neutron counts below the 9 neutrons alarm threshold which is set five standard deviations above the mean neutron background count rate. The three test cases shown are: (a) 20,000 n/s ^{252}Cf with 8 cm HDPE shielding and moving at 2.2 m/s, (b) 10,000 n/s ^{252}Cf with 8 cm HDPE shielding and moving at 1.2 m/s, and (c) 10,000 n/s ^{252}Cf with 8 cm HDPE shielding and moving at 2.2 m/s. These histograms correspond to the data from folders (a) 9, (b) 12, and (c) 11 in Table B-1 in Appendix B. 51

Fig. 4-6. Histograms of measured gamma-ray photons for 30 three second measurements of a 6.6 g sample of WGPu moving at 1.2 m/s past the pedestrian RPM. Histograms are shown for different test scenarios: (a) 1.2 m/s source transit speed; source unshielded, (b) 2.2 m/s source transit speed; source unshielded, and (c) 2.2 m/s source transit speed; source shielded with 1 cm steel. These histograms correspond to the data from folders (a) 21, (b) 22, and (c) 23 in Table B-1 in Appendix B. These measurements were part of the pedestrian RPM gamma-ray photon alarm testing during the 2nd SCINTILLA benchmark in February 2014 at the European Commission JRC in Ispra, Italy [35,37]. The 3,856 gamma-ray photons alarm threshold shown is set five standard deviations above the mean background count rate. 56

Fig. 4-7. Histograms of measured gamma-ray photons for 30 three second measurements with the pedestrian RPM of: (a) 51 g sample of HEU moving at 1.2 m/s, (b) 2,220 kBq ^{241}Am moving at 1.2 m/s, and (c) 2,220 kBq ^{241}Am moving at 2.2 m/s. These histograms correspond to the data from folders (a) 40, (b) 35, and (c) 34 in Table B-1 in Appendix B. These measurements were part of the pedestrian RPM gamma-ray photon alarm testing during the 2nd SCINTILLA benchmark in February 2014 at the European Commission

JRC in Ispra, Italy [35,37]. The 3,856 gamma-ray photons alarm threshold shown is set five standard deviations above the mean background count rate. 57

Fig. 5-1. Example of a gamma-ray photon PHD of 500 g metal WGPu sample (6% ^{240}Pu) acquired with coaxial HPGe detector [74,75]. Peaks without isotope label stem directly from ^{239}Pu decay, while other peaks stem from other isotopes always found in WGPu, such as ^{241}Am as well as other isotopes of plutonium. 61

Fig. 5-2. Gamma-ray photon PHDs before (blue squares) and after (red circles) background subtraction for three second dynamic measurement of 6.6 g WGPu with pedestrian RPM during 2nd SCINTILLA benchmark at JRC Ispra, Italy, in February 2014 [39,76]. Such a background subtracted PHD would provide the raw basis for any subsequent on-the-fly radionuclide identification attempts [39,76]. 62

Fig. 5-3. High (a) and low (b) gain matrices used as library spectra for on-the-fly radionuclide identification with the pedestrian RPM at the 2nd SCINTILLA benchmark at the JRC Ispra, Italy, in February 2014. Measurement times for all PHDs exceeded 600 s. Of the eight detectors, five used the high gain setting and three used the low gain setting [35,71]. 63

Fig. 5-4. PHD modification steps for a three second ^{57}Co measurement with pedestrian RPM at February 2014 SCINTILLA benchmark at JRC Ispra, Italy. All PHDs are subdivided into 200 bins. See Figure 5-2a for energy scale. (a) Background corrected three second PHD (blue) versus library spectrum of ^{57}Co (red) from Figure 5-2a; (b) PHDs after noise suppression has been applied to zero out negative and low count rate bins; (c) PHDs after bin coarsening by a factor of two [35,71]. 66

Fig. 5-5. Average dynamically measured PHD for WGPu and WGPu library PHD for pedestrian RPM at 2nd SCINTILLA benchmark at JRC Ispra, Italy, in February 2014. These two PHDs do not match well, explaining why WGPu was never identified correctly [35]. ...67

Fig. 5-6. (a) High-gain modified CDF library matrix for RPM radionuclide identification, (b) low-gain modified CDF library matrix for radionuclide identification [35,62]. 70

Fig. 5-7. High-gain modified CDF library matrix for RPM radionuclide identification with y(n) of dynamic measurements of (a) ^{133}Ba and (b) ^{137}Cs with pedestrian RPM at 2nd SCINTILLA benchmark at JRC Ispra, Italy, in February 2014 [39,66,77]. 71

Fig. 5-8. Measuring medical isotopes with the pedestrian RPM at the University of Michigan's C.S. Mott Children's Hospital in December 2013. 72

Fig. 5-9. June 2016 setup for measuring medical isotopes at University of Michigan's C.S. Mott Children's Hospital using: (a) a 7.6 cm diameter cylindrical volume EJ309 organic liquid scintillation detector, (b) a 5.1 cm diameter and 5.1 cm height cylindrical volume stilbene crystal from Inrad Optics, a 12.7 cm diameter cylindrical volume EJ309 organic liquid scintillation detector (d) an experimental 5.1 cm diameter and 5.1 cm height cylindrical volume plastic scintillator name BB3 from Radiation Monitoring Devices. 73

Fig. 5-10. 7-8 μCi medical isotope samples measured at the University of Michigan's C.S. Mott Children's Hospital in June 2016. From left to right: ^{111}In, ^{18}F, ^{67}Ga, ^{123}I, ^{201}Tl, ^{99m}Tc, and ^{201}Tl. Labeled activities are desired activities, which at times differed by 1 μCi from the actual activities listed on separate calibration source sheets provided by the hospital. 74

Fig. 5-11. High-gain modified CDF library matrix, including medical isotopes, for RPM radionuclide identification with y(n) of measurement of 131I with pedestrian RPM detector at University of Michigan's C.S. Mott Children's Hospital in June 2016 [77]. .75

Fig. 5-12. Examples of (a) CDF, (b) FFT, and (c) power spectral density for signal from a three second measurement of ^{137}Cs with the pedestrian RPM at the SCINTILLA benchmark at JRC Ispra, Italy, in February 2014. 77

Fig. 5-13. Example of SAM angle being computed between a RPM measured CDF and reference CDF of ^{137}Cs. This process would be repeated for all data points in the measured spectrum. SAM values would then be computed for comparisons with all reference CDFs representing all library radionuclides. The overall smallest SAM value gives the likeliest radionuclide to cause the measured CDF.....78

Fig. 5-14. Non-source inputs for testing the radionuclide identification algorithms. Test inputs include the CDFs of a gamma ray PHD background measurement, a linear function

through the origin, and a square function through the origin. The α SAM values resulting from these inputs are listed in Table 5-4 [77]. 80

Fig. 5-15. Library CDFs and example of RPM data consisting of ^{67}Ga and ^{99m}Tc mixed in a 1:1 ratio. 86

Fig. 5-16. Average isotope fraction coefficients, c_i, computed for an LSU algorithm for un-mixing pedestrian RPM data consisting of ^{67}Ga and ^{99m}Tc mixed in a 1:1 ratio. The averages and standard deviations of coefficients computed for each possible isotope use 30 three second measurement data sets as inputs. Inputs are PHDs. 87

Fig. 5-17. Library CDFs and example of RPM data consisting of ^{137}Cs, WGPu, and ^{99m}Tc mixed in a 1:3:1 ratio. 90

Fig. 5-18. Average isotope fraction coefficients, c_i, computed for an LSU algorithm for un-mixing pedestrian RPM data consisting of ^{137}Cs, WGPu, and ^{99m}Tc mixed in a 1:3:1 ratio. The averages and standard deviations of coefficients computed for each possible isotope use 30 three second measurement data sets as inputs. Inputs are PHDs. 90

Fig. A-1. Example of an XML file output for a single RPM occupancy for the pedestrian RPM tested at the 2nd SCINTILLA benchmark at the European Commission JRC in Ispra, Italy, in February 2014. The standardized XML file contains vital information, including a time stamp, gross neutron and gamma-ray photon counts and count rates, alarm type, and radionuclide identification result in the case of gamma alarms. 95

List of Tables

Table 2-1. Manufacturer and model numbers for organic scintillation detectors used in measurements for this dissertation.. 20

Table 2-2. Properties of various organic scintillators by the listed manufacturer [38,47–51].....20

Table 3-1. Measured and simulated neutron count rates for moderated ^{252}Cf setup shown in Figure 3-5 [45,62]... 36

Table 3-2. Probabilities of a true alarm as a function of number of detectors and assuming a 1 in 10,000 false alarm rate for a 2 s measurement of a 20,000 n/s ^{252}Cf source placed 100 cm from the detector front face and shielded by 10 cm of HDPE, as show in the setups in Figure 3-5 [45]. 40

Table 4-1. Gamma-ray photon source activities for ANSI recommended sources as well as activities used at the two SCINTILLA RPM benchmark experiments at the JRC Ispra in February and November 2014. 45

Table 4-2. Highlights of February 2014 2nd SCINTILLA benchmark pedestrian RPM neutron alarm test results [35,37] for ANSI [34] and beyond ANSI standard test conditions using a 10,000 n/s or 20,000 n/s ^{252}Cf source with 1 cm steel and 0.5 cm lead shielding. Underlined values indicate parameters set at beyond ANSI standard for pedestrian RPM. Full neutron alarm dataset may be found in Table B-1 in Appendix B.. 47

Table 4-3. Results of November 2014 3rd SCINTILLA benchmark vehicle RPM neutron alarm test results [36,69] for ANSI [34] and beyond ANSI standard test conditions using 7,000 n/s, 13,000 n/s, or 20,000 n/s ^{252}Cf sources with 1 cm steel and 0.5 cm lead shielding. Underlined values indicate parameters set at beyond ANSI standard for vehicle RPM... 53

Table 4-4. Results of February 2014 2nd SCINTILLA benchmark pedestrian RPM gamma-ray photon alarm test results [36,69] for ANSI [34] and beyond ANSI standard test

conditions using a variety of gamma-ray photon sources, including SNM. More detailed information on these trials can also be found in Table B-1 in Appendix B folders 17-40....54

Table 4-5. Results of November 2014 3rd SCINTILLA benchmark vehicle RPM gamma-ray photon alarm test results [36,69] for ANSI [34] and beyond ANSI standard test conditions using a variety of gamma-ray photon sources.....59

Table 5-1. Correct radionuclide identification using the modified least squares method out of 30 trials for different isotopes measured with the pedestrian RPM at the 2nd SCINTILLA benchmark at the JRC Ispra, Italy, in February 2014 [35,71]. Identification results are shown for both high- and low-gain detector sets, and for the different PHD modification steps outlined in Figure 5-3.....67

Table 5-2. Comparison of correct radionuclide identifications out of 30 trials using the modified least squares method versus the CDF method for different isotopes measured with the pedestrian RPM at the 2nd SCINTILLA benchmark at the JRC Ispra, Italy, in February 2014 [35,71]. A slightly higher pulse height threshold of 0.06 V vs 0.03 V was used for the ^{57}Co results.....72

Table 5-3. List of medical isotopes measured at University of Michigan's C.S. Mott Children's Hospital in June 2016 and their respective radioactive half-lives in hours, and their activities at time of sample calibration and at time we measured them.....74

Table 5-4. Average and standard deviations of the SAM α values computed for the correct isotope for thirty datasets for each of the 13 tested radionuclides. The SNM and industrial radionuclide datasets come from the datasets from Table B-1 listed previously in this section. The medical datasets consist of 1,000 net detected pulses from the respective medical sources. Examples of full datasets showing SAM α values for all 30 datasets for one isotope for all possible radionuclide identification options are given in Tables B-2 and B-3 in Appendix B 79

Table 5-5. Average and standard deviations of the SAM α values computed for the correct isotope for thirty datasets for each of the 12 tested radionuclides. The SNM and industrial radionuclide datasets come from the following datasets from Table B-1 in Appendix B:

folders 17, 21, 27,31, 34, 36. All of these tests are the same as those used for Table 5-4 except that the source transit speed is increased from 1.2 m/s to 2.2 m/s . The medical datasets consist of 400 net detected pulses from the respective medical sources, which is at the limit of detection for the pedestrian RPM for the background conditions and associated gamma alarm threshold used at the JRC Ispra. 80

Table 5-6. SAM α-values computed for the test cases shown in Figure 5-14. As none of these inputs should match any of the reference spectra, the α SAM values should be larger than, for example, the average α SAM value of 0.003±0.000 for positive identification of WGPu shown in the right most column [77]. 81

Table 5-7. Precision, recall, and F-scores computed for SCINTILLA pedestrian RPM datasets with 1.2 m/s source transit speed, and medical isotope datasets consisting of 1,000 good pulses. The following three isotope identification algorithms are compared: identification using least squares comparison with modified PHDs from Section 5.2 (Method 1), identification using least squares comparison with cumulative distribution functions from Section 5.3 (Method 2), and identification using power spectral density and spectral angular mapper from Section 5.5. 83

Table 5-8. Precision, recall, and F-scores computed for two datasets. Dataset 1 contains SCINTILLA pedestrian RPM datasets with 1.2 m/s source transit speed, and medical isotope datasets consisting of 1,000 good pulses. The more challenging dataset 2 contains the 2.2 m/s source transit speed SCINTILLA datasets and medical radionuclide datasets containing only 400 net accepted pulses. F-scores are computed for both datasets using the identification algorithm using power spectral density and spectral angular mapper from Section 5.5. 83

Table 5-9. Isotope fraction coefficients computed for an LSU algorithm for un-mixing pedestrian RPM data consisting solely of WGPu or ^{137}Cs measurements. The averages and standard deviations of coefficients computed for each possible isotope use 30 three second measurement data sets as inputs. Inputs are either PHDs, CDFs, or power spectral densities.....85

Table 5-10. Isotope fraction coefficients computed for an LSU algorithm for un-mixing pedestrian RPM data consisting of ^{99m}Tc and ^{67}Ga or ^{137}Cs and WGPu mixed in a 1:1 ratio. The averages and standard deviations of coefficients computed for each possible isotope use 30 three second measurement data sets as inputs. Inputs are either PHDs, CDFs, or power spectral densities of CDFs.. 86

Table 5-11. Isotope fraction coefficients computed for an LSU algorithm for un-mixing pedestrian RPM data consisting of ^{137}Cs and WGPu in a 2:1 or 1:2 ratio. The averages and standard deviations of coefficients computed for each possible isotope use 30 three second measurement data sets as inputs. Inputs are either PHDs, CDFs, or power spectral densities of CDFs.. 88

Table 5-12. Isotope fraction coefficients computed for an LSU algorithm for un-mixing pedestrian RPM data consisting of ^{137}Cs, WGPu, and ^{99m}Tc mixed in a 1:3:1. The averages and standard deviations of coefficients computed for each possible isotope use 30 three second measurement data sets as inputs. Inputs are either PHDs, CDFs, or power spectral densities of CDFs.. 89

Table B-1. Overview of test results for pedestrian RPM at 2nd SCINTILLA benchmark at JRC Ispra, Italy, in February 2014. Test results include false alarm test (top left), neutron alarm tests (folders 1-16), as well as gamma-ray photon alarm and ID tests (folders 17-50). The ID results in this table still use a method with weighting masks on the PHDs, thus the discrepancy to values shown elsewhere in Table 5-1 and Table 5-2. 96-97

Table B-2. Radionuclide identification results using SAM on power spectral densities of measured CDFs of thirty datasets of ~1000 good pulses of 99mTc measured with the 7.6 cm diameter cylindrical volume EJ309 organic liquid scintillation detector. These measured spectra are compared the reference spectra for each of the thirteen radionuclides measured with the pedestrian RPM. The lowest SAM value corresponds to the best identification match. For this scenario, all thirty measurements of 99mTc were identified correctly. 98

Table B-3. Table B-3. Radionuclide identification results using SAM on power spectral densities of measured CDFs of thirty datasets of ~400 good pulses of 99mTc measured with the

7.6 cm diameter cylindrical volume EJ309 organic liquid scintillation detector. These measured spectra are compared the reference spectra for each of the thirteen radionuclides measured with the pedestrian RPM. The lowest SAM value corresponds to the best identification match. For this scenario, only 28 of thirty measurements of 99mTc were identified correctly, and the SAM values for 99mTc are twice as high on average compared to those from Table B-2. 99

List of Appendices

Appendix A. RPM XML File Output Example 95

Appendix B. Pedestrian RPM Results for 2nd SCINTILLA Benchmark 96

List of Abbreviations

α	alpha particle, or ^{4}He nucleus
γ	gamma ray photon
ANSI	American National Standards Institute
CBP	United States Custom and Border Protection
CDF	Cumulative distribution function
DAQ	Data acquisition system
DFT	Discrete Fourier Transform
DHS	Department of Homeland Security
DNNG	Detection for Nuclear Nonproliferation Group
FFT	Fast Fourier Transform
FOM	figure of merit, used for optimizing PSD
FWHM	full-width at half maximum
HDPE	high density polyethylene
HEU	highly-enriched uranium
HPGe	high purity germanium (detector)
HV	high voltage
IAEA	International Atomic Energy Agency
IND	Improvised Nuclear Device
INL	Idaho National Laboratory

IO	Inrad Optics, Inc.
ITDB	Incident and Trafficking Database
JRC	Joint Research Centre
keVee	kilo-electron volt electron equivalent, amount of light from 1 keV of electron energy deposited into an organic scintillator
LLNL	Lawrence Livermore National Laboratories
LSU	Linear Spectral Un-Mixing
MDA	Minimum Detectable Activity
MeVee	mega-electron volt electron equivalent
MOX	mixed uranium-plutonium oxide
NNSA	National Nuclear Security Administration
NORM	Naturally Occurring Radioactive Material
NPT	Treaty on the Non-Proliferation of Nuclear Weapons
n	neutron particle
PHD	pulse height distribution
PMT	photomultiplier tube
PSD	pulse-shape discrimination
PVT	Poly-Vinyl Toluene
RDD	Radiological Dispersal Device
RMD	Radiation Monitoring Devices, Inc.
ROC	Receiver Operating Characteristics (curve)

RPM	Radiation Portal Monitor
SAM	Spectral Angle Mapping
SF	spontaneous fission
SNM	Special Nuclear Material, defined as plutonium and enriched uranium

Abstract

Thousands of radiation portal monitors have been deployed worldwide to detect and deter the smuggling of nuclear and radiological materials that could be used in nefarious acts. Radiation portal monitors are often installed at bottlenecks where large amounts of people or goods must traverse. Examples of use include scanning cargo containers at shipping ports, vehicles at border crossings, and people at high profile functions and events.

Traditional radiation portal monitors contain separate detectors for passively measuring neutron and gamma ray count rates. ^{3}He tubes embedded in polyethylene and slabs of plastic scintillators are the most common detector materials used in radiation portal monitors. The radiation portal monitor alarm mechanism relies on measuring radiation count rates above user defined alarm thresholds. These alarm thresholds are set above natural background count rates. Minimizing false alarms caused by natural background and maximizing sensitivity to weakly emitting threat sources must be balanced when setting these alarm thresholds.

Current radiation portal monitor designs suffer from frequent nuisance radiation alarms. These radiation nuisance alarms are most frequently caused by shipments of large quantities of naturally occurring radioactive material containing cargo, like kitty litter, as well as by humans who have recently undergone a nuclear medicine procedure, particularly ^{99m}Tc treatments. Current radiation portal monitors typically lack spectroscopic capabilities, so nuisance alarms must be screened out in time-intensive secondary inspections with handheld radiation detectors.

Radiation portal monitors using organic liquid scintillation detectors were designed, built, and tested. A number of algorithms were developed to perform on-the-fly radionuclide identification of single and combination radiation sources moving past the portal monitor at speeds up to 2.2 m/s. The portal monitor designs were tested extensively with a variety of shielded and unshielded radiation sources, including special nuclear material, at the European Commission Joint Research Centre in Ispra, Italy. Common medical isotopes were measured at the C.S. Mott Children's Hospital and added to the radionuclide identification algorithms.

Chapter 1
Introduction

The threat of nuclear and radiological terrorism has long been simmering in the minds of security experts. United States President Barack Hussein Obama's 2009 Prague speech and resulting four nuclear security summits have heightened the public's awareness of this danger [1]. Far from just being a dramatic television plot device, nuclear smuggling and nuclear terrorism are a genuine threat to global security illustrated by many reports of stolen nuclear and radiological material, interdictions of such materials, and threats by extremist groups to utilize such material [2–4].

Materials of concern range widely in their availability, their applications and their threat to society. Uranium enriched to more than 20% in the isotope ^{235}U and all isotopes of plutonium garner the most attention. These isotopes are classified as special nuclear material (SNM) for they are the key ingredients that make nuclear weapons such powerful instruments of destruction. These materials cannot be found in weapons-usable form in nature, and instead require complex and costly industrial processes for their production, such as uranium enrichment facilities and specialized plutonium production reactors. SNM was produced in large quantities in the nuclear weapons states. While the vast majority of this material was earmarked for weapons programs, tens of tons of highly enriched uranium (HEU) and plutonium were distributed by the United State of America and the Soviet Union to other countries under the auspices of the Atoms for Peace program in the 1950s and beyond for scientific research purposes and as fuel for research reactors [5]. Some peaceful nuclear fuel cycle facilities and processes can also be used to produce or divert SNM. Therefore every signatory of the Treaty on the Non-Proliferation of Nuclear Weapons (NPT) must agree to allow the International Atomic Energy Agency (IAEA) to monitor all nuclear fuel cycle facilities through the application of safeguards.

While the United States Department of Energy's National Nuclear Security Administration (NNSA) continues its efforts to repatriate SNM to the United States and Russia, and the IAEA continues its safeguards mission, no absolute guarantee can be made that SNM

will never be stolen or lost. The notion of terrorists acquiring SNM for an improvised nuclear device (IND) or indeed an intact nuclear device must be taken seriously. The collapse of the Soviet Union in the early 1990s led to a prolonged period of instability in its successor states. Accountability for SNM stockpiles was no longer fully guaranteed. Some SNM left regulatory control through lack of security, corruption, and theft and has since appeared for sale on the black market. The IAEA registered a marked spike in reported interdictions of nuclear and radiological sources in the decade following the collapse of the Soviet Union as seen in their Incident and Trafficking Database (ITDB). The ITDB lists 442 reported radioactive material interdictions worldwide between 1993 and 2014, though only 21 of these involved SNM [6]. The number of successful nuclear smuggling incidents are unknown, though several extremist groups, such as the Japanese doomsday cult Aum Shinrikyo [7] and the Islamist terrorist group Al Qaeda [8], have attempted to acquire SNM and nuclear weapons in the past.

While a successful nuclear terrorist attack remains a serious and devastating possibility, the vast majority of radioactive material interdictions involve radiological sources. Radiological sources, sometimes with dangerously high activity, are commonly used in a variety of industries. Industrial and medical radiological sources are not to be confused with SNM and cannot be used to produce INDs. ^{192}Ir and ^{60}Co are commonly used in radiation therapy and in industrial radiography to inspect welds, and large ^{60}Co sources are also commonly used for sterilizing instruments at hospitals and sterilizing food. A variety of radiological sources are used for treatments and diagnostics in medicine, backscatter gauges, smoke detectors, radioisotope thermoelectric generators and oil well gauging. When used by a trained technician, these radiological sources are a valuable tool in many industries. However, in the wrong hands these materials could be integrated into a radiological dispersal device (RDD), often referred to as a "dirty bomb".

While the destructive capability of an RDD pales in comparison to a nuclear device, its economic and psychological repercussions at the target site should not be underestimated. Industrial radiological sources may lack the stringent security protocols implemented for protecting SNM stockpiles. Historically, many radiological sources also were never disposed of properly. Such orphan radiological sources are a common nuisance at scrap metal yards particularly, and have led to a number of high profile and in some cases deadly accidental

exposures of radiation to unwitting members of the public [9]. Potential thefts pose a threat as well. In Mexico alone there have been at least three high profile incidents of vehicle thefts that led to national security alerts over the past three years because these vehicles were transporting radiological sources [10–12]. While in all cases the radiological material was eventually recovered and the thieves confessed to being solely after the vehicles and ignorant of the radiological cargo, these incidents nevertheless demonstrate the relative ease with which extremist groups could obtain such materials. In Iraq, the so called Islamic State has on multiple occasions stolen radiological sources, including from a university in 2014 [13] and from an oil field in 2016 [14]. The group has subsequently threatened to use stolen radiological materials in RDDs against nations in Europe who participated in air strikes against the Islamic State [15].

The first line of defense must be to improve the security protocols in place for the protection of SNM and radiological sources and to find replacement technologies when feasible. However, these actions do not address the material already available in the black market and in the hands of extremist organizations. To detect and deter the smuggling of SNM and radiological sources, the United States has been pursuing a variety of policies that share one key commonality: the deployment of radiation portal monitors (RPM). RPMs contain detectors that will alarm on the detection of neutrons and gamma-ray photons emitted from SNM and radiological sources. These systems are commonly deployed anywhere a large volume of people and goods traverse some bottleneck, like a border crossing.

A variety of governmental agencies and programs are involved in RPM deployment. The NNSA's Second Line of Defense (renamed Nuclear Smuggling Detection and Deterrence) program has provided RPMs and specialized training in over 50 countries [16]. This program first started in Russia to address unaccounted-for nuclear and radiological material after the Soviet Union breakup. RPMs were installed at border crossings, airports and cargo container ports in order to prevent SNM being smuggled out of Russia. The 2006 SAFE Port Act by the United States Congress also required 100% of the millions of cargo containers entering the United States annually to be screened for SNM and radiological material[17]. The NNSA launched the Megaports Initiative which has installed RPMs at dozens of the world's busiest cargo container ports so that cargo containers are screened well before they even approach the American mainland [18]. Domestically the United States Custom and Border Protection (CBP)

within the Department of Homeland Security (DHS) operates over 1,300 RPMs that screen all vehicular traffic entering from Canada and Mexico, all international mail entering the United States, cargo and luggage entering the United States on international flights and cargo entering the United States at major seaports [19,20].

1.1. Problem Description

On a fundamental level, the threat of nuclear terrorism and nuclear smuggling has been addressed by the United States government through the development and deployment of RPMs both domestically and abroad. That is not to say, however, that there is no room for improvement. As will be shown, much time and money is wasted on processing non-threat RPM alarms. As will be addressed in more detail in subsequent chapters, RPMs operate on relatively simple principles. Neutrons and gamma-ray photons that interact in the RPM radiation detectors are counted. We live in a radioactive world, which means that radiation detectors will always see some contribution from background radiation. This background radiation varies across the world and through time because it depends on myriad factors such as local geology, weather, altitude, cosmic particle fluxes incident on earth, and many more factors.

In general, the neutron background can be considered to be relatively small. Very few naturally occurring radioactive materials (NORM) emit copious amounts of neutrons. Instead, the small observable neutron background arises from interactions of high energy cosmic particles, such as protons and alpha particles, that produce showers of spallation neutrons when interacting with molecules in the Earth's atmosphere. The neutron background varies spatially with altitude and the amount of atmosphere shielding cosmic ray-induced neutrons, and it varies temporally with changes in solar activity and other space weather phenomena [21].

The gamma-ray photon background, however, is orders of magnitude higher than the natural neutron background and can vary tremendously in space and time. The Earth's crust contains a wide array of NORM, particularly from the Uranium and Thorium decay series. Concentrations of these ores vary geographically, and thus too does the gamma-ray photon background. Even at a given location, however, the gamma-ray photon background will vary with events such as rain which will temporarily increase an RPM's exposure to the radiation from radon daughters [22].

RPMs are frequently calibrated with the most recent background count rates. Alarm levels are typically set five standard deviations above expected background count rates. If the neutron and/or gamma-ray photon count rate exceeds these levels during an inspection, the appropriate alarm is issued. However, not every alarm is created equal. An alarm that is triggered by the presence of SNM, an IND, or an RDD is classified as a "threat alarm." These are the only RPM alarms that matter to the CBP and a positive threat alarm will trigger a chain of events in the national security apparatus. As illustrated by the IAEA ITDB, threat alarms are exceedingly rare worldwide. However, in the United States, hundreds of thousands of RPM alarms occur annually that result in tens of thousands of hours of CBP personnel work, consuming tens of millions of tax dollars processing non-threat alarms [19].

What causes these non-threat alarms? A few of these alarms are "false alarms". These alarms arise when natural background radiation exceeds an alarm level setting on the RPM. Such alarms can occur due to improper RPM calibrations but also due to statistical flukes such as a rare large cosmic ray-induced neutron burst or a rapid change in gamma-ray photon background following a heavy deluge. False alarms can be minimized through frequent RPM calibrations for natural background. Also, a tradeoff exists between optimizing the minimum detectable activity (MDA) and minimizing the false alarm rate depending upon how high above natural background the alarm levels are set [23–26].

The most common alarms, however, are "nuisance alarms" [27,28]. SNM and RDDs are by far not unique in their propensity to emit copious amounts of gamma-ray photons. In fact, many commonly-used and transported goods contain enough NORM to set off an RPM gamma-ray photon alarm. The various radioactive isotopes in the Uranium and Thorium decay series are common throughout the Earth's crust, so that many earth extracted raw materials and their finished products are naturally radioactive. These include common construction materials, such as granites, cement and bricks, phosphate derived materials, like fertilizer, and many other products, including cat litter that was estimated to account for a third of RPM nuisance alarms in 2003 [28]. NORM triggered nuisance alarms are common in cargo containers and semi-trailers transporting large amounts of NORM-bearing cargo [29].

Amongst personal vehicles, the largest and growing source of RPM nuisance alarms stems from nuclear medicine and nuclear diagnostics patients. A wide variety of gamma-ray

photon-emitting radionuclides are used in over ten million nuclear medicine procedures annually in the United States. While the most commonly used radionuclides in medicine nearly all have half-lives on the order of hours or days, the doses administered to patients in some procedures are large enough that patients who have very recently been injected with medical isotopes will trigger RPM nuisance alarms when travelling across international borders. The time in days it takes for a medical isotope to decay away sufficiently in a patient to no longer trigger an RPM alarm varies from a few days (^{99m}Tc) to several months (^{131}I) [28,30]. In 2005, it was estimated that greater than 1 in 2,600 Americans carried detectable levels of medical radionuclides [28,30]. While a wide variety of procedures exist, about 98% of nuclear medicine patients undergo diagnostic procedures while only about 2% of cases involved therapeutic procedures that typically involve higher activity sources. While over 17 medical radionuclides are commercially available in the United States for a variety of diagnostic and therapeutic procedures, ^{99m}Tc is by far the most likely isotope to trigger an RPM alarm, as it is used in over 90% of nuclear medicine procedures [28,30].

The issue with nuisance alarms is that currently-deployed RPM technology is unable to rapidly sort these alarms out. Current RPMs only provide gamma-ray photon and neutron count rates. Given an alarm, a second inspection will take place at a secondary RPM screening station to rule out a false alarm or a technical glitch. If both RPM stations result in alarms, CBP personnel must perform a lengthy inspection with handheld and spectroscopy-capable radiation detectors in order to locate and identify all sources of radiation that may have triggered the RPM alarms. As already mentioned, performing these inspections for hundreds of thousands of nuisance alarms annually is not a valuable use of CBP's personnel and budget.

In order to maintain a reasonable pace for the flow of traffic and goods, RPMs must perform their radiation measurement and produce a reliable result in the extremely short time span of a few seconds. This constriction requires the RPM to cover a large solid angle so that sufficient data can be collected in a very short amount of time. For gamma-ray photon detection, almost all deployed RPMs use slabs of poly-vinyl toluene (PVT), an organic scintillator. PVT has the advantage of being capable of being manufactured in large shapes. Other classes of gamma-ray photon detectors, such as inorganic scintillators and semi-conductor materials, are used in the hand-held detectors that CBP uses to screen out nuisance alarms. The material

characteristics of these detectors are such that they are capable of directly measuring the individual gamma-ray photon emission energies that are unique to each radionuclide. This capability allows for the application of gamma spectroscopy, in which detected gamma-ray photon energy peaks are compared to a library of gamma-ray photon spectra in order to identify all present radionuclides. However, these detectors often are impossible or prohibitively expensive to manufacture in the size or number needed for RPMs to be able to provide on-the-fly spectroscopic identification of radionuclides. The spectroscopic RPM has long been desired, but currently commercially available spectroscopic RPMs are sparsely deployed [31–33] and mired in controversy [34]. Much money was spent on developing spectroscopic RPMs that, in the end, performed no better than existing non-spectroscopic RPMs [34].

Organic scintillators typically are incapable of measuring gamma-ray photon full energy depositions which results in the absence of the full energy photo-peaks necessary for gamma-ray photon spectroscopy. Organic scintillators nevertheless are energy-sensitive. For instance, Pacific Northwest National Laboratory (PNNL) has upgraded many of the CBP's RPMs with an energy windowing algorithm that can screen out many NORM sources that have high gamma-ray photon energy emissions above 1 MeV as opposed to the SNM emissions that all occur below 1 MeV [35]. This does not address all NORM sources or many medical radionuclides but this upgrade has already reduced annual RPM nuisance alarms in some cases by over 50% resulting in 230,000 fewer RPM alarms per year and 57,000 hours of savings in CBP personnel time [19]. A cost-effective spectroscopic RPM would result in another round of similar savings for the CBP by completely eliminating gamma-ray photon nuisance alarms.

The cost and time saving benefits of reducing the number of gamma-ray photon nuisance alarms is the first priority in times of heightened security and tight budgets. A long term challenge for current RPM technology surrounds the use of ^{3}He as the neutron detection medium. This gas is obtained from the 12.3 year half-life decay of tritium stockpiles produced in the United States and the Soviet Union for the nuclear weapons complex during the Cold War. Large-scale production of tritium ceased several decades ago. New tritium production is considered to be too cost-prohibitive as a source of new ^{3}He production. In the United States, ^{3}He is distributed to government and commercial users in annual federal auctions. Apart from RPMs, ^{3}He is widely used as a neutron detection medium in nuclear safeguards equipment,

nuclear physics experimental setups, and in the oil and gas exploration industry. After remaining flat at around $50 per liter the price of ^{3}He skyrocketed to $765 per liter for federal users and $2500 per liter for commercial users in 2012. While old ^{3}He can be recycled and auction prices have stabilized, the 12.3 year half-life of tritium means that new supplies ^{3}He will continue to shrink in the coming decades. Therefore there has been much interest in developing alternatives to ^{3}He that would benefit not only RPMs but many other fields dependent upon a reliable neutron detector [36,37].

1.2. Contributions from this Work

This work presents the feasibility of using a variety of organic scintillation detectors in a RPM. One detector material functions as both the neutron and gamma-ray photon detector, thus eliminating the use of ^{3}He prevalent in currently deployed RPM technology. Using a template fitting approach on cumulative distribution functions (CDF) of the measured gamma-ray photon distributions, these new RPM designs are capable of performing on-the-fly distinction of a variety of SNM, industrial and medical radionuclides despite the short measurement time of less than three seconds. These new developments have the potential of significantly reducing the number of RPM radiation nuisance alarms that need to be processed by CBP personnel. The cost and time savings for CBP would be significant, and would allow CBP to devote more of their limited resources and attention towards their many other border protection duties beyond preventing smuggling of nuclear and radiological material.

This work includes a large array of Monte Carlo radiation transport simulations and laboratory scale experiments. This initial research supported the construction of a pedestrian and a vehicle RPM prototype, both of which were tested extensively at a purpose-built facility for RPM testing at the European Commission Joint Research Centre (JRC) in Ispra, Italy. Both prototypes were able to successfully detect a range of SNM and industrial sources under a wide range of test conditions while also maintaining the American National Standards Institute (ANSI)-recommended false alarm rate of less than 1 in 10,000 [38–41]. On-the-fly radionuclide identification proved to be successful for a wide energy range of gamma-ray photon emitting radionuclides. The identification algorithm was successfully extended to include over half a

dozen of the most common medical radionuclides thanks to measurements performed at the oncology unit of the University of Michigan's C. S. Mott Children's Hospital.

Chapter 2
Gamma-Ray Photon and Neutron Detection for RPMs

The gamma-ray photon and neutron signatures measured by RPMs are typically acquired with slabs of the organic scintillator PVT and ^{3}He gas-filled proportional tubes embedded in high density polyethylene (HDPE). Both of these detectors typically only provide gross count rates which are compared to background radiation count rates. For this work, organic liquid scintillation detectors are used for both neutron and gamma-ray photon detection. The properties and operation of these different detector types are introduced and compared.

2.1. Inorganic Scintillation Detectors

In the field of gamma-ray spectroscopy, inorganic scintillators with high detector material density and high atomic number are favored as these parameters affect the degree of attenuation of gamma-ray photons, i.e. intrinsic detection efficiency, and the probability of the gamma-ray photons undergoing photoelectric absorption, respectively, as show in equations (2-1) and (2-2) below:

$$1 - \frac{I}{I_0} = 1 - e^{-\left(\frac{\mu}{\rho}\right)\rho t}, \tag{2-1}$$

$$\tau \cong constant * \frac{Z^n}{E_\gamma^{3.5}}, \tag{2-2}$$

where I and I_0 are the number of transmitted gamma-ray photons with and without the presence of an absorber of density ρ, thickness t, and linear attenuation coefficient μ. For (2-2), τ is the probability of a gamma-ray photon undergoing photoelectric absorption as a function of the detector atomic number Z to an exponent n that can vary between 4 and 5, and the incident gamma-ray photon energy E_γ[42]. In a photoelectric absorption, the entire incident gamma-ray photon is absorbed by the absorber atom resulting in the subsequent emission of a photoelectron from the k-shell with energy equaling the incident gamma-ray photon less the typically negligible binding energy of the photoelectron. These photoelectrons then cause excitations while traversing the inorganic scintillator and the subsequent de-excitations emit scintillation light photons. These scintillation photons are the information carrier and proportional to the

energy deposited by the gamma-ray photons in the detector. The brightness of an inorganic scintillator is defined as the number of scintillation photons emitted per unit of energy deposited in the crystal. The crystal may be painted or wrapped in a diffuse or reflective tape so that the scintillation photons are collected at the unpainted or unwrapped surface to which the photocathode is coupled. At the photocathode, typically a Bialkali material, the scintillation photons now undergo the photoelectric absorptions. The probability of this interaction varies with the scintillation photon wavelength, so photocathode materials must be chosen carefully to match the specific inorganic scintillator scintillation photon emission wavelength spectrum as to maximize the quantum efficiency, defined as the ratio of the number of photoelectrons emitted by the photocathode to the number of incident scintillation photons. The photoelectron signal then finally is amplified through a series of dynodes at high voltage called a photomultiplier tube (PMT) [42]. Alternatively, a solid state light sensor known as a silicon photomultiplier (SiPM) has shown promise as a light readout for scintillation photons. SiPMs are much more compact than PMTs and require a much lower applied voltage to operate [43].

Therefore gamma-ray photons undergoing photoelectric absorption in an inorganic scintillator may result in signal pulses with amplitude directly proportional to the original incident gamma-ray photon energy. When plotted as a pulse height distribution, these pulses result in photopeaks corresponding to the incident gamma-ray photon energies which are unique to each radionuclide. These radioisotope-specific photopeaks allow a spectroscopist to identify the radionuclides present in a pulse height spectrum. Photopeaks exhibit a Gaussian shape, and the sharpness of photopeaks and the ability to separate adjacent peaks in energy determine the resolution of the detector which is often expressed as the ratio of the photopeak full width at half maximum and the photopeak energy [42].

However, not all gamma-ray photons will undergo photoelectric absorption. Compton scattering is defined as an interaction in which an incident gamma-ray photon imparts only some of its energy to a recoil electron and is deflected at a scatter angle with diminished energy. This is often the most common interaction for gamma-ray photons. The recoil electron is imparted energy (E_{e^-}) equal to the difference between the incident and scattered photon and it otherwise behaves identically to the previously described photoelectron. The scattered photon energy, and thus also the recoil electron energy, depends upon the scatter angle θ as shown in (2-3):

$$E_{e^-} = hv - hv' = hv - \frac{hv}{1+\frac{hv}{m_o c^2}(1-\cos(\theta))}, \tag{2-3}$$

where hv' and hv are the scattered and incident gamma-ray photon energies, and $m_0 c^2$ is the electron rest mass energy. As the scatter angle can vary from zero to π this leads to the Compton continuum. The Compton continuum is bounded on the lower end by grazing scatters in which almost no energy is imparted upon the recoil electron. The Compton continuum does not, however, stretch all the way to the photopeak as the maximum energy the recoil electron can receive occurs in a head-on collision at $\theta = \pi$ as shown in (2-4). This maximum is known as the Compton edge:

$$E_{e^-}|_{\cdot\theta=\pi} = hv\left(\frac{\frac{2hv}{m_o c^2}}{1+\frac{2hv}{m_0 c^2}}\right). \tag{2-4}$$

2.2. Organic Scintillation Detectors

Almost all RPMs, however, do not use inorganic scintillation detectors for gamma-ray photon detection. Instead they use PVT, an organic scintillation detector consisting mostly of hydrogen and carbon. Three major categories of organic scintillators include organic crystals (stilbene, anthracene), organic plastics (PVT), and organic liquids (EJ309). Though vastly different in physical appearance they all depend upon the same radiation detection mechanisms. The effective atomic number of organic scintillation detectors is very low. Therefore the probability of photoelectric absorption of gamma-ray photons is exceedingly rare for incident gamma-ray photon energies over 100 keV. Nearly all gamma-ray photon interactions involve Compton scattering. Thus organic scintillation detectors are typically ill-suited for gamma-ray photon spectroscopy as they produce spectra with no photopeaks. However, some attempts have been made at loading scintillators with high atomic number additives, like bismuth, [44,45], or using deconvolution algorithms [32] to achieve some ability to perform gamma ray spectroscopy with organic scintillation detectors.

Organic scintillation detectors are not only sensitive to gamma-ray photons, but are also efficient detectors for fast neutrons. As organic scintillators consist predominantly of low-atomic number materials, like hydrogen and carbon, the most probable interaction for fast neutrons is elastic scattering in which some of the incident neutron kinetic energy is transferred to the recoil

nucleus. The resulting recoil nucleus of energy E_R will cause excitations in the scintillator which will lead to the emission of scintillation photons, similar to the process already described for photoelectron and recoil electrons for gamma-ray photon photoelectric absorption and Compton scattering. The resulting recoil nucleus energy for a fast neutron of energy E_n elastic scattering depends upon both its scattering angle θ and the recoil nucleus atomic mass number A as shown in (2-5) below:

$$E_R = \frac{4A}{(1+A)^2}(\cos^2(\theta))E_n, 0 \leq \theta \leq \frac{\pi}{2}. \quad (2\text{-}5)$$

(2-5) shows that for a head on collision ($\theta = 0$) on hydrogen ($A = 1$) the entire incident neutron energy E_n will be imparted to the recoil nucleus E_R, while for a grazing collision ($\theta = \frac{\pi}{2}$) effectively zero energy is transferred to the recoil nucleus. For recoil nuclei heavier than hydrogen, the maximum fractional energy transfer in neutron elastic scattering decreases rapidly with increasing recoil nucleus atomic mass number. For instance, for the other main constituent of organic scintillators, carbon ($A = 12$), the maximum possible energy transfer to the recoil carbon nucleus is only 28.4% of the incident fast neutron energy.

For both gamma-ray photon and neutron interactions, the energy deposited in the detector is directly related to the measured light output measured in units of keVee (keV electron equivalent). While the ratio between deposited energy in keV and light output in keVee is defined as one-to-one for gamma-ray photon interactions, the relationship between deposited energy and light output is non-linear and significantly less than one-to-one for heavier particles like the recoil protons from neutron elastic scattering.

Calibrating organic liquid scintillation detectors for their response to gamma-ray photons involves measuring their response to a series of mono-energetic gamma-ray photon sources. One popular choice is the ^{137}Cs 662 keV gamma-ray photon that according to equation (2-4) should result in a visible Compton edge at 478 keVee light output. Measured ^{137}Cs pulse height distributions (PHDs) are shown in Figure 2-1a from a variety of organic scintillation detectors. These PHDs are simply histograms of the pulse heights for all measured pulses. For the particular digitizer used, pulse heights can vary between zero and two volts. For the gamma-ray photon calibration, one simply needs the location in volts of the Compton edge of known energy.

This value is then used for linear conversion of deposited energy to light output. Picking the exact location of the Compton edge, however, is not trivial, because one must include the effects of the inherent resolution of the detector. Using a Monte Carlo particle transport code, like MCNP6, one can obtain both simulated un-broadened and resolution broadened PHDs for ^{137}Cs, both of which have been normalized and are shown in Figure 2-1b. The true Compton Edge is given by the peak of the un-broadened simulation. The location where this peak intersects with the Compton edge of the simulated resolution broadened PHD tells one what percentage of the Compton edge peak to use for calibration purposes. This value can then be used to convert measured PHDs from the digitizer units of volts to light output with units of keVee, as shown in Figure 2-1b. For many organic liquid scintillation detectors a calibration value of approximately 80% of the ^{137}Cs Compton edge peak leads to good agreement between measurement and simulation taking into account detector resolution. For larger volume detectors, however, like the 25 cm by 25 cm by 10 cm BC501A liquid organic scintillation detector shown in Figure 2-1b, multiple scattering effects result in a much larger percentage of the Compton edge peak (e.g. 96% for the BC501A detector) being necessary for calibrations.

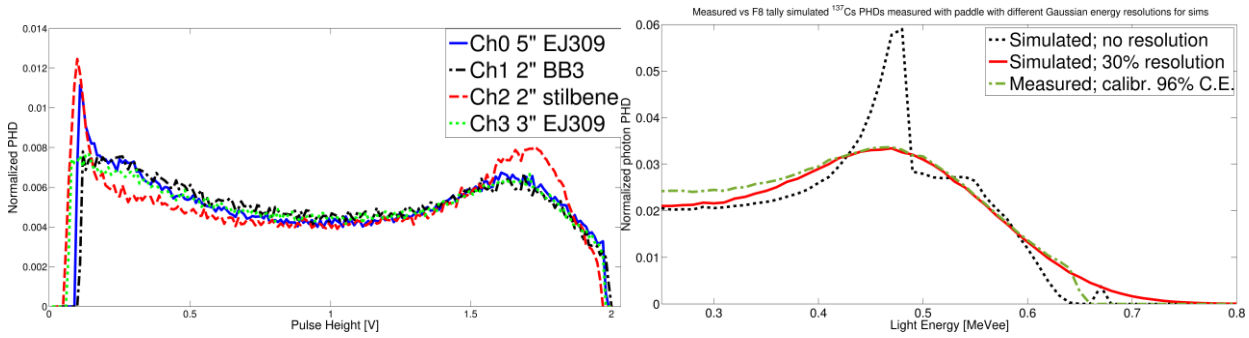

Fig. 2-1. (a) Examples of ^{137}Cs PHDs obtained with a variety of organic liquid scintillation detectors such as liquids (EJ309), plastics (BB3) and crystals (stilbene). Pulse heights are still in digitizer units of volts, and no energy calibration has taken part yet. (b) MCNP6 simulated un-broadened and resolution broadened PHDs for measurements of ^{137}Cs with a 25 cm by 25 cm by 10 cm BC501A liquid organic scintillation detector reveal that a calibration value of 96% of the Compton edge peak should be set to equal the 478 keV Compton edge. This conversion is used to convert the measured ^{137}Cs PHD from volts to light output in keVee.

In traditional PVT organic scintillator RPMs, the contribution of neutron elastic scattering to the PVT signal is accepted as a negligible nuisance relative to the contributions of gamma-ray photon Compton scattering interactions. For background radiation alone, the gamma-ray photon count rate in the PVT will be around three orders of magnitude higher than the neutron background count rate. In currently deployed RPMs, the neutron count rate is acquired

separately with ^{3}He proportional tubes. However, for some organic scintillation detectors one can distinguish the light pulses arising from neutron versus gamma-ray photon interactions through pulse shape discrimination (PSD) with the charge integration method.

2.2.1. Pulse-Shape Discrimination via the Charge Integration Method

As previously described, the recoil electrons and recoil protons resulting from gamma-ray photon Compton scattering and neutron elastic scattering interactions in the organic scintillator will cause excitations in the detectors material. The subsequent de-excitations result in the emission of visible light that is collected at the photocathode. In the 1950s, it was discovered for organic scintillators like stilbene and anthracene that this light has both a prompt and a delayed component, and the heavier the interacting particle (alpha particle versus neutron vs gamma-ray photon), the greater the fraction of the total light emission occurred as part of the delayed component [46,47], as shown in Figures 2-2a and 2-2b.

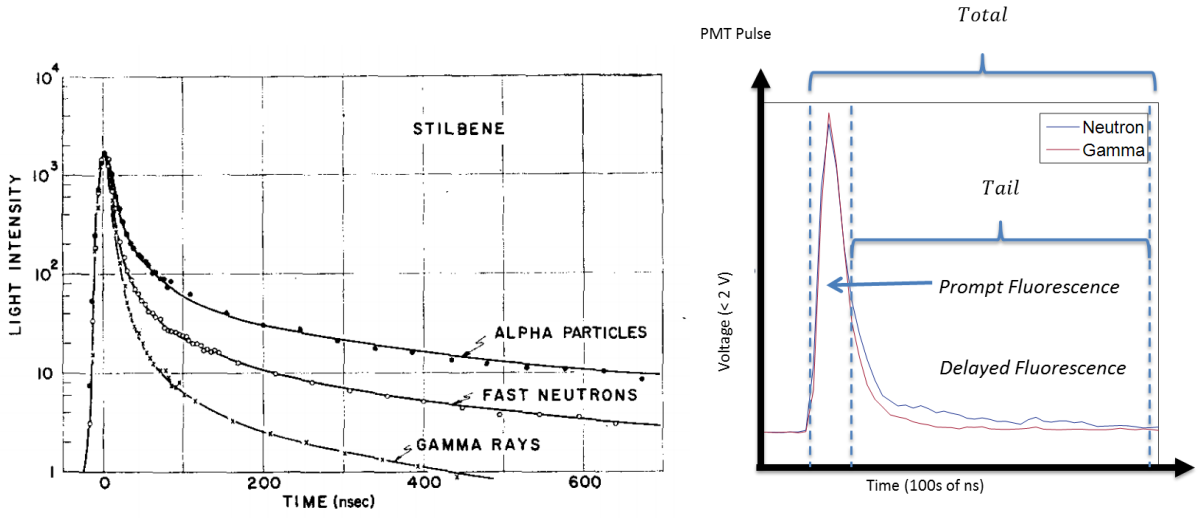

Fig. 2-2. (a) On the left is one of the first measurements showing increasing delayed scintillation light component with increasing mass (stopping power) of incident radiation on organic scintillator (stilbene) [47]; (b) On the right, typical pulses for EJ309 organic liquid scintillation detector showing increased delayed light component for neutron vs gamma-ray photon interaction, thus forming basis for PSD.

The underlying physics of this prompt versus delayed scintillation components were described in the 1960s [48]. For organic molecules with π-electron structure (such as organic scintillators), the energy levels of the molecule include both a number of singlet and triplet excited states (see Figure 2-3). Energy from the recoil electrons and recoil protons is absorbed by exciting the electron configurations of the organic scintillator molecules to the excited states shown in Figure 2-3. Transitions between the S_{10} excited singlet state and any of the $S_{0\#}$ ground

states occurs with an exponential decay with decay time constant of a few nanoseconds. This light emission therefore is relatively fast and contributes to the prompt scintillation light component shown in Figure 2-2b. This process is known as fluorescence. Singlet excited states can also be converted to triplet states. The lifetime of the triplet states, like T_1, however, is much longer ($\sim 10^{-3}\ s$). Therefore de-excitations from triplet states contribute to the delayed scintillation light component and are known as phosphorescence. When two molecules that have been excited to a triplet state meet while migrating, they will annihilate to a molecule in the ground state and a singlet excited state molecule. This triplet-triplet annihilation thus also contributes to the delayed scintillation light component. Therefore a greater concentration of triplet states would lead to a higher probability of triplet-triplet annihilation and thus an increased delayed scintillation light component. The Bethe formula, equation (2-6) for stopping power shows that heavier particles, like recoil protons versus recoil electrons, travel more slowly through the detector material and have a shorter range, thus depositing their energy in a smaller volume and thus creating a greater density of triplet excited states:

$$S = -\frac{dE}{dx} \sim \frac{(ze)^2}{v^2}, \tag{2-6}$$

where v is the velocity of the exciting particle (recoil electron, recoil proton) and ze is its charge. As shown in Figure 2-2a, heavier incident particles lead to a greater delayed light scintillation light fraction in organic scintillators. This is related to the linear energy transfer rate of the exciting particle and its effects on triplet state density. Recoil electrons from gamma-ray photon Compton scattering produce lower triplet state density than heavier and slower recoil protons from fast neutron elastic scattering which produce lower triplet state density than the even heavier and slower alpha particles, thus leading to the differences in delayed scintillation light for these three types of radiation shown in Figure 2-2a.

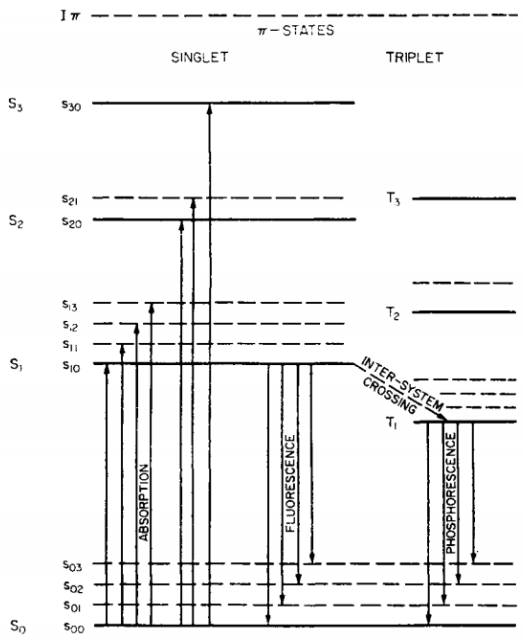

Fig. 2-3. Energy levels for organic molecule with π-electron structure with singlet and triplet excited states. The de-excitation of these states (fluorescence and phosphoresence) cause the prompt and delayed scintillation light components in organic scintillators [48].

When one plots the tail and total integral for organic scintillator pulses, like those shown in Figure 2-2b as a density plot, one can see distinct bands from gamma-ray photon and neutron interactions, where the neutron band clearly exhibits a larger tail integral on average. An example of such a PSD plot is shown in Figure 2-4 for a ^{252}Cf measurement with a liquid organic scintillation detector. A discrimination curve separates these two bands and all interactions above this curve are classified as neutron interactions and all interaction below this curve are classified as gamma-ray photon interactions.

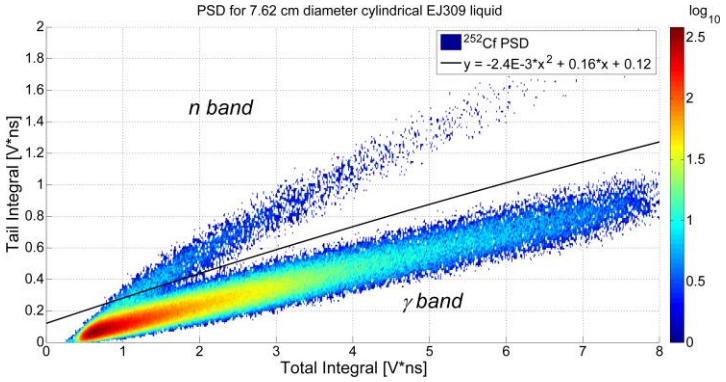

Fig. 2-4. Pulse shape discrimination for measurement of ^{252}Cf with 7.62 cm diameter EJ309 liquid [39][49].

When creating a PSD plot, as shown in Figure 2-4, the user's goal will be to minimize the amount of misclassification, i.e. gamma-ray photon interactions being misclassified as neutron interactions and vice versa. This is best achieved by maximizing the separation between the two PSD bands. While this depends heavily upon detector material characteristics, the user also plays a critical role in the quality of the PSD via the choice of the PSD integral windows and the choice of the PSD discrimination curve. Going back to Figure 2-2b, the user must choose where to start the tail integral and where to set bounds for the total integral. These settings will affect the slopes of the PSD bands as well as the PSD quality. The PSD quality is often expressed with a figure of merit (FOM), as shown in equation (2-7) below:

$$FOM = \frac{Centroid_N - Centroid_G}{FWHM_N + FWHM_G}, \tag{2-7}$$

where the centroids and full-width-half-maxima (FWHM) are taken from the fitted Gaussian distributions of the neutron and gamma-ray photon distributions when plotting the histograms of the tail-to-total integral ratios, as shown for Figure 2-5. The greater the separation between the two Gaussian distributions and the narrower the two distribution are individually, the greater the FOM will be for the PSD. Using linear slices of a PSD plot containing mixed neutron and gamma-ray photon data, such as Figure 2-4, one obtains Gaussian fits, like those in Figure 2-5, for each individual slice. Picking the point of minimum misclassification of photons and neutrons for the two fitted Gaussians for each individual slice provides a dataset to which the PSD discrimination curve can be fitted. The curve, as shown in Figure 2-4, is quadratic and has three coefficients. The user might choose to bias the curve, however, if say a lower misclassification rate of gamma-ray photons as neutrons is more important than a low misclassification rate of neutrons as gamma-ray photons. The process of creating this PSD curve is well suited for automation [50].

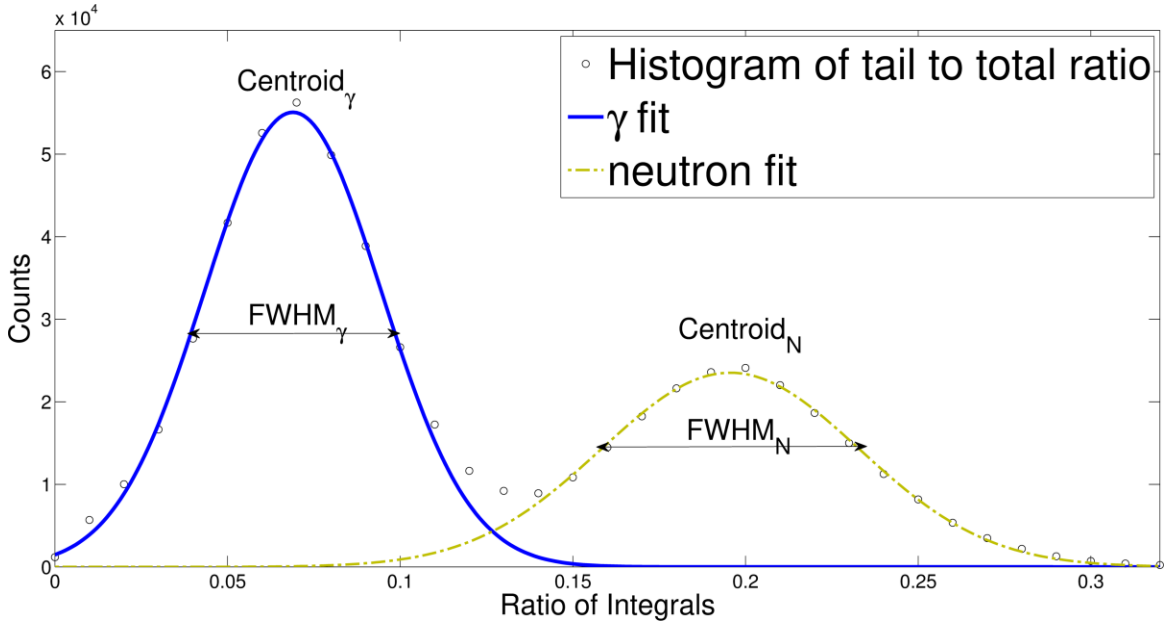

Fig. 2-5. Histogram of tail-to-total integral ratio for ^{252}Cf data acquired with 25 cm by 25 cm by 10 cm BC501A organic liquid scintillation detector. Fitted Gaussian distributions for gamma-ray photons (left, blue) and neutrons (right, yellow) are used for calculating FOM using equation (2-7) [49].

2.2.2. Types of organic scintillation detectors used

Organic scintillation detectors are manufactured from a variety of material forms (liquids, crystals, plastics) and come in many different shapes and sizes. The detectors and their respective PMT light readouts used in the experiments discussed in this dissertation are listed in Table 1-1, and the material properties of these detectors are listed in Table 2-2. An example of the typical composition of an organic scintillator coupled to a PMT is given in Figure 2-6. Figure 2-7 shows a gallery of the detectors listed in Table 1-1.

Table 2-1. Manufacturer and model numbers for organic scintillation detectors used in measurements for this dissertation.

Scintillator Type	Detector			PMT	
	Name	Manufacturer	Model #	Manufacturer	Model #
Liquid	7.62 cm ø EJ309	SCIONIX-Holland	76A76/3M-EJ309 E1XNEG	Electron Tube Enterprises	9821B
	12.7 cm ø EJ309	Eljen	510-50X50-4B/309	Photonis	XP4512B
	25x25x10 cm^3 BC501A	SCIONIX-Holland	R500$80A500/3-LS-X-N	Photonis	P4312
Plastic	5.08 cm ø BB3 − 5 (bibenzyl)	RMD	experimental	Electron Tube Enterprises	9821
Crystal	5.08 cm ø stilbene	Inrad Optics	-	Electron Tube Enterprises	9821

Table 2-2. Properties of various organic scintillators by the listed manufacturer [42,51–55].

Scintillator Type	Model or Manufacturer	Density (g/cm^3)	Light Production (% Anthracene)	Decay Constant (ns)	Softening or Flash Point (°C)	PSD ?
Plastic	Bibenzyl (BB3-5)	1.1	57	10	NA	Yes
Liquid	EJ-301/BC501A	0.874	78	3.2	26	Yes
	EJ-309	0.959	75	3.5	144	Yes
Stilbene	Inrad Optics	1.16	>75	4.5	125	Yes
Anthracene	--	1.25	100	30	217	Yes

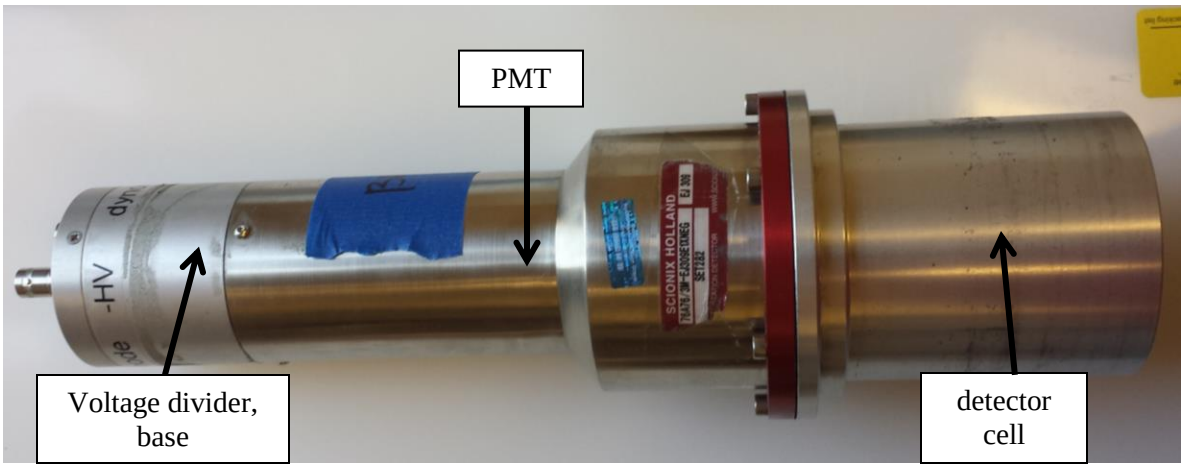

Fig. 2-6. Example of standard composition of an organic scintillation detector coupled to a PMT. Detector cell could be a crystal (stilbene), plastic (BB3, EJ299-33,) or, as in this cases, a liquid cell (EJ309).

Fig. 2-7. Examples of the detectors used in measurements in this dissertation including from left to right: 7.62 $cm \emptyset$ $EJ309$ organic liquid scintillation detector, 12.7 $cm \emptyset$ $EJ309$ organic liquid scintillation detector, 25 cm by 25 cm by 10 cm BC501A organic liquid scintillation detector, 5.08 $cm \emptyset$ stilbene crystal couple to PMT (5.08 $cm \emptyset$ BB3 plastic scintillator looks identical when wrapped and coupled to PMT). Pictures are not to scale relative to each other.

2.2.3 Digital acquisition systems

The block diagram in Figure 2-8 shows a typical measurement setup. The organic scintillation detector PMT is powered by a high voltage power supply. The PMT anode signal is fed to a digitizer in which the amplified detector signal from the collected and converted

scintillation light output is sampled and digitized (i.e. for each pulse only a set of pulse heights sampled at equidistant time intervals are saved). For each pulse this PHD dataset and the time stamp of the pulse are transferred via USB cable or optical link to a computer. Acquisition software is used to set parameters such as the acquisition window for each pulse, the trigger threshold for acquiring/saving pulses, the measurement time, and many other parameters. A post-processing script is then used to perform PSD on all pulses and determine the user desired outputs like neutron and gamma-ray count rates or PHDs.

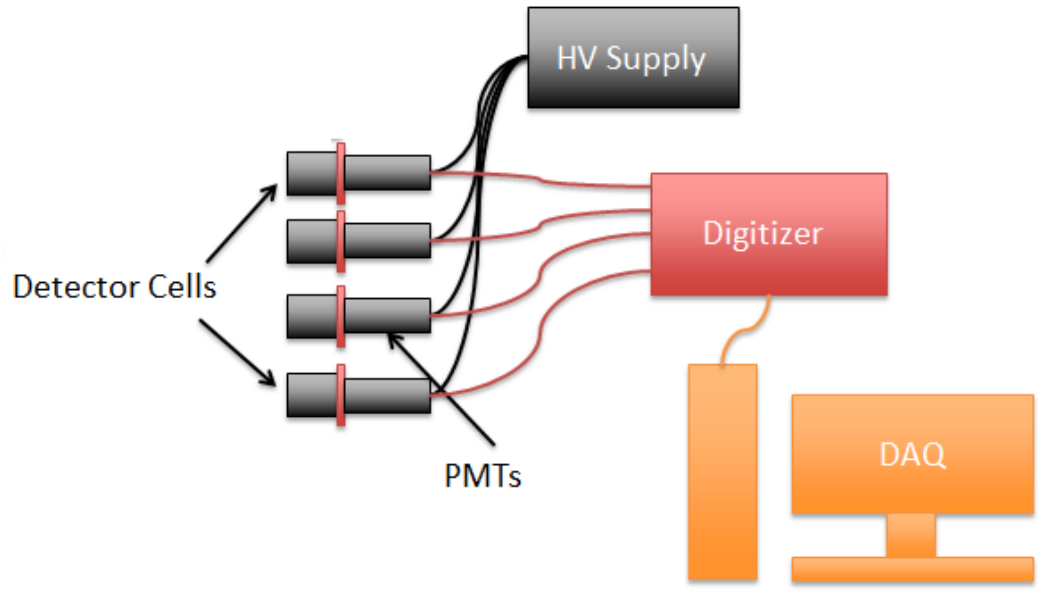

Fig. 2-8. Block diagram of a multi-detector setup, where the PMTs are powered by a high voltage (HV) power supply. Detector anode output signals are fed to a digitizer, and packets of digitized pulses with time stamps are fed via USB link or optical link to a data acquisition system (DAQ). Pulses are processed on the DAQ using PSD to determine parameters such as neutron and gamma-ray photon count rates or PHDs or any other user desired information.

For all experiments mentioned in this dissertation, detector anode pulses were digitized with waveform digitizers from CAEN including the DT5720/V1720 and DT5730/V1730 where the "DT" models are portable desktop digitizers with fewer channels whereas "V" models will have more channels but are used in conjunction with a VME crate. Otherwise the specification of a DT5720 and V1720, for example, are identical [56]. Examples of these digitizers are pictured in Figure 2-9.

Fig. 2-9. CAEN V1730 (top) and DT5720 (bottom) digitizers.

The sampling rates for these digitizers are either 250 MHz (DT5720/V1720) or 500 MHz, which means that every 4 ns or every 2 ns the local pulse height of the pulse in time is sampled. These digitizers have either 12-bit ($2^{12} = 4096$ voltage bins) or 14-bit (2^{14} = 16384 voltage bins) vertical resolution. Given a digitizer 2 V dynamic range, all non-clipped measured pulses will therefore theoretically have pulse heights between 0 V and 2 V. Due to the user set trigger threshold, and a user set offset for the baseline, the actual range of acceptable pulse heights will in reality be a bit more constricted.

A variety of CAEN-provided and University of Michigan Detection for Nuclear Nonproliferation Group (DNNG)-written data acquisition scripts were utilized in all experiments. These tools are used to initiate and execute data acquisition and to set a variety of important measurement parameters such as channels to trigger on, measurement time, trigger thresholds, baseline offsets, acquisition window length for pulses, trigger location within pulse, and several other parameters. Whenever a detector anode signal pulse exceeds the user-set trigger threshold, any signal in the digitizer buffer is converted into waveforms. These waveforms are written to a file and data is transferred from the digitizer to the DAQ via USB cable or optical link. In high count rate measurements the measurement system is limited by the 80 MB/s processing limit of the digitizer, as well as additional limitations such as data transfer rate via USB versus optical link and the hard drive writing speed of the DAQ. Whenever the digitizer buffer is full due to an overwhelmingly high acquisition rate, additional incoming data

will be lost leading to an underestimation of count rate [56]. However, in the vast majority of measurements in this dissertation count rates were well below any of these upper limits.

2.3. ^{3}He neutron proportional counters

^{3}He proportional tubes have long been the neutron detector of choice not only in RPM systems, but also in a wide variety of safeguards and nuclear security equipment. This isotope of helium exhibits an incredibly high interaction cross-section for undergoing the thermal neutron capture reaction in equation (2-8):

$$^{3}He + n_{th} \rightarrow {}^{3}H + {}^{1}H + 764\ keV, \sigma = 5330\ b, \tag{2-8}$$

where the charged particles (proton and triton) share the Q of this reaction (764 keV) which has a cross-section σ for thermal neutron capture. This cross-section drops off rapidly with increasing neutron energy. SNM and other materials typically emit fast neutrons on the order of MeV, while the capture reaction is most efficient for thermal neutrons. Therefore ^{3}He proportional tubes are usually embedded in a hydrogenous moderator, such as HDPE, which thermalizes the incident neutron flux.

Proportional counters have been around since the 1940s. An anode wire runs through the cylindrical tube containing the fill gas (^{3}He). HV is applied to the anode wire to create an electric field. The protons and tritons resulting from the thermal neutron captures will ionize the fill gas thus creating electron-ion pairs. If the applied bias is high enough, recombination of these pairs will be suppressed. The electric field will result in migration of the electrons to the anode wire and ions to the cathode tube wall. The accelerated electrons will liberate secondary electrons in subsequent collisions with neutral gas atoms. If the applied electric field is chosen carefully, these secondary ionizations will lead to an avalanche of subsequent secondary ionizations. This gas multiplication process is known as a Townsend avalanche. Because the electric field rapidly decreases with distance from the anode wire, nearly all multiplication will occur within very close proximity to the anode wire. While the electrons will be quickly collected at the anode wire, the vast majority of the signal pulse is made up of the slow drift of the ions to the far away cathode wall. In a certain applied voltage region, the avalanche signal will be proportional to the energy deposited, thus the name proportional counter. Within a voltage region, known as the plateau, the measured count rate for a given neutron source should be independent of any applied

voltage fluctuations. For each thermal neutron detected, one expects the same amount of energy to be deposited, so the neutron count rate should be proportional to energy deposited in the tube. In reality, the range of the triton and proton are large relative to the tube dimensions. For capture reactions taking place near the tube walls, the proton or triton might escape the tube, thus leading to incomplete energy deposition and a feature known as the wall effect. The efficiency of the detector will vary with fill pressure of the gas, typically between two and ten atmospheres [42,57].

Every pulse in a ^{3}He proportional counter is typically fed into a module containing a charge sensitive pre-amplifier followed by an amplifier, wave shaping and discriminator circuits. This means that the output of the tube is simply a TTL logic pulse for each incident pulse over threshold. The TTL outputs of multiple tubes can be daisy-chained together to give a summed output. Gamma insensitivity is another important attribute for these detectors. With no threshold applied, ^{3}He will register a pulse for approximately 1 in 10,000 incident gamma-ray photons. However, by implementing a small detection threshold, the gamma-ray rejection rate, i.e. the rate at which gamma-ray photons are falsely registered as neutrons, can be lowered to 10^{-8} [23]

Because ^{3}He is the gold standard that we are trying to replace due to the reasons explained in Chapter 1, it is important to benchmark all new RPM developments to ^{3}He performance. Therefore many measurements were also performed with the ^{3}He RPM system shown in Figure 2-10. This system consists of three 3.92 atm GE-Reuter-Stokes model RSP4-1659-202 ^{3}He proportional tubes. These tubes have a 5.08 cm diameter and are 152.4 cm long. The neutron pulse monitoring modules containing the amplifier and discriminator logic circuits are Precision Data Technology models PDT 10A and PDT 20A-HN. The 20A-HN has its own internal HV power supply for the proportional tube anode wire, while the 10A neutron pulse monitoring module does not. For tubes with the 10A model module, external HV bias was supplied with a CAEN model N472 HV power supply. The neutron pulse monitoring modules are powered by +12V provided by an Agilent Technologies model E3641A low power supply. The TTL logic pulse outputs were daisy-chained and counted with a Tennelec model TC536 counter/timer.

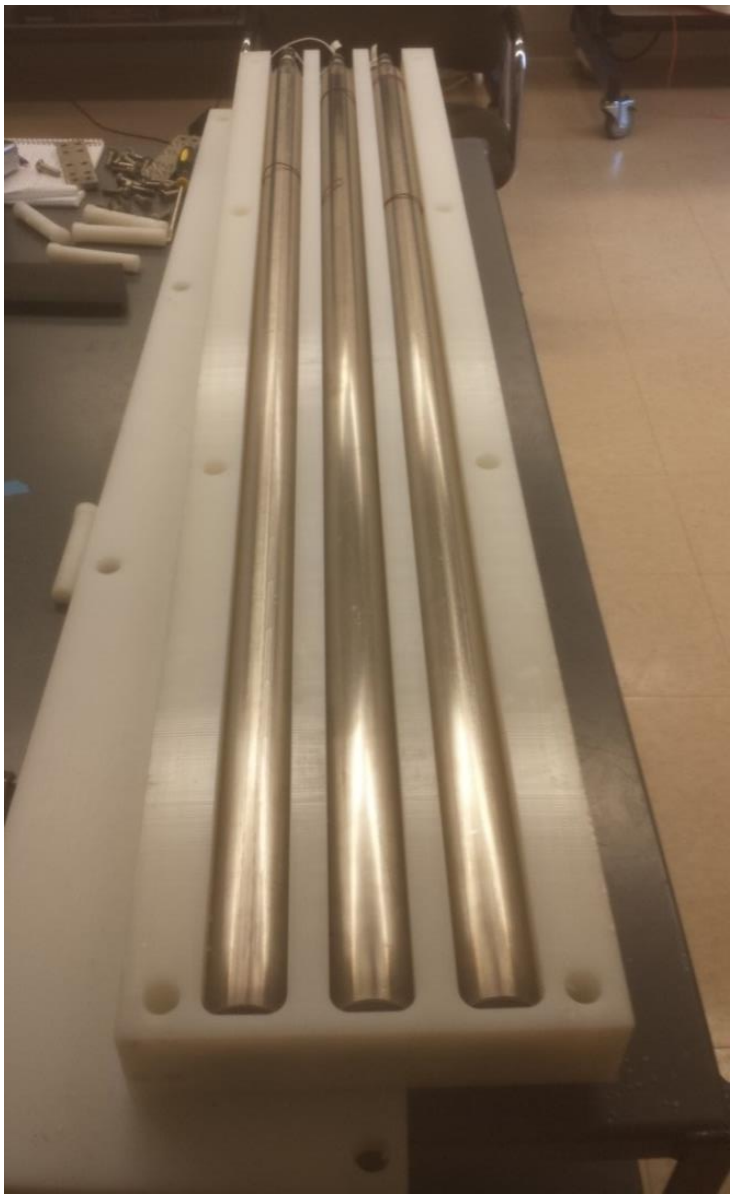

Fig. 2-10. Opened ^{3}He RPM containing three ^{3}He proportional tubes embedded in HDPE.

Chapter 3
Modeling and Designing RPMs with MCNPX-PoliMi and Benchtop Experiments

Several RPM prototypes were tested, and the results of those measurements are presented in Chapter 4. First, however, the RPM prototypes had to be designed and tested. This chapter focuses on three key design steps. First, particle transport codes were used to study a variety of design criteria and parameters in simulation space. This offers an inexpensive pathway to explore a wide variety of design ideas before committing to any particular hardware. Second, scaled down experiments with single detectors were used to confirm simulation findings, and establish basic system performance criteria like false alarm rates and minimum detectable activity through receiver operating characteristics curve analysis. Third, radiation detectors, occupancy sensors, data acquisition, and software had to all be integrated into a complete RPM system.

3.1. Modeling RPMs with MCNPX-PoliMi

3.1.1. The Particle Transport Code MCNPX-PoliMi

Simulation tools are a valuable commodity when developing a radiation detection system, such as an RPM. In particle transport codes, the user defines a radiation detection system, its surrounding environment, and the radiation source. The particle transport code then simulates a user-defined number of radiation source emissions, and tracks how each source particle travels though and interacts with the user defined environment. A random number generator and probabilities from cross-section libraries are used to create a random history for each source particle.

For example, one might simulate a ^{137}Cs gamma-ray photon point source, an organic liquid scintillation detector placed some distance from the radiation source, and environment, such as the walls and floors of the room of this experiment. Each source history begins with the creation of an isotropically-emitted 662 keV gamma-ray photon at the radiation point source location. Random numbers and interaction cross-sections for the materials in the environment would determine how this photon travels through and interacts with the environment. Interactions might lead to changes in energy, direction, and momentum of the photon.

Interactions might lead to the creation of additional particles, which are also tracked. In the end, every particle is either absorbed somewhere in the environment or escapes the user-defined geometry.

The goal of these simulations for RPM design is to simulate the detector response to a variety of radiation sources. Simulations allow the user to quickly experiment with a wide range of radiation sources, detector types and configurations, and experimental environments at a fraction of the time and cost that would be required to perform with actual physical experiments. The RPM will have several required design parameter limitations, such as a minimum detection efficiency, or size/weight/cost constraints. One can thus simulate infinite design configurations to whittle down the selection to a handful of configurations with the most promising simulation results.

The particle transport code MCNPX-PoliMi was used for all simulations [58]. MCNPX-PoliMi samples cross-section libraries, like ENDF-VII, to simulate the movement and interactions of gamma-ray photons and neutrons through a user-created environment as a function of particle energy and momentum. This particular code has several benefits over other particle transport codes, including built-in spontaneous fission and (alpha,n) sources. MCNPX-PoliMi can produce a collision data output file for user-specified cells, such as the radiation detector material cells. The collision data file is useful for simulating detector response as it stores information for all neutron and photon interactions in the chosen cells. Stored information includes a total of 16 parameters, such as the particle type, the interaction type, the target nucleus, the time and location of the interaction, and the energy deposited, among others.

As explained in section 2.2, the scintillation light produced due to radiation interactions in an organic scintillation detector depends upon the incident particle type, the target nucleus, and the energy deposited. All of this information is included in the MCNPX-PoliMi collision output file. The MCNPX-PoliMi Post-Processing script, MPPost, has been developed and maintained by DNNG [59]. MPPost reads in the MCNPX-PoliMi collision data files. Light output is calculated as a function of energy deposited using relationships specified by the user in an input file. The total light output for all energy deposited for one history occurring within the scintillator's pulse generation time is used to recreate an individual pulse. Processing the entire collision output file will result in thousands of pulses. MPPost outputs pulse height distributions

separated by particle type. The simulated number of source particles and the desired hypothetical source activity can be used to determine the simulated measurement time. The simulated measurement time and summed pulse height distributions yield simulated neutron and gamma-ray photon count rates for the simulated RPM for the simulated radiation source scenario.

3.1.2. Modeling Light Output for Organic Scintillators

As already explained in section 2.2., a one-to-one relation exists between energy deposited by gamma-ray photons and light output in organic scintillation detectors when using electron-equivalent light output units. The light output produced as the result of neutron interactions in organic scintillators, however, is non-linear and exhibits significantly less than a one-to-one ratio. The light output for neutron collisions on carbon is very small for several reasons. From equation (2-5), it can be shown that the recoil carbon nucleus can at maximum only receive 28% of the incident neutron energy, whereas hydrogen recoil nuclei can receive up to 100% of the incident neutron energy. Additionally, due to the lower velocity of carbon recoil nuclei as well as their higher stopping power relative to lighter hydrogen recoil nuclei (see equation 2-6), neutron scattering on carbon should result in relatively low light output. Low light output for carbon scattering, often below the user-set energy threshold, has also been shown in measurements [60] . For MPPost light output conversions, it was assumed that carbon recoil nuclei resulted in light output equivalent to two percent of the energy deposited by the incident neutron [60].

Determining the light output response neutron collisions on hydrogen in organic scintillators often requires time-of-flight measurements, such as those described in [61]. Different neutron time-of-flight slices correspond to different incident neutron energies that can be computed from the known neutron flight path and flight time. For every incident neutron energy, the neutron can deposit from zero up to all of its energy in a collision with a hydrogen nucleus. Taking into account energy resolution broadening effects, one can use the upper limits of the pulse height distributions formed by these quasi-monoenergetic neutron interactions on hydrogen to build a dataset of neutron light output response. These data will vary with detector type and shape, and due to statistical and measurement limitations, these response data will often not cover the full neutron energy range of interest. Choosing the fitted and extrapolated neutron light output response curve therefore plays a crucial role in the degree to which simulated and

measured organic scintillator neutron pulse height distributions will agree. Exponential fits, as well as those suggested by Birks and Voltz are commonly used, and are shown in equation (3-1) through (3-3) [62,63]:

$$Exponential: L(E) = aE - b[1 - c * \exp(-E^d)], \tag{3-1}$$

$$Birks: L(E) = \int \frac{a}{1+b\left(\frac{dE}{dx}\right)} dE, \tag{3-2}$$

$$Voltz: L(E) = a \int \left[(1-c)\exp\left[-\frac{b(1-c)dE}{dx}\right] + c\right] dE, \tag{3-3}$$

where $L(E)$ is the light output produced by the organic scintillator for neutrons depositing energy E in the detector through interactions on hydrogen. Coefficients $a, b, c,$ and d are determined through fitting the above functional forms to the measured neutron response data. For detectors discussed in this dissertation, Birks and Voltz were found to produce the best agreement to measured data [49].

3.1.3. Modeling Moving Sources with MCNPX-PoliMi

Radiation sources in MCNPX-PoliMi can be simple mono-energetic point sources, like a ^{137}Cs calibration source, or complex volumetric sources with many different emissions, like a mixed-oxide (MOX) fuel canister. Regardless of the complexity of the source, the source position remains fixed throughout a MCNPX-PoliMi simulation. In order to fully simulate a realistic RPM measurement, however, it was important to capture the effects of a moving radiation source.

All sources tested in the laboratory and during benchmark experiments were small enough or far enough away from the RPM as to be treated as point sources. Assuming that the source would be moving at a constant speed past the RPM, the source could be represented as a line source for which radiation emissions are equally probable along the entire length of the line. One important parameter to be determined through simulations was an optimum measurement time for the RPM, i.e. as a pedestrian or vehicle approaches the RPM, when does one start and end the data acquisition. When screening a pedestrian one can assume the radiation background to be relatively constant. For much larger screening objects, like cargo containers, the ship effect may increase neutron background, while the terrestrial gamma-ray photon background will be

suppressed due to the cargo container's shielding effect [26]. Assuming constant background, there should be a diminishing signal to background return the further the source is away from the RPM.

For example, an RPM consisting of eight 7.62 cm diameter EJ309 liquid organic scintillators was modeled in MCPX-PoliMi, as shown in Figure 3-1. The length of the line source corresponds to the RPM measurement time assuming a user-defined source transit speed of 1.2 m/s for pedestrians [38]. For a given source strength, one can obtain a simulated RPM radiation count rate for different measurement times of a moving radiation source.

For a simulated 0.59 MBq ^{137}Cs source traveling at 1.2 m/s, Figure 3-2a shows the diminishing returns of increasing the RPM measurement time beyond 3 s, an ideal RPM measurement time found through other analysis methods as well [64]. As it would be impractical to develop a system in our laboratory to move radioactive sources at a constant speed parallel to the RPM, it was also desirable to determine a static measurement equivalent time to a three second dynamic measurement time. Figure 3-2b overlays RPM count rates as a function of static and dynamic source measurement times. One can see that for a three second dynamic source measurement an equivalent number of counts are recorded in the RPM for a two second static measurement of the same radioactive source.

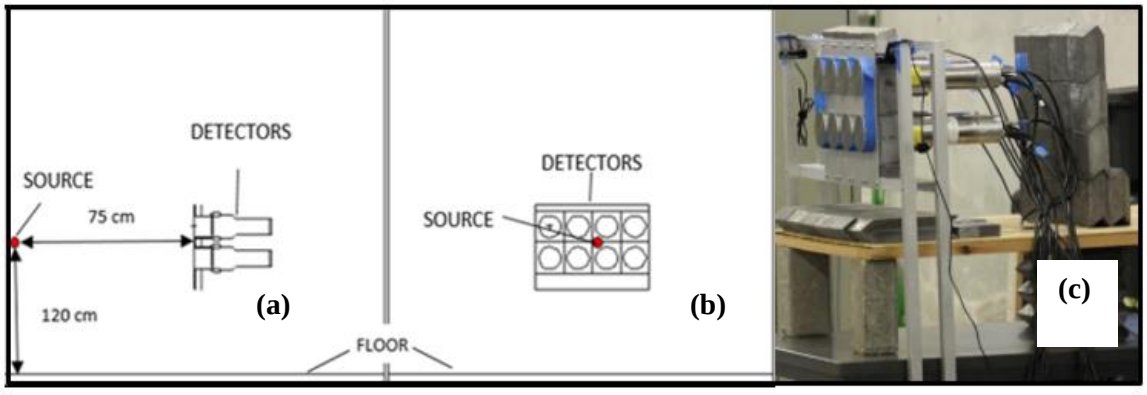

Fig. 3-1. (a) Side and (b) front view of an eight 7.62 cm diameter EJ309 cylindrical liquid scintillator RPM modeled in MCNPX-PoliMi and later built as a prototype (c). A 0.59 MBq ^{137}Cs line source is situated 75 cm parallel to RPM front face. The source is assumed to be moving at 1.2 m/s, and the length of the line source therefore represents the simulated measurement time [65].

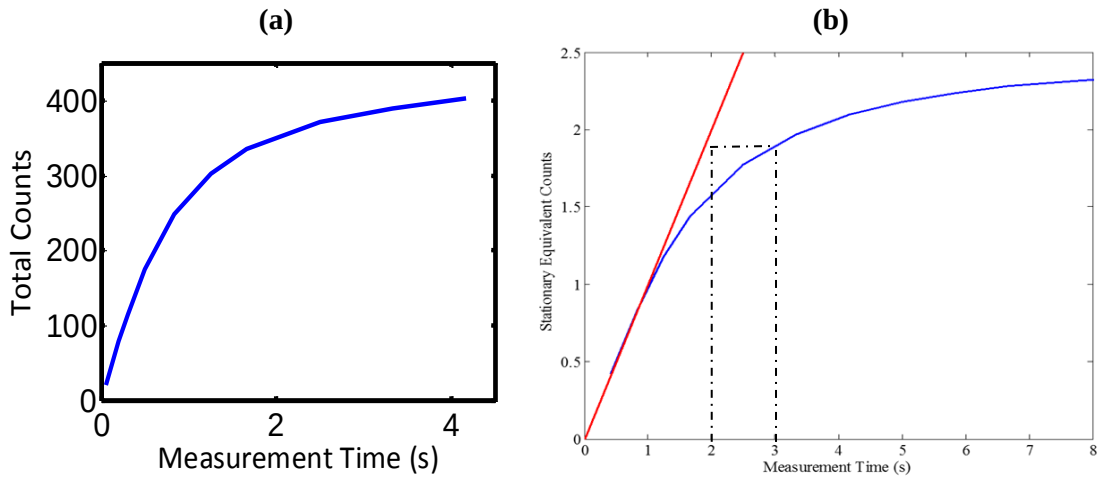

Fig. 3-2. (a) Simulated RPM gamma-ray photon count rates for setup from Figure 3-1 for a range of different measurement times simulated via changing the length of the line source. (b) Comparison count rates of a static (red) versus a dynamic (blue) source measurement to establish that a 3 s measurement for a source moving at 1.2 m/s can be reproduced in the laboratory with a 2 s static source measurement [65].

The type, shape, and number of detectors used in our RPM prototypes was determined through the use of receiver operating characteristics (ROC) curves, as explained further in Chapter 3.2. However, MCNPX-PoliMi simulations were also used to optimize the layout of the detectors in rows and columns, and the spacing between detectors. Differences in efficiency for the different layouts simulated were, in the end, relatively small, but these simulation results were used, for instance, to choose the two row and four column layout for the pedestrian RPM shown in Figure 3-1.

3.2. Establishing System False Alarm Rate and Minimum Detectable Activity Using Receiver Operating Characteristic Curves

3.2.1. What are Receiver Operating Characteristics Curves?

An ideal RPM would exhibit high absolute detection efficiency at low total detector and system cost. The size, type, and number of detectors dictates cost, but the detector with the highest intrinsic efficiency might not be the ideal RPM detector if it is costly and many are needed to achieve the desired absolute system efficiency. When comparing different RPM systems, two interlaced parameters are of great importance. On the one hand, the RPM should reliably alarm on some minimum detectable activity (MDA) source. On the other hand, the RPM

should exhibit a very low false alarm rate on natural background. As neutron nuisance alarms are exceedingly rare and any neutron RPM neutron alarm is treated very seriously, a very low neutron false alarm rate is particularly important.

Focusing on the example of neutron background and some MDA neutron source, one can represent the RPM neutron detection response to this source as two overlapping Poisson distributions, as shown in Figure 3-3. The user defines some neutron count rate as an alarm threshold, t_n, that should result in a very low false alarm rate, i.e. minimizes the area of the background neutron Poisson distribution that falls to the right of t_n. At the same time it is imperative that the probability of neutron alarming on the MDA source is high, i.e. minimize the area of MDA neutron source Poisson distribution that is to the left of t_n. Selecting an appropriate t_n is trivial if the background and MDA Poisson distributions are well separated, but much more challenging when they are overlapping, as they are in Figure 3-3.

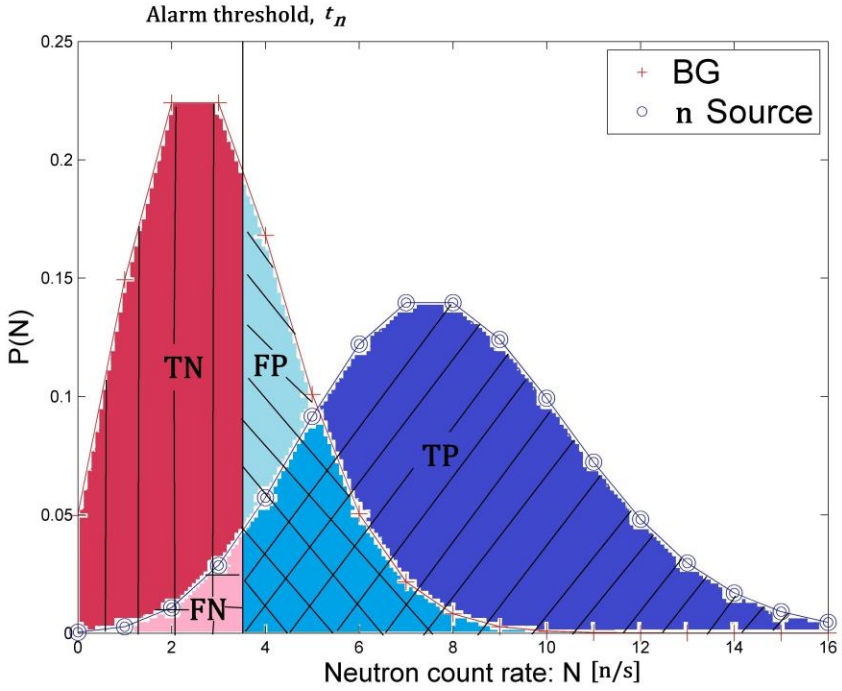

Fig. 3-3. Example of the probability of an RPM detecting N neutrons per second from a background and some MDA neutron Poisson distributions. For a user defined alarm threshold neutron count rate, t_n,the true negative rate, TN, is the probability of correctly not neutron alarming on neutron background, whereas the false negative rate, FN, is the probability of not alarming on the MDA neutron source. The false positive rate, FP, the false alarm rate probability on neutron background, whereas the true positive rate, TP, is the correct alarm rate on the neutron MDA source. [49]

The false alarm probability, P_{FP}, and true alarm probability, P_{TP}, can be calculated using equations (3-4) and (3-5), where μ_{BG} and μ_{SIG} are means of background and MDA neutron Poisson distributions:

$$P_{FP}(t_n, \mu_{BG}) = e^{-\mu_{BG}} \sum_{i=t_n}^{\infty} \frac{\mu_{BG}^i}{i!}, \tag{3-4}$$

$$P_{TP}(t_n, \mu_{BG}) = e^{-(\mu_{BG}+\mu_{SIG})} \sum_{i=t_n}^{\infty} \frac{(\mu_{BG}+\mu_{SIG})^i}{i!} \tag{3-5}$$

An ROC curve, like the one shown in Figure 3-4, can be obtained by computing P_{FP} and P_{TP} over a range of different alarm thresholds, t_n, and then plotting these two probabilities against each other. Looking at the ROC curve for an RPM allows one to find the desired false alarm probability, P_{FP}, and see if the corresponding true alarm probability, P_{TP}, for the MDA source is acceptable. This allows for an easy comparison between may different RPM systems.

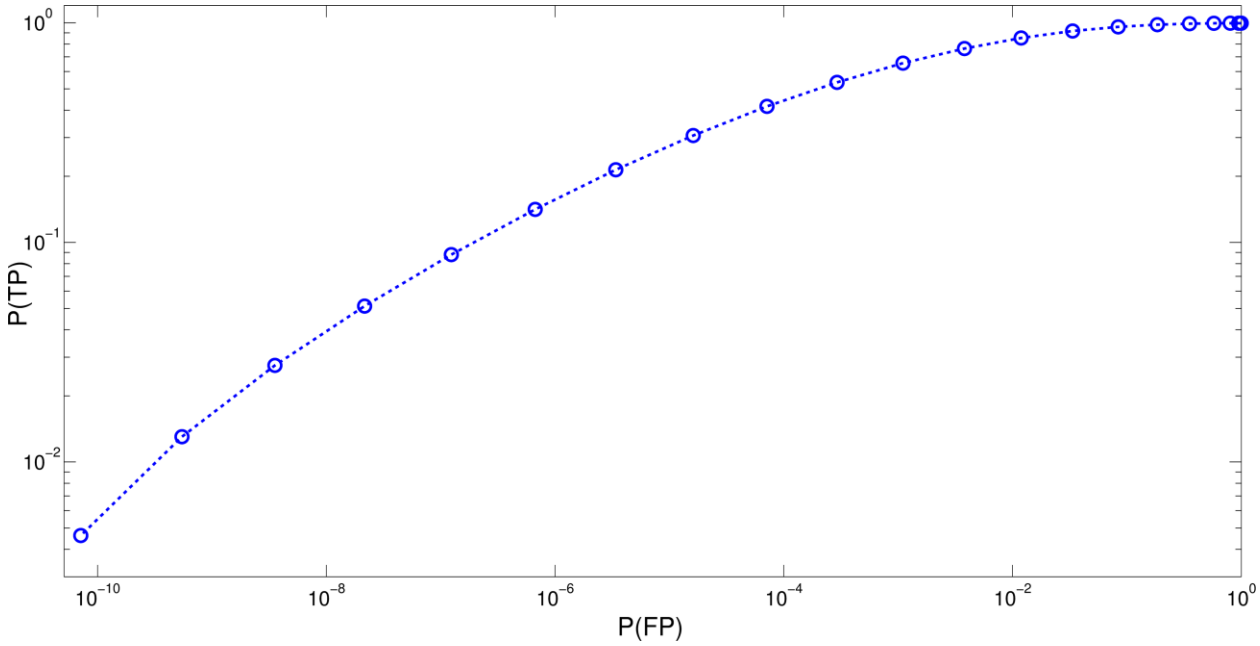

Fig. 3-4. Example of an ROC curve for the sample background and MDA source neutron Poisson distributions from Figure 3-3 [49].

3.2.2. Experimental Setup for Comparing Different Detectors for RPM Suitability

The three differently-shaped and sized liquid organic scintillation detectors from Table 2-1 and Figure 2-7 were compared amongst themselves and against the ^{3}He RPM described in section 2.3 using ROC analysis for a moderated ^{252}Cf source MDA scenario [49,66]. The setups, shown in Figure 3-5, included a 110,000 n/s ^{252}Cf source placed 100 cm from the detector front

face and shielded by a 10 cm thick HDPE slab. A 50-keVee light output threshold was applied to all organic liquid scintillators, corresponding to a neutron energy of approximately 470 keV. All three organic scintillators were gain matched by aligning the ^{137}Cs 478-keV Compton edge at a pulse height of 1.6 V using the CAEN DT5720 digitizer which features a 2 V dynamic range. This relatively high gain was intentionally chosen to preserve the ability of the RPM to detect low energy gamma-ray photon sources, such as ^{241}Am (60 keV gamma-ray photon) and ^{57}Co (122 keV gamma-ray photon). Using the PSD curves described in [49,66] and measurement times varying between 10 and 90 minutes, neutron count rates were obtained for all four detection setups pictured in Figure 3-5.

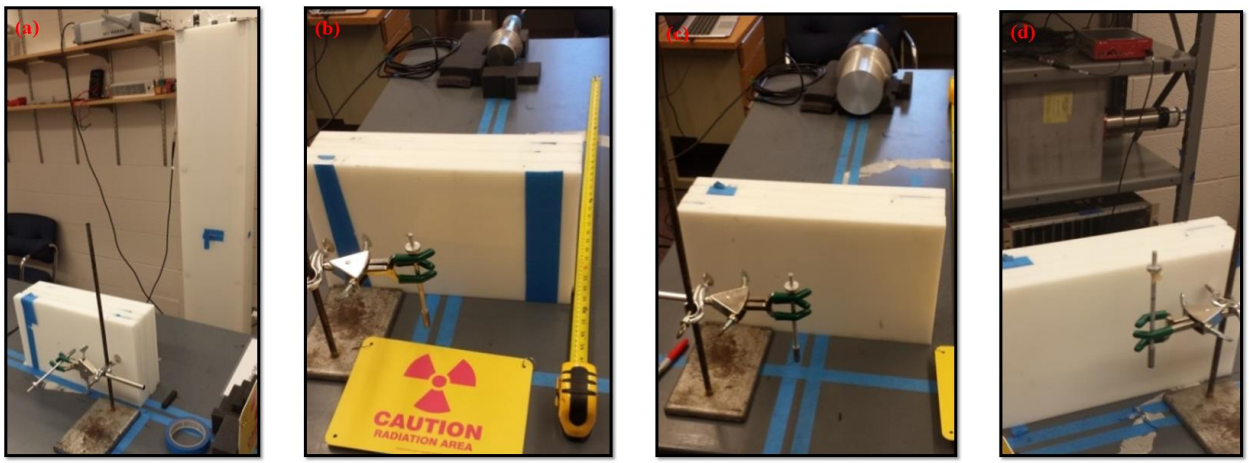

Fig. 3-5. (a) ^{3}He RPM, (b) 7.62 cm ∅ cylindrical EJ309, (c) 12.7 cm ∅ cylindrical EJ309, and (d) 25 cm x 25 cm x 10 cm BC501A; 110,000 n/s ^{252}Cf + 10 cm HDPE at 100 cm from detector front face [49].

3.2.3. Receiver Operating Characteristics Curve Results for Comparing Different Organic Liquid Scintillation Detector Shapes and Volumes

Table 3-1 lists the measured neutron count rates observed from background and the setups shown in Figure 3-5, as well as simulated neutron count rates obtained from MCNPX-PoliMi simulations of the same measurements. Measured and simulated neutron count rates agree well with the exception of the 25x25x10 cm^3 BC501A paddle. The measured and simulated PHDs for that detector are shown Figure 3-6. The fractional difference plot between measurement and simulation, shown in Figure 3-7, shows that measurement and simulation agree within ten to fifteen percent at light output over 250 keVee or 1.5 MeV neutron energy. The discrepancy of measured and simulated count rate for this largest volume detector thus arises from the lower pulse height region where overlapping of the neutron and gamma-ray photon

bands required a conservative PSD curve at the cost of low neutron energy detection efficiency [49]. A material with better PSD characteristics would allow one to operate at low thresholds without sacrificing neutron efficiency at lower energies [43,51,67].

Table 3-1. Measured and simulated neutron count rates for moderated ^{252}Cf setup shown in Figure 3-5 [49,66].

Neutron Count Rate	**Detector**	**^{3}He RPM**	**7.62 cm ∅ EJ309**	**12.7 cm ∅ EJ309**	**25x25x10 cm^3 BC501A**
Measured Background [n/s]		3.13 ± 0.02	0.24 ± 0.01	0.25 ± 0.01	2.60 ± 0.07
Measured [n/s]		373.3 ± 0.5	6.0 ± 0.1	17.6 ± 0.1	26.5 ± 0.2
Simulated [n/s], 100 cm		415.2 ± 2.6	6.1 ± 0.3	17.7 ± 0.2	82.2 ± 0.3

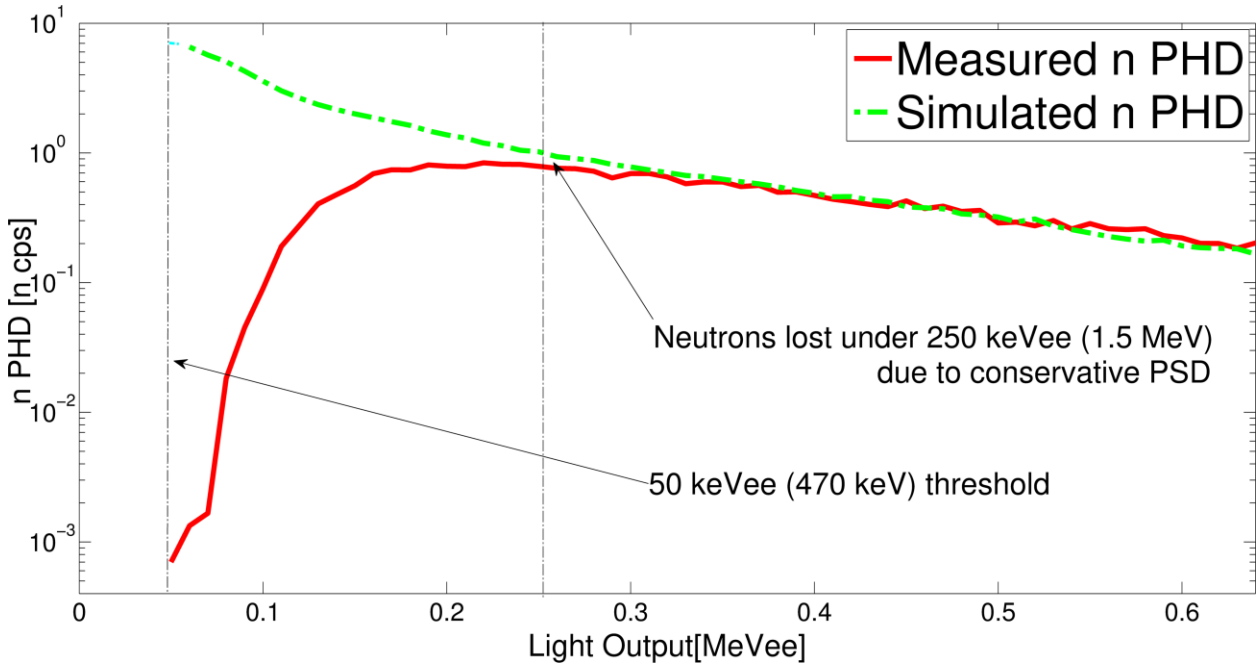

Fig. 3-6. Measured and MCNPX-PoliMi simulated neutron pulse height distributions for moderated ^{252}Cf measurement with 25x25x10 cm BC501A shown in Figure 3-5d [49].

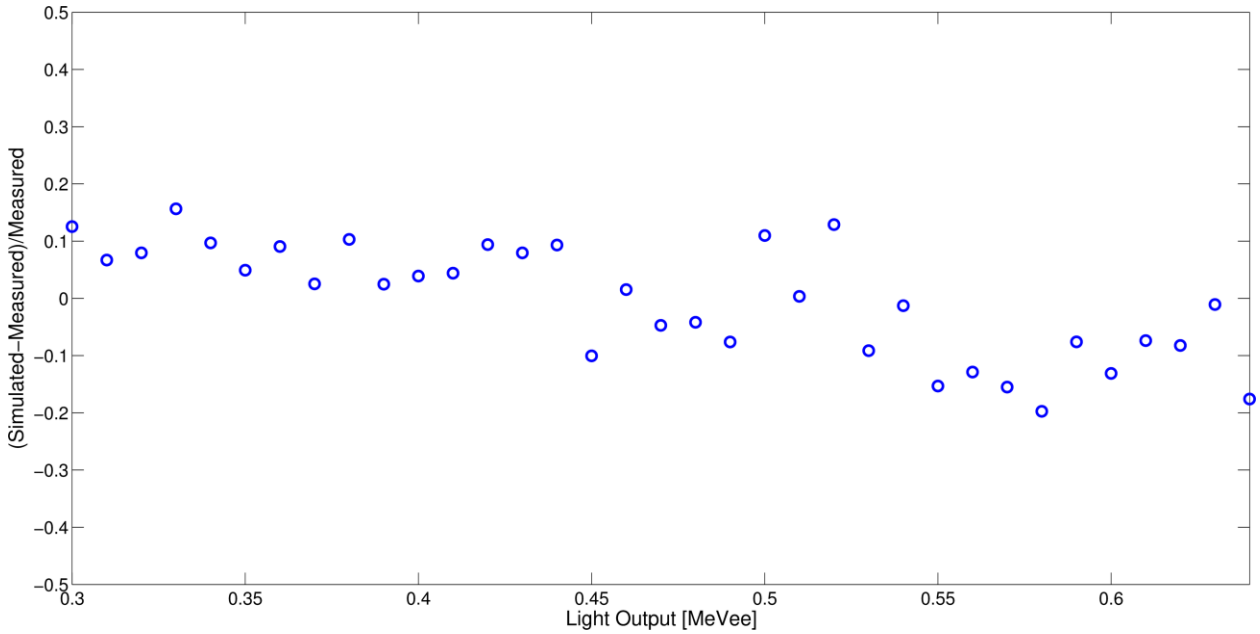

Fig. 3-7. Fractional difference plot for measured and simulated PHDs from figure 3-6, showing 10-15 percent agreement between measurement and simulation at light output over 300 keVee[49].

These measured neutron count rates were then scaled to a 20,000 n/s source strength to make the MDA scenario more challenging. The total counts for a two second measurement, equivalent to a three second dynamic measurement (see section 3.1.3.), was then used in equations (3-4) an (3-5) as μ_{SIG}, and the measured background count rates were modified accordingly to be used as μ_{BG} in the same equations. For this given MDA scenario and a desired false alarm rate of 1 in 10,000 [38,39] one can now create ROC curves to compare the four different detectors, as show in Figure 3-8. The ^{3}He RPM excels at this MDA scenario, while none of the single liquid organic scintillation detectors come close to the desired 100% true positive alarm probability. Increasing the size of the liquid detector from the 7.62 cm diameter EJ309 to the 12.7 cm diameter EJ309 exhibits a steep improvement in the ROC curve, but not much is gained from the increased volume of the 25x25x10 cm^3 BC501A due to the loss of neutron efficiency at lower energies because of the conservative PSD curve.

In terms of developing an RPM, one can easily scale this ROC analysis to determine how many of any given detector are needed to achieve a 100% true positive alarm probability for this MDA scenario while also not exceeding the desired 1 in 10,000 false alarm rate. ROC curves for different numbers of 7.62 cm diameter and 12.7 cm diameter EJ309 organic liquid scintillation detectors are shown in Figures 3-9 and 3-10. Data for a wide variety of different RPM

configuration scenarios are also summarized in Table 3-2. The ROC curve analysis suggests that this particular MDA neutron source scenario could therefore be satisfactorily detected with a 1 in 10,000 false alarm rate by using either eight 7.62 cm diameter cylindrical volume EJ309 organic liquid scintillation detectors, two 12.7 cm diameter cylindrical volume EJ309 organic liquid scintillation detectors, or three 25x25x10 cm^3 paddle-shaped BC501 organic scintillation detectors. As later described in Section 4.2, the pedestrian RPM using eight 7.62 cm diameter cylindrical volume EJ309 organic liquid scintillation detectors did indeed exhibit satisfactory neutron alarming performance for a very similar MDA neutron source test scenario.

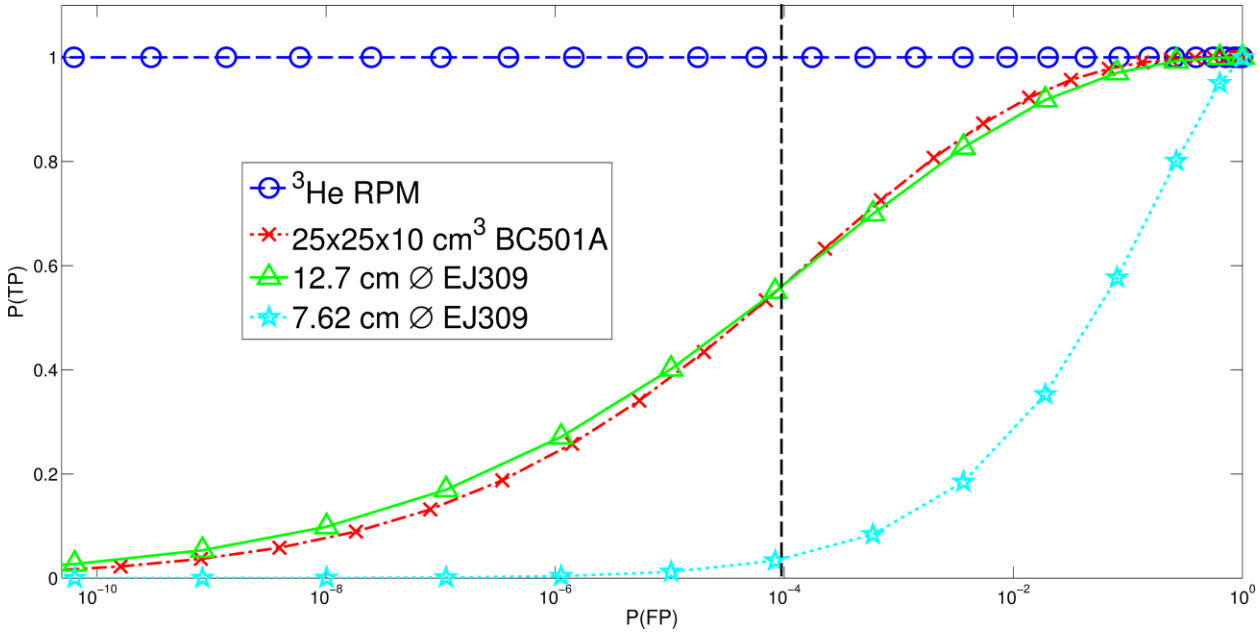

Fig. 3-8. ROC curve comparison of three different organic liquid scintillators and a ^{3}He RPM for the moderated ^{252}Cf setup from Figure 3-5 [49]. A 1 in 10,000 desired neutron false alarm rate is indicated by the dashed vertical black line [38].

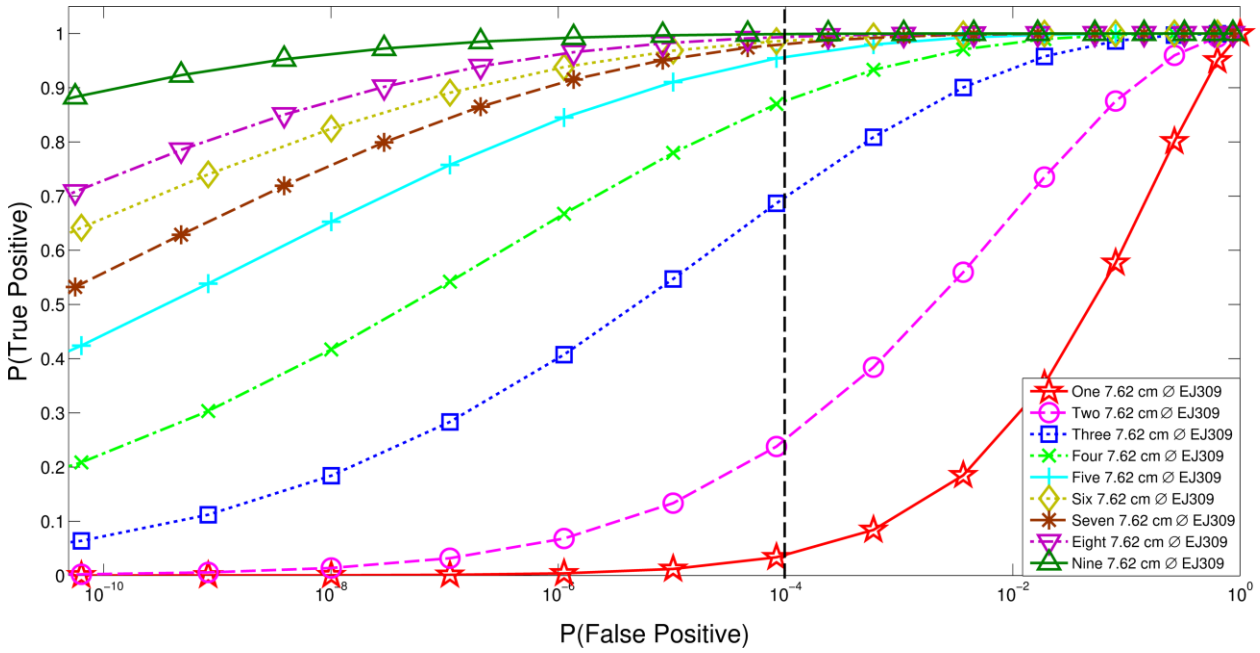

Fig. 3-9. ROC curve comparison of different number of 7.62 cm diameter EJ309 cylindrical active volume organic scintillation detectors for the moderated ^{252}Cf setup from Figure 3-5b [49]. A 1 in 10,000 desired neutron false alarm rate is indicated by the dashed vertical black line [38].

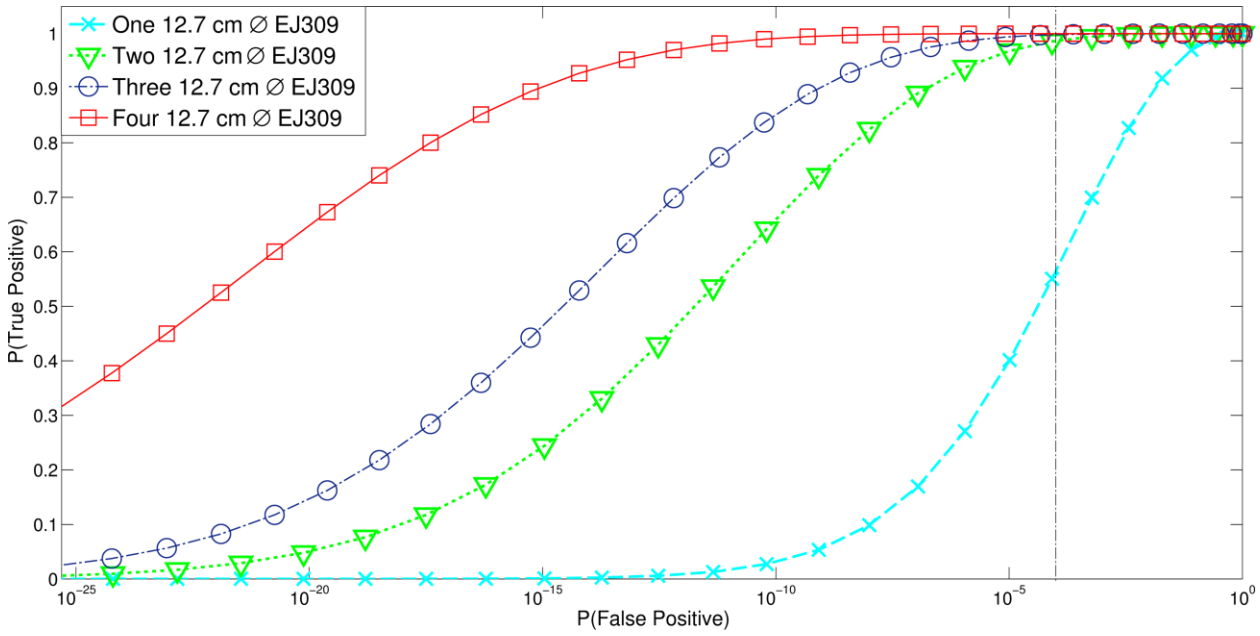

Fig. 3-10. ROC curve comparison of different number of 12.7 cm diameter EJ309 cylindrical active volume organic scintillation detectors for the moderated ^{252}Cf setup from Figure 3-5c [49]. A 1 in 10,000 desired neutron false alarm rate is indicated by the dashed vertical black line [38].

Table 3-2. Probabilities of a true alarm as a function of number of detectors and assuming a 1 in 10,000 false alarm rate for a 2 s measurement of a 20,000 n/s ^{252}Cf source placed 100 cm from the detector front face and shielded by 10 cm of HDPE, as show in the setups in Figure 3-5 [49].

Detector	P_{TA}
^{3}He RPM (3 tubes)	1
One 25x25x10 cm^3 BC501A	0.56
Two 25x25x10 cm^3 BC501A	0.91
Three 25x25x10 cm^3 BC501A	0.99
One 12.7 cm Ø EJ309	0.56
Two 12.7 cm Ø EJ309	0.99
Three 12.7 cm Ø EJ309	1
One 7.62 cm Ø EJ309	0.03
Four 7.62 cm Ø EJ309	0.71
Eight 7.62 cm Ø EJ309	0.96

3.3. Designing a Complete RPM System Architecture

Two RPM systems were designed and tested extensively in benchmark campaigns discussed in Chapter 4. The pedestrian RPM, depicted in Figure 3-11a, consisted of eight 7.62 cm diameter cylindrical volume EJ309 organic liquid scintillation detectors and used a CAEN V1720 digitizer board. The vehicle RPM, depicted in Figure 3-11b, consisted of four 12.7 cm diameter cylindrical volume EJ309 organic liquid scintillation detectors and one 25x25x10 cm^3 paddle-shaped BC501 organic scintillation detector. Based upon measurements and simulations, ideally the vehicle RPM would have contained two or more 25x25x10 cm^3 paddle-shaped BC501 organic scintillation detectors, but due to planning and logistics constraints, the 12.7 cm diameter EJ309 liquids were used as an adequate substitute. The vehicle RPM used a CAEN V1730 digitizer board.

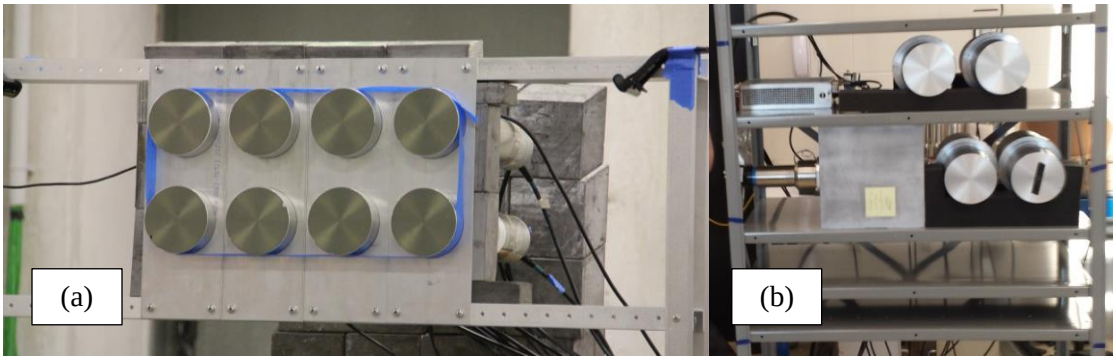

Fig. 3-11. (a) Pedestrian RPM consisting of eight 7.62 cm diameter cylindrical volume EJ309 organic liquid scintillation detectors; (b) vehicle RPM consisting of four 12.7 cm diameter EJ309 cylindrical active volume organic scintillation detectors and one 25x25x10 cm^3 BC501A liquid detector. Both RPMs used two web-cameras and motion detection software as a makeshift occupancy sensor [40,41].

In order to trigger a measurement, a makeshift occupancy sensor had to be constructed. Two USB commercial web-cameras pointing in opposite directions were used in conjunction with motion detection freeware [68]. Assuming a constant source-transit speed, such as 1.2 m/s for the pedestrian RPM, and assuming a three second measurement time, we measured out the distances to the left and right of the RPM at which we wished to trigger the three second data acquisition. The motion detection software uses a mask for which the user defines the region of the image in which any image change, i.e. motion, triggers a motion detection event. An example of a mask and an image taken at the time of a motion trigger event are shown in Figure 3-12. A low resolution trigger picture was saved for each trigger for debugging purposes, and to filter out any unintended trigger events.

Any time motion is detected a three second data acquisition is triggered. A modified near real-time data acquisition and processing software was used. This script was originally developed by Alexis Poitrasson-Riviere for the DNNG Dual Particle Imager [69,70]. Acquired pulses are passed from the digitizer buffer to the DAQ in packets which then have PSD applied to them to build up gamma-ray photon and neutron count rates as well as PHDs. Within a few seconds of the RPM measurement finishing, a standardized XML file containing relevant measurement data is created. The XML file contains information on what type of alarm was registered (no alarm, gamma alarm, neutron alarm) and lists parameters such as measured

gamma-ray and photon count rates and, in the case of a gamma alarm, what radionuclide was identified.

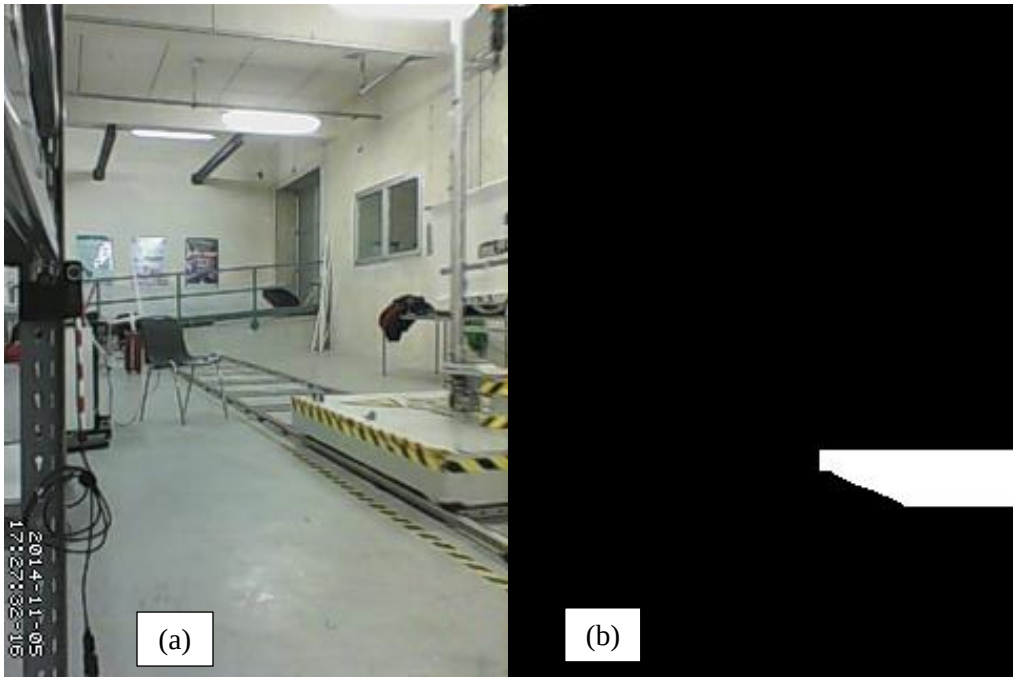

Fig. 3-12. (a) Example of a trigger picture captured by the vehicle RPM occupancy sensor [40]. (b) The motion detection software [68] will signal that motion has been detected if the image in the white portion of this mask changes. Separate masks are used to detect motion approaching from the left and right of the RPM.

Chapter 4
Testing RPM Prototypes Under Real-World Conditions

The two RPM prototypes described Chapter 3 needed to be rigorously tested with a variety of moving gamma-ray photon and neutron sources, including SNM. The majority of data was collected in two extended measurements trips to an RPM testing facility in Italy in 2014.

4.1. The European Commission SCINTILLA RPM Testbed Facility

Testing conditions and scenarios for RPMs are outlined in the ANSI standard N42.35 [38] and IAEA-TECDOC-1312 [71]. A number of RPM testbeds with appropriate facilities and nuclear and radiological reference sources have been developed around the world. We were granted access to the European Commission's RPM testbed at the JRC in Ispra, Italy. Data were collected with the pedestrian RPM (see Chapter 3.3) for two weeks in February 2014 and with the vehicle RPM (see Chapter 3.3) for two weeks in November 2014.

The JRC RPM testbed is an indoor facility consisting of an electric rail-cart system. Sources are placed in an adjustable source holder with a 2.1 m maximum source height. The maximum possible source transit speed is 3 m/s, though the ANSI standard only calls for 1.2 m/s for pedestrian RPMs and 2.2 m/s for vehicle RPMs. Sources can be shielded with a variety of common shield materials, like lead, steel, and HDPE. The facility has been used for a variety of RPM test campaigns, like ITRAP+10 [72]. We participated in the 2nd and 3rd of three RPM benchmark campaigns that were part of the European Commission's SCINTILLA project which was launched in 2012 to develop and test new technologies for detecting nuclear and radiological materials. The SCINTILLA component relevant to us focused on the development and testing of ^{3}He-free RPM systems [73]. The facility is shown in Figure 4-1.

Other invited participants at SCINTILLA included representatives from the French Alternative Energies and Atomic Energy Commission (CEA), SAPHYMO, Istituto Nazionale di Fisica Nucleare (INFN), Ansaldo Nucleare, symetrica, Arktis Radiation Detectors and others. Detector materials used by these institutions included PSD capable plastic organic scintillators

[74], gadolinium capture-gated plastic scintillators [75], and ^{6}LiZnS(Ag) [76]. All laboratories and companies provided their own ^{3}He-free systems for testing. During official benchmark measurements, all RPMs were operated by JRC staff and modifications or interventions by the RPM designers were prohibited.

Fig. 4-1. RPM testing facility at European Commission JRC Ispra, Italy. Left: 2nd SCINTILLA benchmark campaign in February 2014. Right: Electric rail cart system. (Photo credit: JRC Ispra).

^{252}Cf was used as a source of spontaneous fission neutrons for all neutron alarm tests. Most tests were performed with ANSI recommended 20,000 n/s activity ^{252}Cf sources [38], though tests also included weaker sources with activities of 7,000, 10,000, and 13,000 n/s. All neutron alarm tests included a 0 cm, 4 cm, or 8 cm thick HDPE moderator sphere for the ^{252}Cf. neutron source.

The ANSI RPM standards lists a number of recommended gamma-ray photon emitting radionuclides and activities with which to test RPM gamma-ray alarm sensitivities. Table 4-1 shows that all sources used at the two SCINTILLA benchmarks were of approximately the recommended activity. No ^{232}Th source was available for testing, even though it is an ANSI recommended source. A number of medical isotopes were originally planned to be part of the SCINTILLA benchmarks, but had to be left out due to issues with the JRC cyclotron. A host of medical isotopes, including ^{99m}Tc, ^{18}F, ^{67}Ga, ^{111}In, ^{123}I, ^{131}I and ^{201}Tl were measured in June 2016 at the University of Michigan's C.S. Mott Children's Hospital.

Table 4-1. Gamma-ray photon source activities for ANSI recommended sources as well as activities used at the two SCINTILLA RPM benchmark experiments at the JRC Ispra in February and November 2014.

Source	Source Activity [kBq] (ANSI) [38]	Source Activity [kBq] (2nd SCINTILLA, pedestrian RPM) [39]	Source Activity [kBq] (3rd SCINTILLA, vehicle RPM) [40,77]
^{57}Co	185	204	262
^{133}Ba	518	301	212
^{137}Cs	592	370	350
^{60}Co	259	259	181
^{232}Th	517	NA	NA
^{241}Am	1740	2220	2200
HEU	NA	51 g; 89.9 % ^{235}U	NA
WGPu	NA	6.6 g; 93% ^{239}Pu	6.6 g; 93% ^{239}Pu

4.2. RPM False Alarm Tests

False alarms are defined as radiation alarms in the presence of no external radiation source except natural background radiation. Unless the neutron and gamma-ray photon alarm threshold are set incredibly high, there always exists some non-zero probability of fluctuations in background radiation resulting in a false alarm. The ANSI RPM standards require a 1 in 10,000 false alarm rate. This means that in 10,000 occupancies the RPM should register no more than one false alarm. In practice, an even lower false alarm rate is highly desirable. To test RPM false alarm rates at SCINTILLA, the electric cart was run for thousands occupancy passages overnight with no radiation sources placed on the cart. Alarm rates were set at five standard deviations above mean background. For the pedestrian RPM the alarm threshold settings were 8 neutrons and/or 3,856 gamma-ray photons measured in three seconds [39]. For the vehicle RPM the alarm threshold settings were 14 neutrons and 11,044 gamma-ray photons. For the pedestrian RPM at the 2nd SCINTILLA benchmark our RPM recorded zero false alarms in the 2,739 overnight RPM occupancies. For the vehicle RPM at the 3rd SCINTILLA benchmark our RPM recorded zero false alarms in 1,781 overnight RPM occupancies. While the lack of false alarms is encouraging in these data, a larger dataset would have been preferable given more time. Histograms of the pedestrian RPM false alarm rate test data are shown in Figure 4-2.

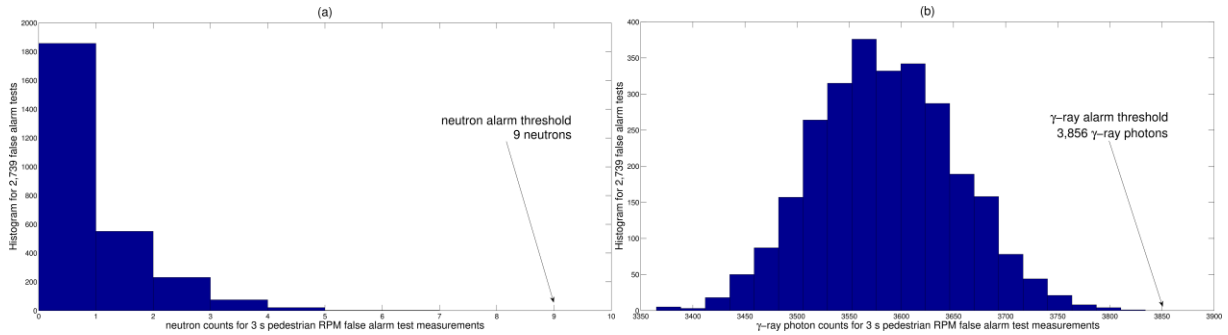

Fig. 4-2.Histograms of measured (a) neutrons and (b) gamma-ray photons in 2,739 three second measurements for the false alarm test for the pedestrian RPM during the 2nd SCINTILLA benchmark in February 2014 at the European Commission JRC in Ispra, Italy. The alarm thresholds shown are set five standard deviations above the mean background count rates.

4.3. RPM Neutron Alarm Tests

4.3.1. Pedestrian RPM Neutron Alarm Results

ANSI standards [38] for pedestrian RPMs require the RPM to alarm at least 59 out of 60 times on a 20,000 n/s ^{252}Cf moving at 1.2 m/s (2.7 miles per hour, 4.3 kilometers per hour) at a source to single pillar RPM distance of 1 m. The neutron source is to be placed at a 1.2 m source height. The same test is to be repeated with the neutron source shielded with 4 cm thick HDPE moderator. The test is also to be repeated at a range of source heights to test the RPM sensitivity to sources high off of or low to the ground.

Neutron alarm tests were included in the February 2014 2nd SCINTILLA benchmark. As the DNNG system is eventually intended as a two pillar system, a source to detector distance of 70 cm was used. This reduced distance doubles the observed RPM radiation count rates based upon the one over distance squared dependence of the RPM solid angle relative to the radiation source.

Due to time constraints, most tests were only run for 30 repetitions as opposed to the prescribed 60 iterations. In order to go beyond the ANSI standards, several even more challenging scenarios were tested. These included elevated source speeds of 2.2 m/s and 3 m/s, a reduced source activity of 10,000 n/s, and an increased HDPE moderator thickness of 8 cm. Detailed neutron alarm test conditions and results are included in Table B-1 in Appendix B. A subset of these results are highlighted in Table 4-2. These results show that the pedestrian RPM met the basic ANSI standards. Many beyond ANSI standard tests were successfully passed as well, though the RPM struggled when multiple parameters went well beyond the ANSI standard, such as the combination of a halved source activity, doubled HDPE shielding, and elevated source transit speed.

Table 4-2. Highlights of February 2014 2nd SCINTILLA benchmark pedestrian RPM neutron alarm test results [39,41] for ANSI [38] and beyond ANSI standard test conditions using a 10,000 n/s or 20,000 n/s ^{252}Cf source with 1 cm steel and 0.5 cm lead shielding. Underlined values indicate parameters set at beyond ANSI standard for pedestrian RPM. Full neutron alarm dataset may be found in Table B-1 in Appendix B.

ANSI Standard Tests					
Activity [n/s]	**Speed [m/s]**	**HDPE [cm]**	**Source Height [m]**	**Average n counts**	**Neutron Alarms**
20,000	1.2	0	1.2	63	30/30
20,000	1.2	4	1.2	24	30/30
Beyond ANSI Standard Tests					
20,000	2.2	0	1.2	30	30/30
20,000	3	0	1.2	23	30/30
20,000	2.2	0	1.9	22	60/60
20,000	2.2	0	2.1	20	30/30
10,000	1.2	0	1.2	23	30/30
10,000	2.2	0	1.2	15	28/30
20,000	2.2	4	1.2	15	30/30
10,000	1.2	4	1.2	9	17/30
10,000	2.2	4	1.2	8	15/30
20,000	1.2	8	1.2	14	29/30
20,000	2.2	8	1.2	8	14/30
10,000	1.2	8	1.2	6	5/30
10,000	2.2	8	1.2	3	0/30

To visualize the test results, neutron counts per trial were extracted from the XML files, like the one in Figure A-1 in Appendix A, for the various neutron alarm test cases described in Table 4-2 and Table B-1 in Appendix B. Figure 4-3 shows the pedestrian RPM neutron count distribution shifting downwards when the source transit speed is increased from 1.2 m/s (4.3 km/h) to 3 m/s (10.8 km/h). In both cases, however, the neutron count distribution remains well above the 9 neutron alarm threshold, thus resulting in a perfect pass rate for these test scenarios.

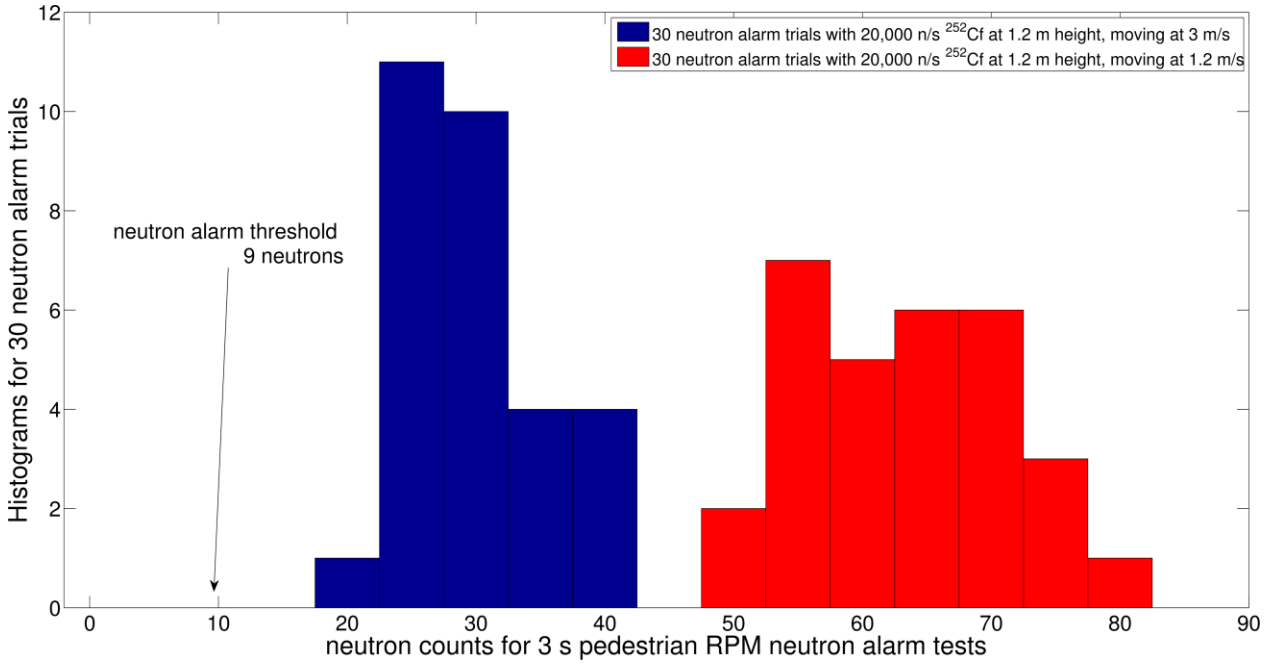

Fig. 4-3. Histograms of measured neutrons for 30 three second measurements of an unshielded 20,000 n/s ^{252}Cf moving at 1.2 m/s (red) or 3 m/s (blue). These histograms correspond to the data from folders 2 (red) and 3 (blue) in Table B-1 in Appendix B. These measurements were part of the pedestrian RPM neutron alarm testing during the 2nd SCINTILLA benchmark in February 2014 at the European Commission JRC in Ispra, Italy [39,41]. The 9 neutrons alarm threshold shown is set five standard deviations above the mean background count rate.

The effects of adding increasing amounts of HDPE shielding around the ^{252}Cf neutron source are shown in the histograms in Figure 4-4. The unshielded source results in neutron counts in the pedestrian RPM that are consistently well above the 9 neutron alarm threshold. The addition of 4 cm of HDPE shielding, however, shifts the neutron counts distribution to much lower neutron counts on average, thus even resulting in one undetected trial out of thirty trials. The addition of 8 cm of HDPE shielding moves the lower end of the neutron distribution to just above the 9 neutron alarm threshold. Keeping all other parameters constant, any further increase in the shielding thickness would undoubtedly detrimentally affect the ability of the pedestrian RPM to reliably detect the shielded neutron source.

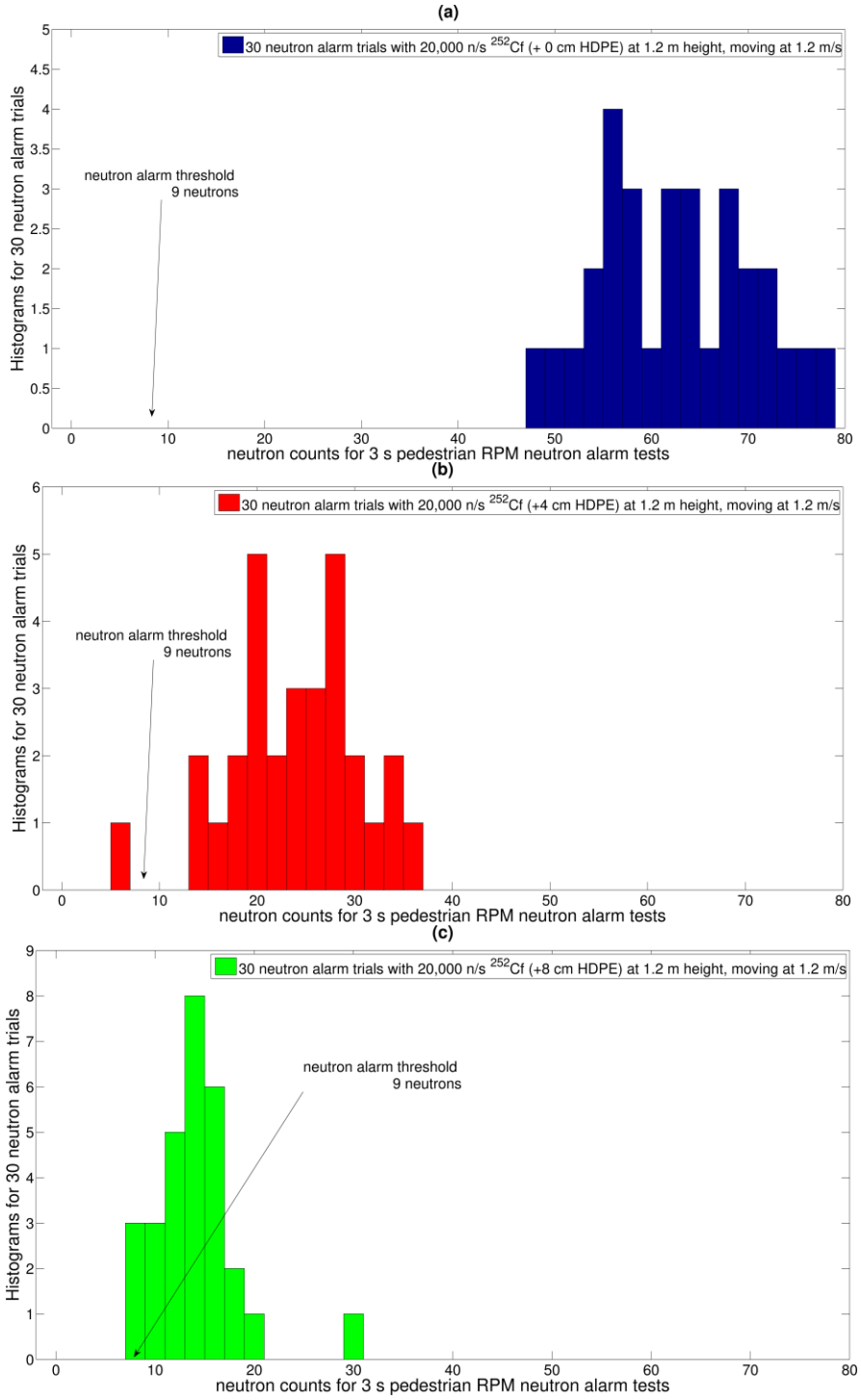

Fig. 4-4. Histograms of measured neutrons for 30 three second measurements of a 20,000 n/s ^{252}Cf moving at 1.2 m/s past the pedestrian RPM. Histograms are shown for tests with different amounts of HDPE shielding around the neutron source: (a) unshielded, (b) 4 cm thick HDPE, and (c) 8 cm thick HDPE. These histograms correspond to the data from folders (a) 2, (b) 16, and (c) 10 in Table B-1 in Appendix B. These measurements were part of the pedestrian RPM neutron alarm testing during the 2nd SCINTILLA benchmark in February 2014 at the European Commission JRC in Ispra, Italy [39,41]. The 9 neutrons alarm threshold shown is set five standard deviations above the mean background count rate.

Finally, some test cases that went above and beyond the basic ANSI standards [38] give us an idea of the limitations of the current system. In Figure 4-5, three different test scenarios are depicted in which the pedestrian RPM failed to neutron alarm on the ^{252}Cf source more than 50% of the time. All three of these cases involve 8 cm of HDPE source shielding, as well as a reduced source activity and/or an elevated source transit speed. Overall, nevertheless, the pedestrian RPM showed strong performance in its ability to reliably detect neutron source under a variety of different circumstances.

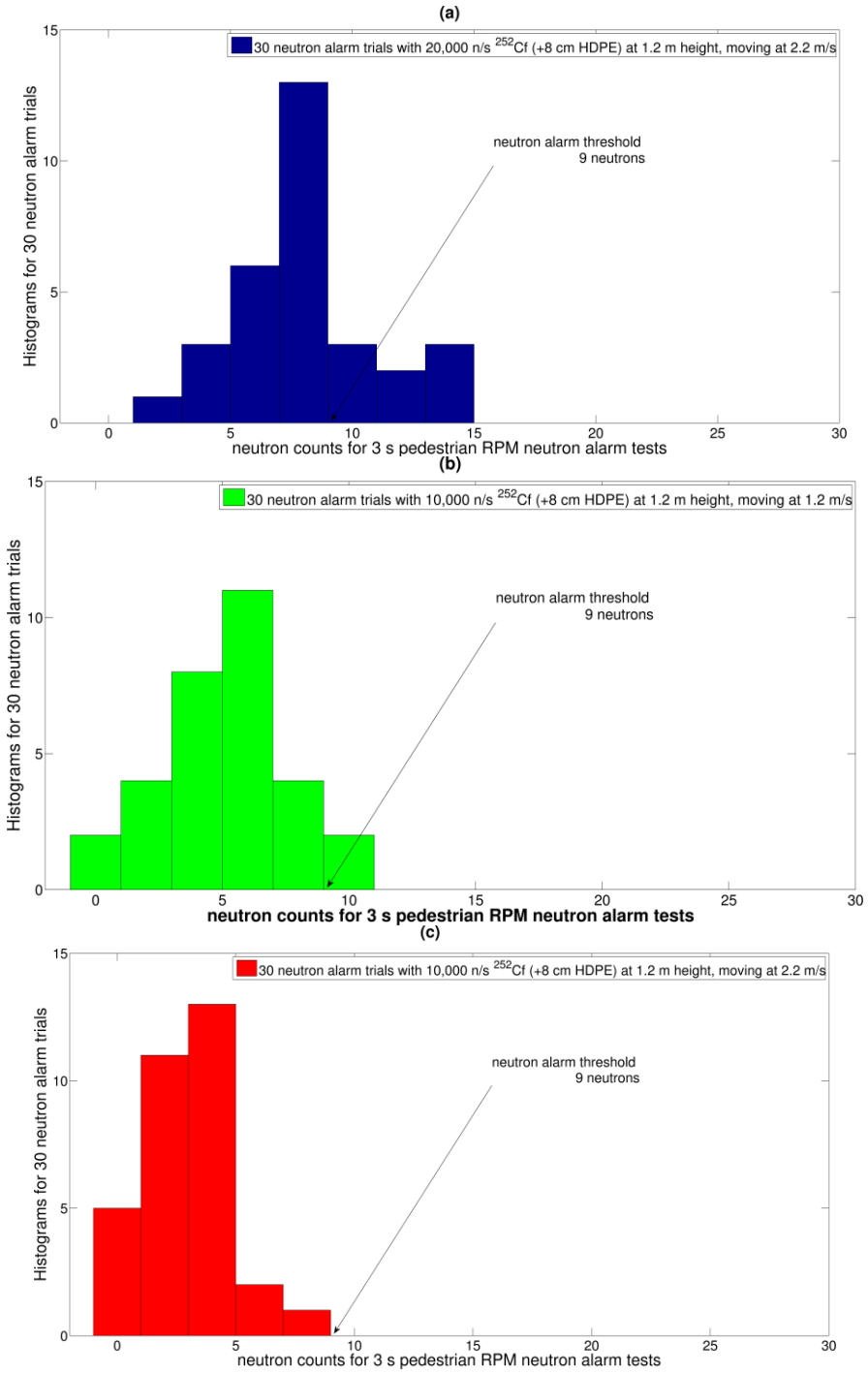

Fig. 4-5. Histograms of measured neutrons for 30 three second measurements of a ^{252}Cf source from the pedestrian RPM neutron alarm testing during the 2nd SCINTILLA benchmark in February 2014 at the European Commission JRC in Ispra, Italy [39,41]. All three cases involve test scenarios well beyond ANSI standard neutron alarming test conditions [38] and a majority of runs resulted in neutron counts below the 9 neutrons alarm threshold which is set five standard deviations above the mean neutron background count rate. The three test cases shown are: (a) 20,000 n/s ^{252}Cf with 8 cm HDPE shielding and moving at 2.2 m/s, (b) 10,000 n/s ^{252}Cf with 8 cm HDPE shielding and moving at 1.2 m/s, and (c) 10,000 n/s ^{252}Cf with 8 cm HDPE shielding and moving at 2.2 m/s. These histograms correspond to the data from folders (a) 9, (b) 12, and (c) 11 in Table B-1 in Appendix B.

4.3.2. Vehicle RPM Neutron Alarm Results

The ANSI standards for vehicle RPMs differ only in a few areas from those described already in 4.3.1 for pedestrian RPMs [38]. The source transit speed for vehicle RPM testing is prescribed to be 2.2 m/s, as opposed to the slower 1.2 m/s for pedestrian RPMs. The distance between vehicle RPM panels is set at 5 m. Our vehicle RPM consisted of a single panel at 2.5 m from the source rail track center.

Our vehicle RPM (see section 3.3 and Figure 3-11b) was tested during the 3rd SCINTILLA benchmark at the European Commission JRC in Ispra, Italy, in November 2014. Once again, due to time constraints most neutron alarm tests were run for fewer than the ANSI [38] recommended 60 trials. The ^{252}Cf source activities used for these experiments were 7,000 n/s, 13,000 n/s, and the ANSI [38] recommended 20,000 n/s. The source height used was 1.1 m instead of the usual 1.2 m. No 4 cm HDPE shielded neutron source tests were performed, as all participants agreed that their systems would easily pass this scenario. Therefore only iterations of the more challenging 8 cm HDPE shielded ^{252}Cf were run.

The full set of neutron alarm test results for our vehicle RPM are presented in Table 4-3. The vehicle RPM passed all basic neutron alarm tests with perfect marks. Tests with the ^{252}Cf at elevated heights of 2.1 m and 2.7 m posed no challenges. Performance for detecting the unshielded but weaker activity 7,000 n/s and 13,000 n/s ^{252}Cf sources ranged from modest to good. Performance for the 8 cm HDPE shielded ^{252}Cf trials, however, was poor, especially when using any of the lower activity neutron sources. Overall, the performance for neutron alarming was quite satisfying.

Table 4-3. Results of November 2014 3rd SCINTILLA benchmark vehicle RPM neutron alarm test results [40,77] for ANSI [38] and beyond ANSI standard test conditions using 7,000 n/s, 13,000 n/s, or 20,000 n/s ^{252}Cf sources with 1 cm steel and 0.5 cm lead shielding. Underlined values indicate parameters set at beyond ANSI standard for vehicle RPM.

Cf Activity (n/s)	Speed (m/s)	HDPE (cm)	Source Height (m)	Passages	Alarms
ANSI standard tests					
20,000	2.2	0	1.1	52	52
20,000	1.2	0	1.1	32	32
Beyond ANSI standard tests					
20,000	2.2	8	1.1	34	11
20,000	1.2	8	1.1	32	21
13,000	2.2	0	1.1	32	30
13,000	1.2	0	1.1	31	31
13,000	2.2	8	1.1	32	4
13,000	1.2	8	1.1	30	17
7,000	2.2	0	1.1	34	18
20,000	2.2	0	2.1	32	32
20,000	2.2	0	2.7	32	32

4.4. RPM Gamma-Ray Photon Alarm Tests

4.4.1. Pedestrian RPM Gamma-Ray Photon Alarm Results

This section concerns only the ability to alarm on the presence of the gamma-ray photon sources. The ability to identify radionuclides based upon gamma-ray photon measurements with the RPMs is discussed separately in Chapter 5. The testing conditions for gamma-ray photon alarming are very similar to those already described for neutron alarm tests in section 4.3; a list of ANSI prescribed sources and source activities were listed previously in Table 4-1. All sources are to be detected in at least 59 out of 60 iterations with the source moving at 1.2 m/s at a source height of 1.2 m. A single pillar RPM is to be placed 1 m from the source track [38].

Gamma-ray photon alarm tests were performed with the pedestrian RPM at the 2nd SCINTILLA benchmark at the European Commission JRC in Ispra, Italy, in February 2014 [39,41]. The gamma-ray photon sources and source activities used are listed in Table 4-1 and differ from the ANSI required source activities. Most gamma-ray photon sources used are of

lower activity, thus making the tests more challenging. The one exception is ^{241}Am, for which a higher than prescribed activity source was used. Additionally, two SNM sources were included in the gamma-ray photon alarm tests. These were a 6.6 g WGPu plutonium-oxide sample (93% ^{239}Pu), as well as a 51 g HEU (89.9 % ^{235}U) sample. Due to time constraints, typically only 30 trials were run per source scenario rather than the ANSI prescribed 60 trials. Up to 3 cm of steel source shielding was included in some measurements. The full list of test scenarios and pedestrian RPM results are listed in Table 4-4.

Table 4-4. Results of February 2014 2nd SCINTILLA benchmark pedestrian RPM gamma-ray photon alarm test results [40,77] for ANSI [38] and beyond ANSI standard test conditions using a variety of gamma-ray photon sources, including SNM. More detailed information on these trials can also be found in Table B-1 in Appendix B folders 17-40.

Source	Activity [kBq]	Source Speed [m/s]	Source Height [m]	Steel Shielding [cm]	Average γ counts	Gamma-Ray Alarms
^{57}Co	204	1.2	1.2	0	4021	29/30
^{57}Co	204	2.2	1.2	0	3867	15/30
^{133}Ba	110	1.2	1.2	0	4004	30/30
^{133}Ba	110	2.2	1.2	0	3877	22/30
^{133}Ba	301	1.2	1.2	0	4808	30/30
^{133}Ba	301	1.2	2.0	0	4239	30/30
^{133}Ba	301	2.2	1.2	0	4432	30/30
^{133}Ba	301	2.2	2.5	0	3945	28/30
^{137}Cs	370	1.2	1.2	0	4635	30/30
^{137}Cs	370	2.2	1.2	0	4298	30/30
^{137}Cs	3700	1.2	1.9	3	5648	30/30
^{137}Cs	3700	2.2	2.1	3	4839	30/30
^{60}Co	259	1.2	1.2	0	4572	30/30
^{60}Co	259	2.2	1.2	0	4277	30/30
^{60}Co	259	1.2	2.0	0	4212	30/30
^{60}Co	259	2.2	2.5	0	3944	29/30
^{241}Am	2220	1.2	1.2	0	4025	30/30
^{241}Am	2220	2.2	1.2	0	3864	18/30
HEU	51 g	1.2	1.2	0	4502	30/30
HEU	51 g	2.2	1.2	0	4223	30/30
WGPu	6.6 g	1.2	1.2	0	5381	30/30
WGPu	6.6 g	2.2	1.2	0	4757	30/30
WGPu	6.6 g	1.2	1.2	1	4546	30/30
WGPu	6.6 g	2.2	1.2	1	4215	30/30

Overall the pedestrian RPM performed very well. Nearly all test scenarios resulted in perfect detection rates. Figure 4-6a shows that the pedestrian RPM can easily detect the 6.6 g WGPu sample, while Figure 4-6b shows that this statement holds even when the source transit speed is raised to 2.2 m/s. Figure 4-6c shows the effects of adding 1 cm thick steel source shielding, which further lower the average number of gamma-ray photons detected by the pedestrian RPM, but still results in a 100% detection rate.

The 51 g HEU sample was also reliably detected, as shown in Figure 4-7a. However, the pedestrian RPM exhibits the most difficulty with low energy gamma-ray photon sources, like ^{241}Am. Despite using source activity almost 30% higher than prescribed by ANSI [38], Figure 4-7b shows that the pedestrian RPM alarm threshold is barely low enough to reliably alarm on the ^{241}Am source travelling at 1.2 m/s. When the source transit speed is raised to 2.2 m/s the successful detection rate drops to 60%, as shown in Figure 4-7c.

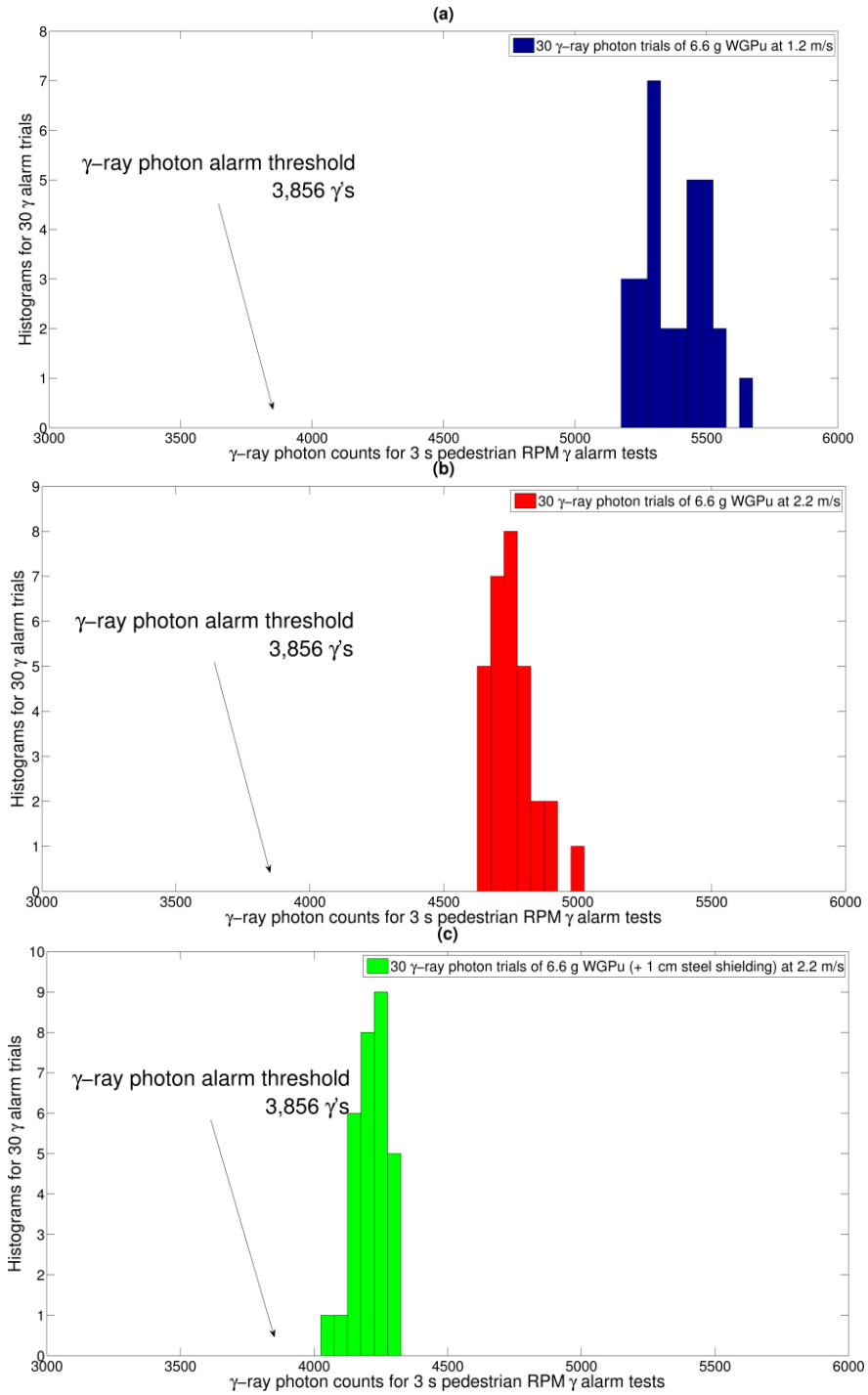

Fig. 4-6. Histograms of measured gamma-ray photons for 30 three second measurements of a 6.6 g sample of WGPu moving at 1.2 m/s past the pedestrian RPM. Histograms are shown for different test scenarios: (a) 1.2 m/s source transit speed; source unshielded, (b) 2.2 m/s source transit speed; source unshielded, and (c) 2.2 m/s source transit speed; source shielded with 1 cm steel. These histograms correspond to the data from folders (a) 21, (b) 22, and (c) 23 in Table B-1 in Appendix B. These measurements were part of the pedestrian RPM gamma-ray photon alarm testing during the 2nd SCINTILLA benchmark in February 2014 at the European Commission JRC in Ispra, Italy [39,41]. The 3,856 gamma-ray photons alarm threshold shown is set five standard deviations above the mean background count rate.

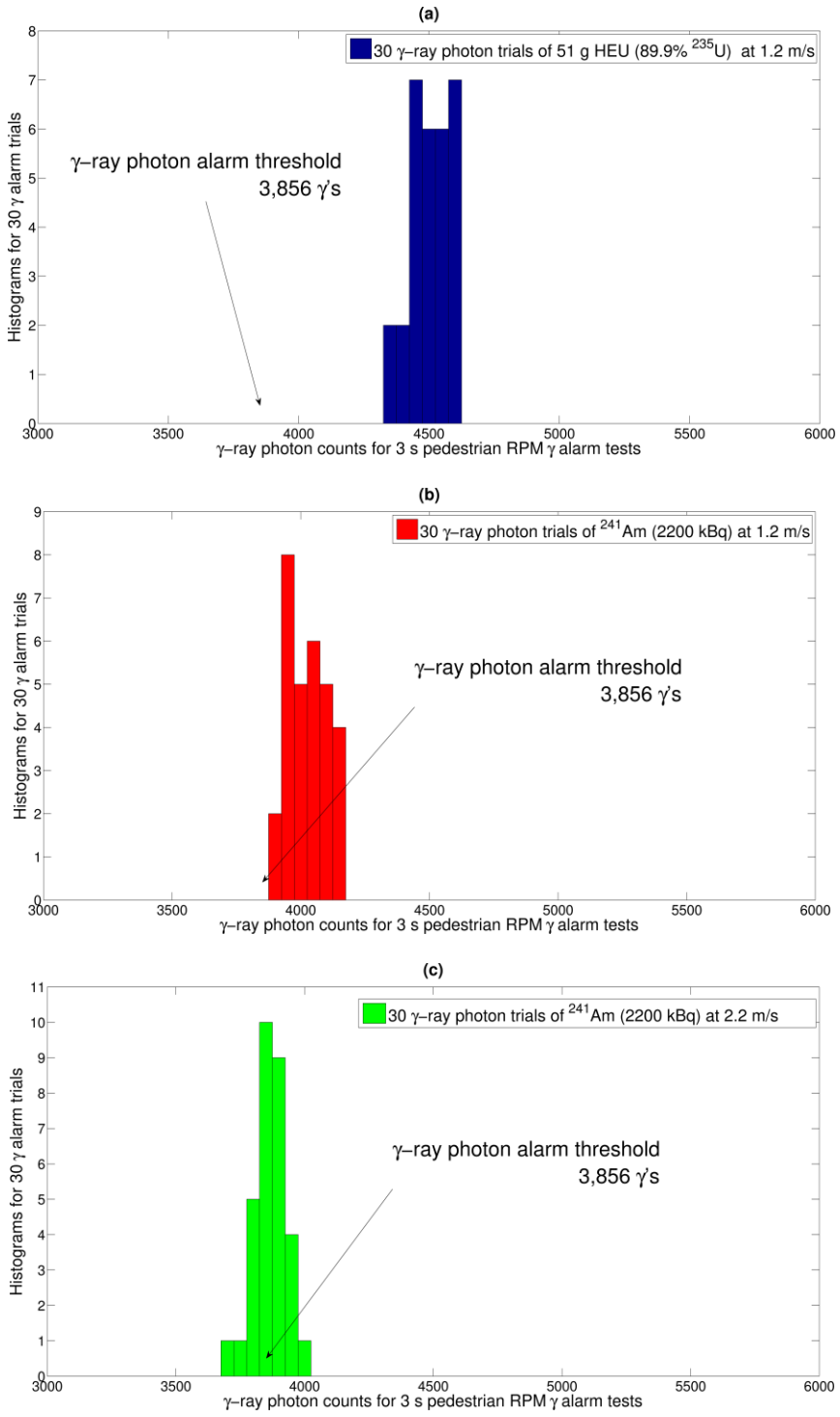

Fig. 4-7. Histograms of measured gamma-ray photons for 30 three second measurements with the pedestrian RPM of: (a) 51 g sample of HEU moving at 1.2 m/s, (b) 2,220 kBq ^{241}Am moving at 1.2 m/s, and (c) 2,220 kBq ^{241}Am moving at 2.2 m/s. These histograms correspond to the data from folders (a) 40, (b) 35, and (c) 34 in Table B-1 in Appendix B. These measurements were part of the pedestrian RPM gamma-ray photon alarm testing during the 2nd SCINTILLA benchmark in February 2014 at the European Commission JRC in Ispra, Italy [39,41]. The 3,856 gamma-ray photons alarm threshold shown is set five standard deviations above the mean background count rate.

4.4.2. Vehicle RPM Gamma-Ray Photon Alarm Results

Identical to the vehicle RPM neutron alarm tests, the vehicle gamma-ray photon alarm tests require that sources travel at 2.2 m/s. The distance between a two pillar vehicle RPM should be 5 m. The same ANSI sources and associated source activities (Table 4-1) used for the pedestrian RPMs should be detected at least 59 out of 60 times with the vehicle RPM [38].

Vehicle RPM gamma-ray photon alarm tests were successfully performed at the 3rd SCINTILLA benchmark at the European Commission JRC in Ispra, Italy, in November 2014 [40,77]. Once again, due to time constraints anywhere between 30 and 43 passages were run per source scenario as opposed to the minimum of 60 trials suggested by ANSI [38].The source activities used (see Table 4-1 and Table 4-5) were as much as 80% lower than prescribed by ANSI [38], making these test conditions quite challenging. Exceptions to this were the two low energy gamma-ray photon sources, ^{57}Co and ^{241}Am, for which a majority of SCINTILLA participants requested that higher activity sources be used in the tests.

The full set of tests and results achieved with our vehicle RPM for these gamma-ray photon alarm tests are presented in Table 4-5. The results were very mixed. For source activities well below the ANSI-suggested activity, like the 107 kBq vs 518 kBq ^{133}Ba, the vehicle RPM had zero successful alarms. For higher energy gamma-ray photons sources and sources with activities closer to the ANSI-recommended values, the vehicle RPM performed satisfactorily.

The sensitivity of both RPMs to detection scenarios beyond ANSI standards could be improved with the use of additional detectors or more efficient detectors in the RPM designs.

Table 4-5. Results of November 2014 3rd SCINTILLA benchmark vehicle RPM gamma-ray photon alarm test results [40,77] for ANSI [38] and beyond ANSI standard test conditions using a variety of gamma-ray photon sources.

Isotope	Activity (kBq)	Speed (m/s)	Source Height (m)	Passages	Alarms
^{241}Am	1,480	2.2	0.8	32	1
^{241}Am	2,220	2.2	0.8	32	5
^{133}Ba	107	2.2	0.8	35	0
^{133}Ba	212	2.2	0.8	33	32
^{133}Ba	107	1.2	0.6	32	0
^{57}Co	262	2.2	0.8	34	0
^{57}Co	333	2.2	0.6	30	0
^{60}Co	181	1.2	0.6	43	38
^{137}Cs	350	2.2	0.8	32	26
^{226}Ra	290	2.2	0.8	30	30
^{226}Ra	290	1.2	0.6	32	31
^{137}Cs	350	2.2	1.7	32	28
^{137}Cs	350	2.2	2.4	30	15
^{60}Co	826	2.2	0.8	32	32
^{60}Co	826	2.2	0.8	32	32
^{137}Cs	3,500	2.2	0.8	32	31
^{137}Cs	3,500	1.2	0.6	32	30
WGPu	6.6 g	2.2	0.8	31	7
WGPu	6.6 g	1.2	0.6	32	25

Chapter 5
Reducing Nuisance Alarms Through On-The-Fly Radionuclide Identification

5.1. Challenges for On-The-Fly Identification

On-the-fly radionuclide identification, as discussed in Chapters 1 and 2, could provide some cost and time savings to CBP by lowering the number of nuisance alarms that would need to undergo a secondary inspections. Ideally, any alarm during primary inspection would report identified radionuclides with some associated certainty. For cases in which clearly only NORM or medical isotopes are present, secondary inspections could be skipped.

In Chapter 2 the differences between organic scintillators, like those used for the RPMs in Chapter 4, and inorganic scintillators and semi-conductor-based gamma-ray photon detectors were discussed. The latter two detector types depend upon the photo-electric effect to form distinct full energy photopeaks in their PHDs. These photopeaks are characteristic of a given isotope's decay scheme, like the many photopeaks of WGPu shown in a PHD taken with a high purity Germanium (HPGe) semi-conductor-based gamma-ray photon detector (see Figure 5-1).

Organic scintillators completely rely upon Compton scattering for detecting incident gamma-ray photons. Therefore a PHD of WGPu acquired with the liquid scintillator-based RPM will show no characteristic photopeaks even for a long measurement time. In a realistic RPM measurement scenario, long measurement times are a luxury that is rarely granted. Measurement times on the order of three seconds are common. Figure 5-2 shows PHDs before and after background subtraction. These PHDs were acquired with the pedestrian RPM during a three second measurement of 6.6 g WGPu moving past the RPM at 1.2 m/s. Background radiation subtraction and the short measurement time result in a jittery PHD with no immediately discernible features that would identify the radiation source as WGPu to the naked eye.

In the following sections a variety of algorithms are discussed that were implemented to draw radionuclide identification information from these noisy short measurement time PHDs.

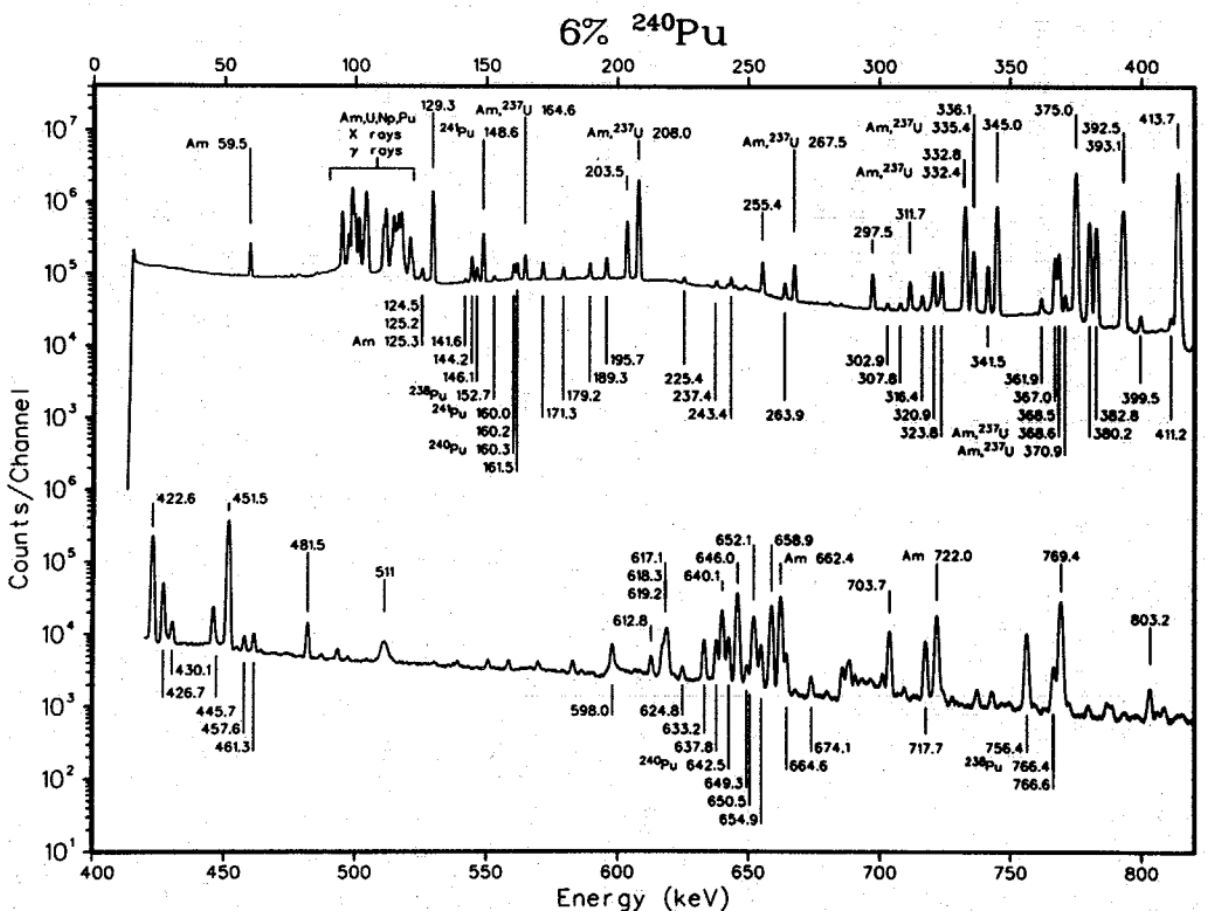

Figure 5-1. Example of a gamma-ray photon PHD of 500 g metal WGPu sample (6% ^{240}Pu) acquired with coaxial HPGe detector [78,79]. Peaks without isotope label stem directly from ^{239}Pu decay, while other peaks stem from other isotopes always found in WGPu, such as ^{241}Am as well as other isotopes of plutonium.

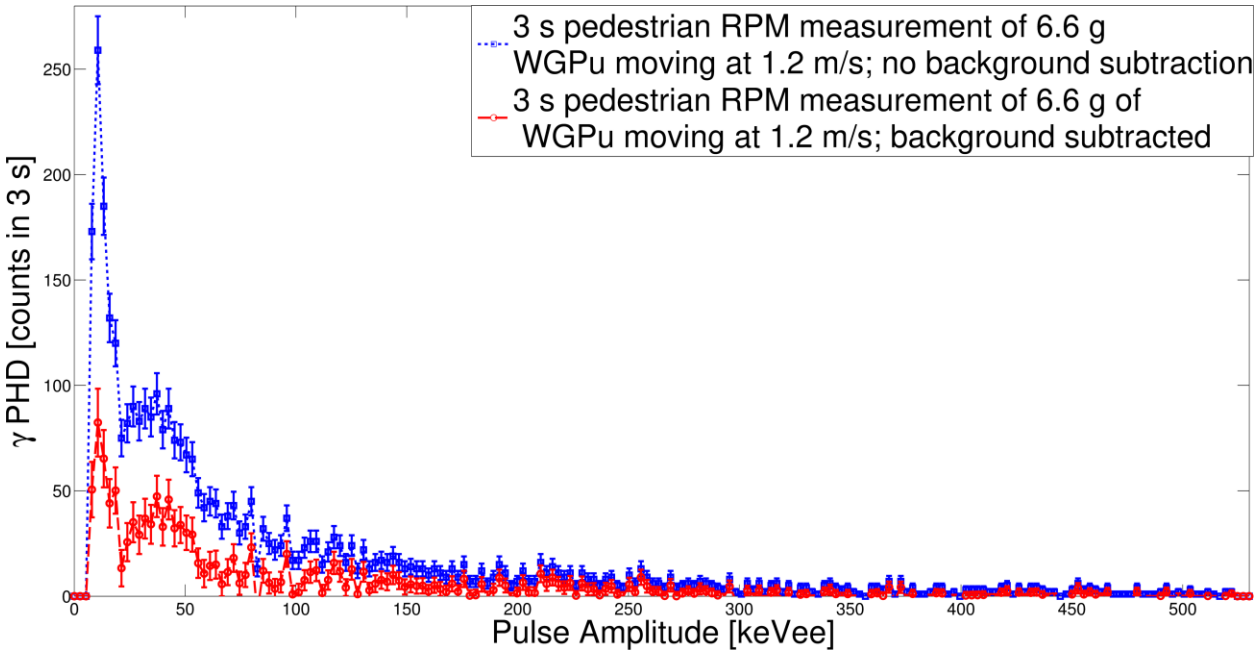

Figure 5-2. Gamma-ray photon PHDs before (blue squares) and after (red circles) background subtraction for three second dynamic measurement of 6.6 g WGPu with pedestrian RPM during 2nd SCINTILLA benchmark at JRC Ispra, Italy, in February 2014 [39,80,81]. Such a background subtracted PHD would provide the raw basis for any subsequent on-the-fly radionuclide identification attempts [39,80].

5.2. Identification Using Least Squares Comparison with Modified PHDs

The first rudimentary radionuclide identification algorithm implemented for the pedestrian RPM utilized a least squares comparison between the short three-second PHDs of the moving sources and the much longer previously acquired library spectra shown in Figure 5-3. As mentioned in Chapter 2.2, the organic scintillators are energy calibrated assuming 80% of the ^{137}Cs Compton edge corresponds to the expected 478 keVee light output. The calibration gives the linear relationship between the pulse height in Volts and light output in keVee. The 2 V dynamic range of the V1720 digitizer used for the pedestrian RPM is insufficient to capture the full PHDs of both low energy gamma-ray photon emitting sources, like ^{241}Am, and high energy gamma-ray photon emitting sources, like ^{40}K. Therefore, as shown in Figure 5-3, one set of detectors was calibrated at a higher gain to capture the PHDs of the lower energy gamma-ray photons, while another set of detectors was calibrated at a lower gain to capture the full PHDs of higher energy gamma-ray photons. Not all isotopes in the library PHDs ended up being used in the dynamic tests. ^{40}K and ^{226}Ra were dropped from the tests due to time constraints.

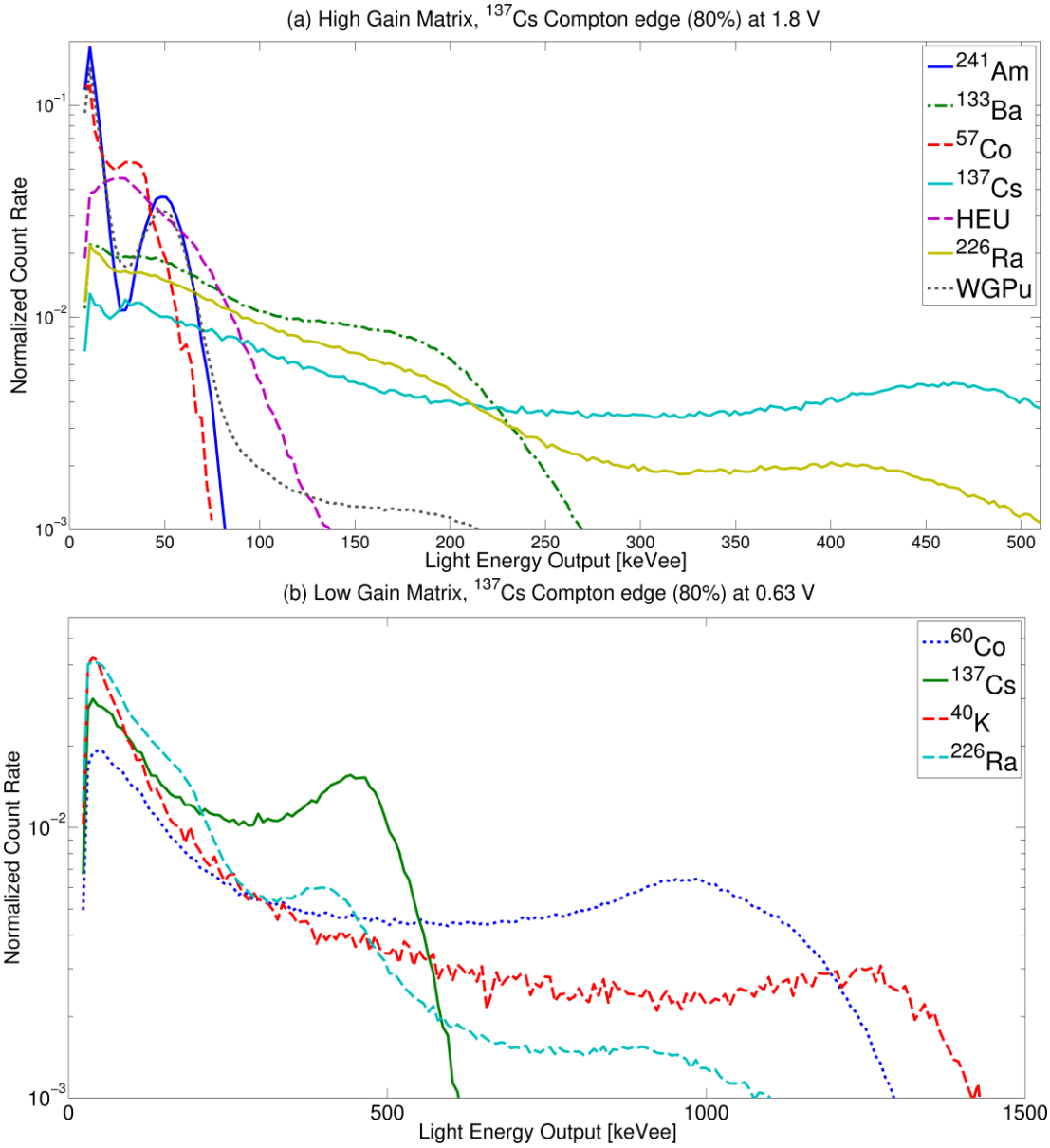

Figure 5-3. High (a) and low (b) gain matrices used as library spectra for on-the-fly radionuclide identification with the pedestrian RPM at the 2nd SCINTILLA benchmark at the JRC Ispra, Italy, in February 2014. Measurement times for all PHDs exceeded 600 s. Of the eight detectors, five used the high gain setting and three used the low gain setting [39,80].

The identification methodology relies on finding the lowest residual value (S_i) when doing a least squares comparison between the dynamic three second measurement PHD and all of the library PHDs using equation (5-1):

$$S_i = \sum_{b=1}^{B}(m_b - l_{ib})^2, \tag{5-1}$$

where B is the number of bins in the PHD, m_b is the preprocessed count rate in the b^{th} bin of the PHD, and l_{ib} is the preprocessed count rate in the b^{th} bin of the i^{th} isotope in the library. Figure 5-4a shows a three second measurement of ^{57}Co using the pedestrian RPM during the 2nd SCINTILLA benchmark. Included in this Figure is the ^{57}Co library PHD that the three second measurement should match, in theory. In practice, the three second measurement is very noisy resulting in large residuals for all PHD comparisons. Therefore a number of modifications are performed on both the three second and library PHDs to improve the identification accuracy.

The background radiation PHD that is subtracted from the three second measurement has excellent statistics due to the much longer measurement time. The three second measurements have poor statistics and only very few counts in most PHD bins. Therefore it is probable that the background corrected three second PHDs will showcase jitter and exhibit many bins with negative counts. These negative count bins substantially add to the residual value, especially for low energy gamma-ray photon PHDs for which only a few bins contain a substantial number of counts. Therefore, the first step is to filter out some of the noise by zeroing out all PHD bins with negative counts or counts below some small user defined threshold. Figure 5-4b shows the much cleaner ^{57}Co PHD after this noise suppression has been applied.

To increase the statistics of individual PHD bins, bin coarsening was applied, as shown for the same ^{57}Co PHD in Figure 5-4c. Too much bin coarsening, however, will eliminate characteristic features in the PHDs. A bin coarsening factor of two was found to give satisfactory results [39,80].

Finally one has to also decide which lowest residual value to use: the overall lowest residual, or the lowest residual from the low or the high gain matrix? The algorithm uses three criteria to make a selection. A high energy gamma-ray photon will create more counts in the low gain detector PHDs than in high gain detector PHDs. The ratio of counts in the low gain versus the high gain detectors is used as the first decision-making criteria. If this ratio exceeds 0.75, it is assumed that a high energy gamma-ray photon source was being measured, so the lowest residual value of the low gain detector set is chosen. For very low count rate scenarios, however, the ratio might be meaningless. When there are fewer than 50 counts in the low gain detectors, the identification result from the low gain detectors is thrown out. Finally, if neither of the previous two criteria leads to a conclusive answer, then simply the lowest residual value is used

to pick the radionuclide [39,80]. Originally the method also included the use of user-defined weighting masks, but these had mixed effects on the identification results and were deemed to be too arbitrary [80].

The radionuclide identification results for samples measured with the pedestrian RPM at the 2nd SCINTILLA benchmark at the JRC Ispra, Italy, in February 2014 are listed in Table 5-1. The identification results are listed for both high- and low-gain detectors as the PHDs are modified step by step. The final identification results were excellent for ^{133}Ba and HEU, but only middling for ^{241}Am, ^{57}Co, ^{60}Co, and ^{137}Cs. The WGPu was misidentified for all thirty trials. Figure 5-5 shows that the library WGPu PHD does not match the PHDs from the dynamic WGPu measurements. Possible explanations could include improper gain settings when measuring the WGPu library PHD. Overall, the modified PHD least squares method did not produce high quality and fidelity identification results, and relied too heavily on user choices, like bin coarsening. These challenges inspired the subsequent radionuclide identification algorithm developments.

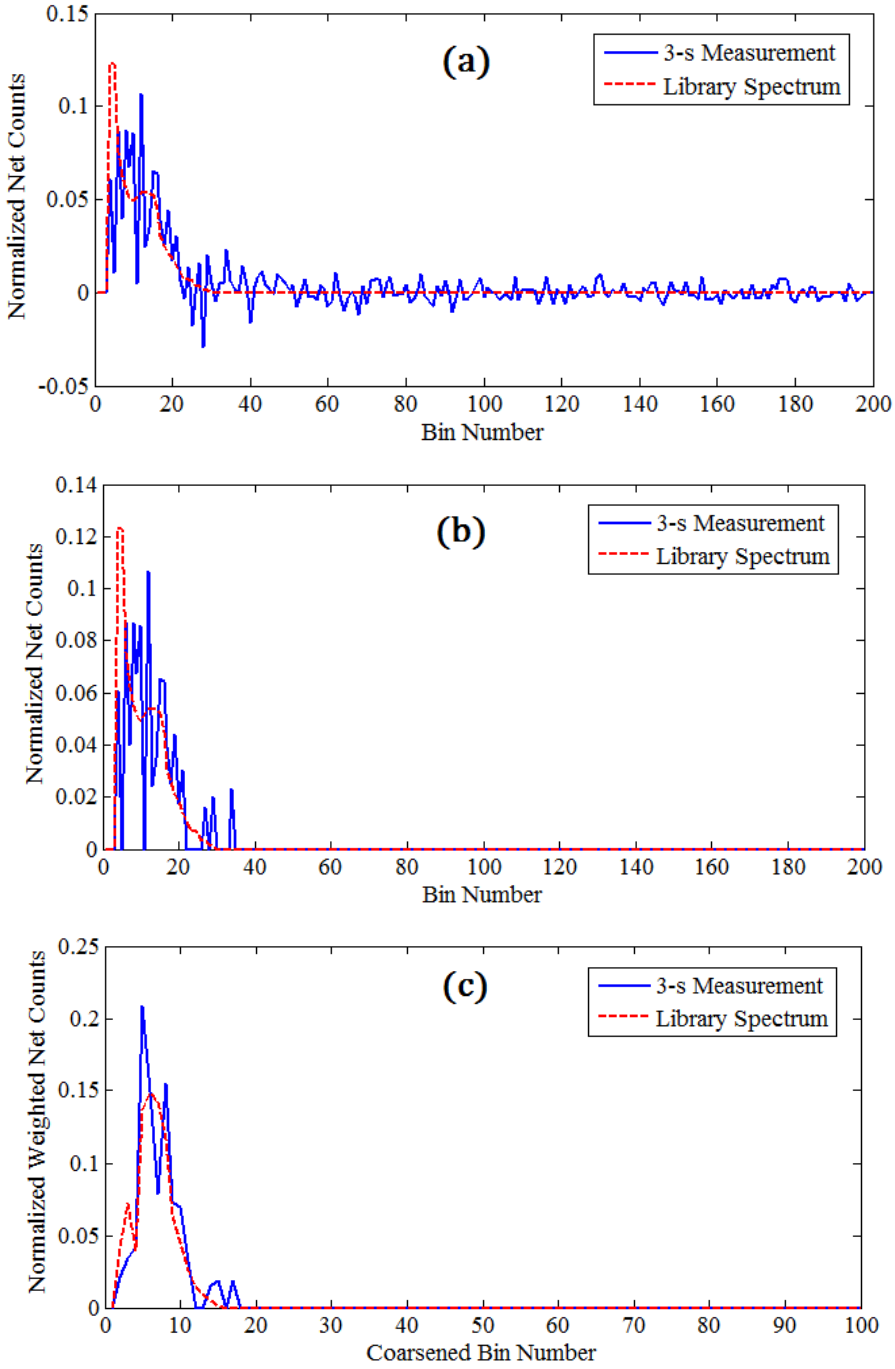

Figure 5-4. PHD modification steps for a three second ^{57}Co measurement with pedestrian RPM at February 2014 SCINTILLA benchmark at JRC Ispra, Italy. All PHDs are subdivided into 200 bins. See Figure 5-3a for energy scale. (a) Background corrected three second PHD (blue) versus library spectrum of ^{57}Co (red) from Figure 5-3a; (b) PHDs after noise suppression has been applied to zero out negative and low count rate bins; (c) PHDs after bin coarsening by a factor of two [39,80].

Table 5-1. Correct radionuclide identification using the modified least squares method out of 30 trials for different isotopes measured with the pedestrian RPM at the 2nd SCINTILLA benchmark at the JRC Ispra, Italy, in February 2014 [39,80]. Identification results are shown for both high- and low-gain detector sets, and for the different PHD modification steps outlined in Figure 5-4.

Correct IDs (High-gain, Low-gain)	^{60}Co		WGPu		^{133}Ba		^{57}Co		^{241}Am		^{137}Cs		HEU	
Raw Spectrum	0	23	0	0	30	0	9	0	19	0	23	27	30	0
Noise Suppression	0	19	0	0	30	0	9	0	18	0	10	23	30	0
Bin Coarsening	0	19	0	0	30	0	12	0	20	0	11	22	30	0
Final HG/LG Selection	14		0		30		12		20		11		30	

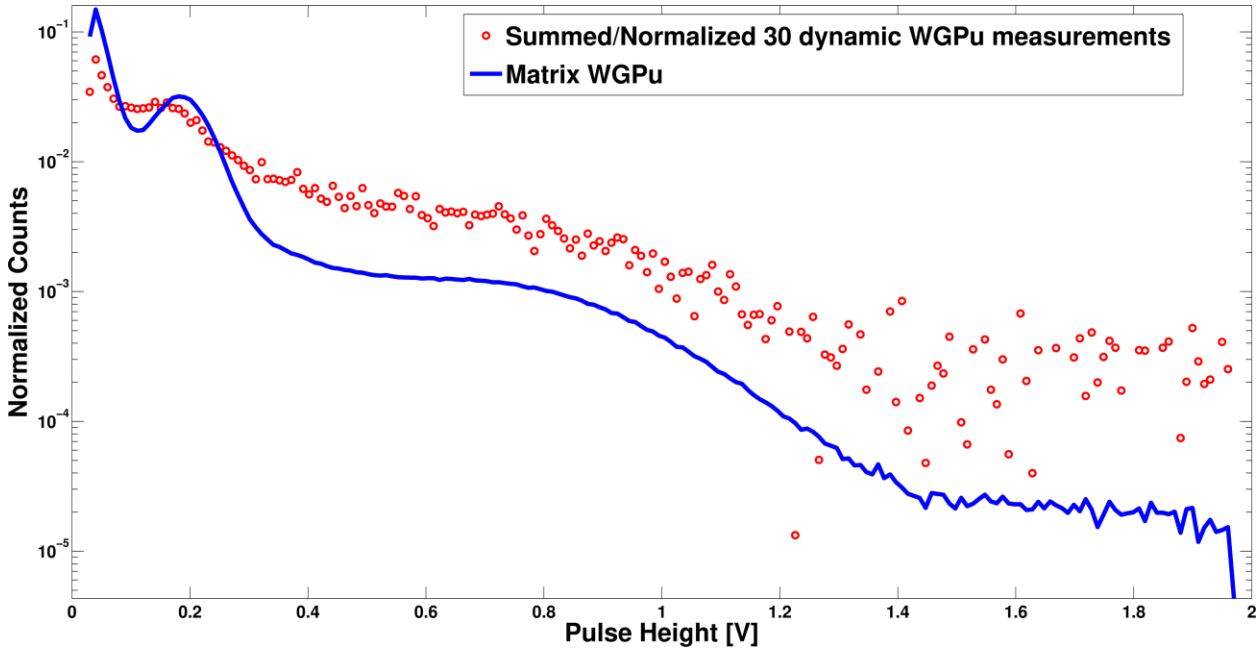

Figure 5-5. Average dynamically measured PHD for WGPu and WGPu library PHD for pedestrian RPM at 2nd SCINTILLA benchmark at JRC Ispra, Italy, in February 2014. These two PHDs do not match well, explaining why WGPu was never identified correctly [39].

5.3. Identification Using Least Squares Comparison with Cumulative Distribution Functions

The least squares method with modified PHDs described in 5.2 did not consistently produce satisfactory radionuclide identification results for the set of radionuclides measured with

the pedestrian RPM. Its multi-step process and reliance on user-defined parameters made the method inelegant and convoluted. A simpler, more robust, and more successful radionuclide identification algorithm had to be developed. All background corrected measured PHDs were saved, so other identification algorithms could easily be tested on the dataset.

The goal of all developed identification algorithms was to find a bridge between the jittery dynamically measured PHDs with low counting statistics, and the smooth and well-defined library PHDs of radionuclides used for identification. In the previous method this was attempted through de-emphasizing unimportant PHD regions through noise suppression, and emphasizing distinctive PHD features through bin coarsening and weighting functions.

The next proposed radionuclide identification method uses least squares comparisons of modified CDFs of both the library PHDs and the dynamically measured PHDs. It is hypothesized that CDFs would smooth out the statistical jitter of the short measurement time dynamically measured PHDs, while also preserving and emphasizing any distinctive PHD features that might not be obvious when viewing the noisy unmodified PHDs.

The CDF, $x(n)$, of any distribution $F_X\ (x)$ represents the probability that X takes a value less than x, i.e., $P(X \leq x)$. The PHD is integrated bin-by-bin, thus expressing what fraction of the total PHD exists to the left of each bin. Our subsequent analysis uses $y(n) = (1 - x(n))$. The CDFs thus are formed by integrating the PHDs from right to left and normalizing to unity. The integration from high to low energy was chosen to minimize the effects of variable noise found at low energies right above the threshold [81]. The algorithm still utilizes equation (5-1) to compute the residual values when comparing dynamically measured $y(n)$ to the library $y(n)$ spectra. The radionuclide is identified by finding the library $y(n)$ that produces the smallest residual when compared with the dynamically measured $y(n)$. High- and low-gain $y(n)$ matrices are shown in Figures 5-6a and 5-6b.

Figures 5-7a and 5-7b show examples of the three second dynamic measurements of radionuclides with the pedestrian RPM at the 2nd SCINTILLA benchmark, and how their $y(n)$ spectra match well with the library $y(n)$ for a variety of radionuclides in the high- and low-gain matrices. While the modified PHD method required several steps and user chosen parameters to smoothen the jittery short measurement time PHDs, the CDF method only uses one operation to

transform a noisy and messy PHD into a form that is easily comparable and relatable to the smoother library $y(n)$.

Table 5-2 compares the success rate of the modified PHD and CDF radionuclide identification methods for the pedestrian RPM data from the 2nd SCINTILLA benchmark at JRC Ispra, Italy, from February 2014. With the exception of ^{241}Am, all radionuclides were identified correctly at a significantly higher success rate, even at the higher source transit speed of 2.2 m/s. Nevertheless, the average correct radionuclide identification rate of 90%, while good for an initial attempt, would need to be further improved for commercial viability.

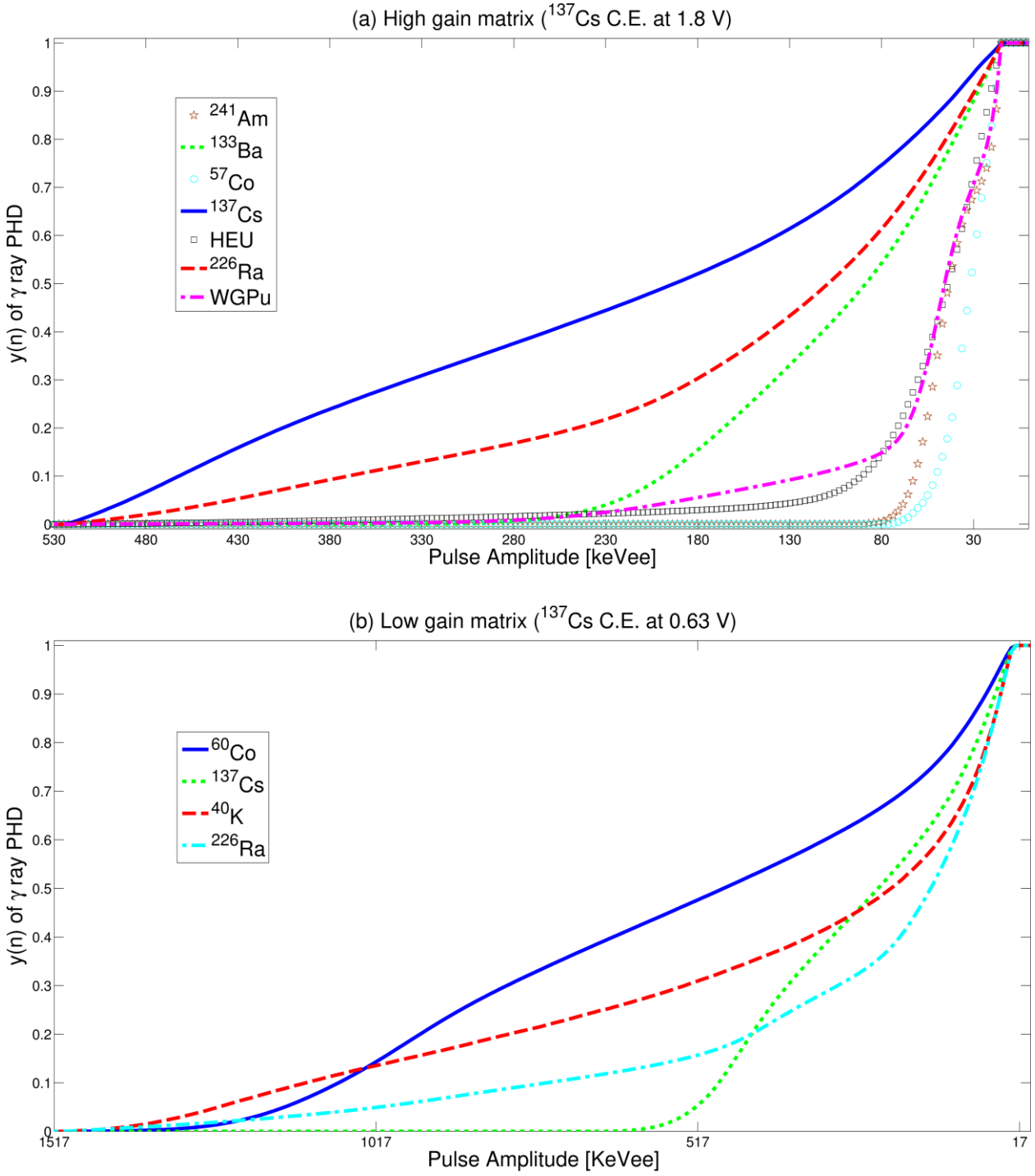

Figure 5-6. (a) High-gain modified CDF library matrix for RPM radionuclide identification, (b) low-gain modified CDF library matrix for radionuclide identification [39,66].

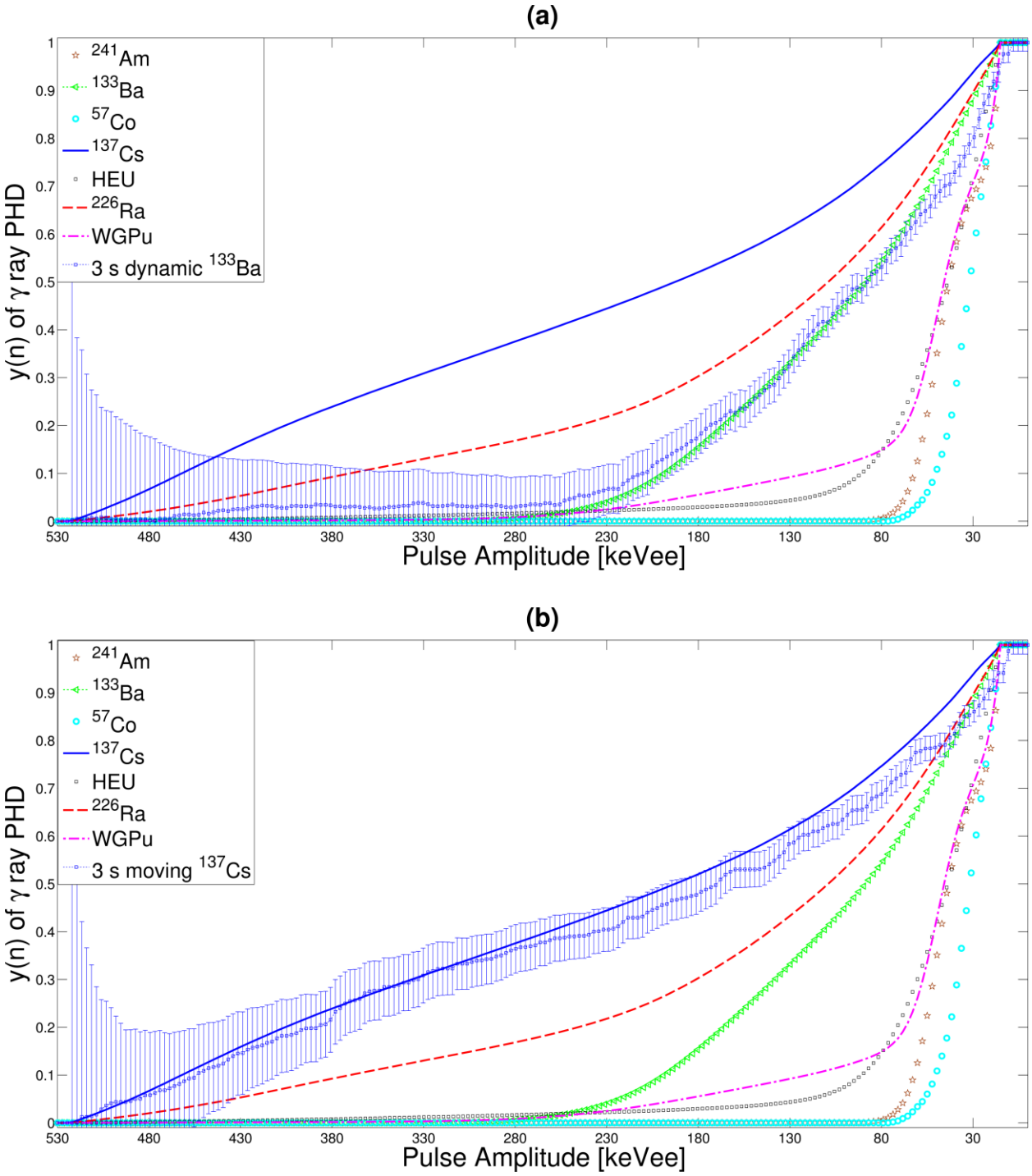

Figure 5-7. High-gain modified CDF library matrix for RPM radionuclide identification with $y(n)$ of dynamic measurements of (a) ^{133}Ba and (b) ^{137}Cs with pedestrian RPM at 2nd SCINTILLA benchmark at JRC Ispra, Italy, in February 2014 [39,66,81].

Table 5-2. Comparison of correct radionuclide identifications out of 30 trials using the modified least squares method versus the CDF method for different isotopes measured with the pedestrian RPM at the 2nd SCINTILLA benchmark at the JRC Ispra, Italy, in February 2014 [39,80]. A slightly higher pulse height threshold of 0.06 V vs 0.03 V was used for the ^{57}Co results.

Source	Speed [m/s]	Modified PHD method Correct ID (#/30)	CDF method Correct ID (#/30)
^{137}Cs	1.2	11	27
^{137}Cs	2.2	3	25
HEU	1.2	30	30
HEU	2.2	30	25
^{60}Co	1.2	14	26
^{60}Co	2.2	7	20
^{133}Ba	1.2	30	30
^{133}Ba	2.2	21	30
^{57}Co	1.2	12	25
^{241}Am	1.2	20	13

5.4. Adding Medical Isotopes to the Mix

As mentioned in Chapter 1, medical isotopes, especially ^{99m}Tc, have become a common source of RPM nuisance alarms [30]. Therefore, it was highly desirable to add these isotopes to the RPM radionuclide identification library.

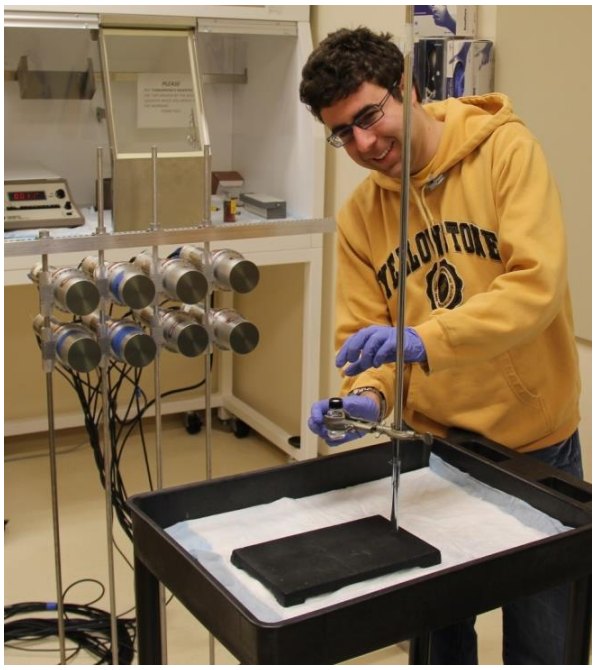

Figure 5-8. Measuring medical isotopes with the pedestrian RPM at the University of Michigan's C.S. Mott Children's Hospital in December 2013.

In June 2016, medical isotope gamma-ray photon emissions were measured with four different detectors, including a 7.6 cm diameter and a 12.7 cm diameter cylindrical volume EJ309 organic liquid scintillation detector, a 5.1 cm diameter and 5.1 cm height cylindrical volume stilbene crystal from Inrad Optics, as well as an experimental 5.1 cm diameter and 5.1 cm height cylindrical volume plastic scintillator named BB3 from Radiation Monitoring Devices (see Figure 5-9 for setup).

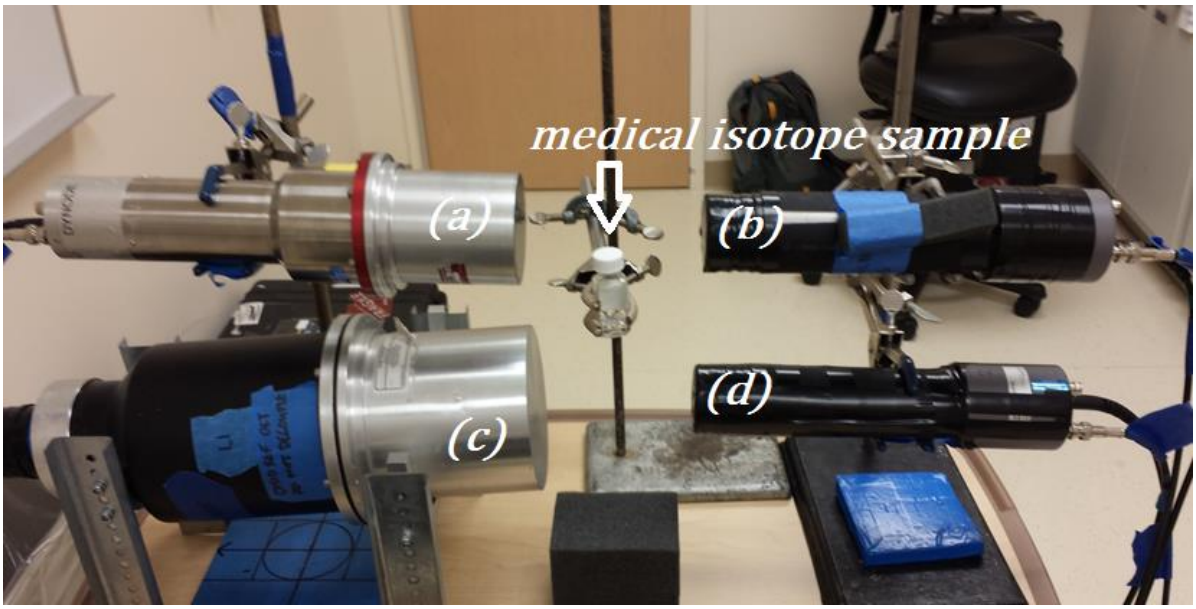

Figure 5-9. June 2016 setup for measuring medical isotopes at University of Michigan's C.S. Mott Children's Hospital using: (a) a 7.6 cm diameter cylindrical volume EJ309 organic liquid scintillation detector, (b) a 5.1 cm diameter and 5.1 cm height cylindrical volume stilbene crystal from Inrad Optics, a 12.7 cm diameter cylindrical volume EJ309 organic liquid scintillation detector (d) an experimental 5.1 cm diameter and 5.1 cm height cylindrical volume plastic scintillator name BB3 from Radiation Monitoring Devices [81].

The medical isotopes came in solution form packaged in glass vials. A total of seven medical isotopes were measured, including ^{18}F, ^{67}Ga, ^{123}I, ^{131}I, ^{111}In, ^{99m}Tc, and ^{201}Tl. At time of calibration each source had an activity of $7 - 8\ \mu Ci$ with a 20% uncertainty. The sources are pictured in Figure 5-10 and more source information is listed in Table 5-3. ^{18}F has a relatively short half-life of 1.83 hours, so even though it was included in these measurements, it is considered to be a very unlikely source of nuisance alarms at border crossing as its activity decreases so rapidly with time [30].

Figure 5-10. $7-8\ \mu Ci$ medical isotope samples measured at the University of Michigan's C.S. Mott Children's Hospital in June 2016. From left to right: ^{111}In, ^{18}F, ^{67}Ga, ^{123}I, ^{201}Tl, ^{99m}Tc, and ^{201}Tl. Labeled activities are desired activities, which at times differed by $1\ \mu Ci$ from the actual activities listed on separate calibration source sheets provided by the hospital.

Table 5-3. List of medical isotopes measured at University of Michigan's C.S. Mott Children's Hospital in June 2016 and their respective radioactive half-lives in hours, and their activities at time of sample calibration and at time we measured them [81].

Isotope	$T_{1/2}$ [h]	Activity at noon 6/2/16 [mCi] $\pm 20\%$	Activity at time of measurement [mCi] $\pm 20\%$
^{99m}Tc	6.0	0.008	0.007
^{123}I	13.3	0.007	0.007
^{201}Tl	72.9	0.008	0.008
^{131}I	192.5	0.008	0.008
^{111}In	67.3	0.007	0.007
^{18}F	1.8	0.007	0.001
^{67}Ga	78.3	0.007	0.007

Each of the seven medical sources was measured for thirty minutes. Four background measurements were taken interspersed throughout the day of the measurements. The background corrected CDFs of the PHDs measured with the 7.6 cm diameter cylindrical volume EJ309 organic liquid scintillation detector were added to the high gain identification matrix for the pedestrian RPM (see Figure 5-6a). This updated identification matrix for low energy gamma-ray photon sources is shown in Figure 5-11. The figure also includes a modified CDF ($y(n)$) of a short measurement (1000 pulses) of ^{131}I.

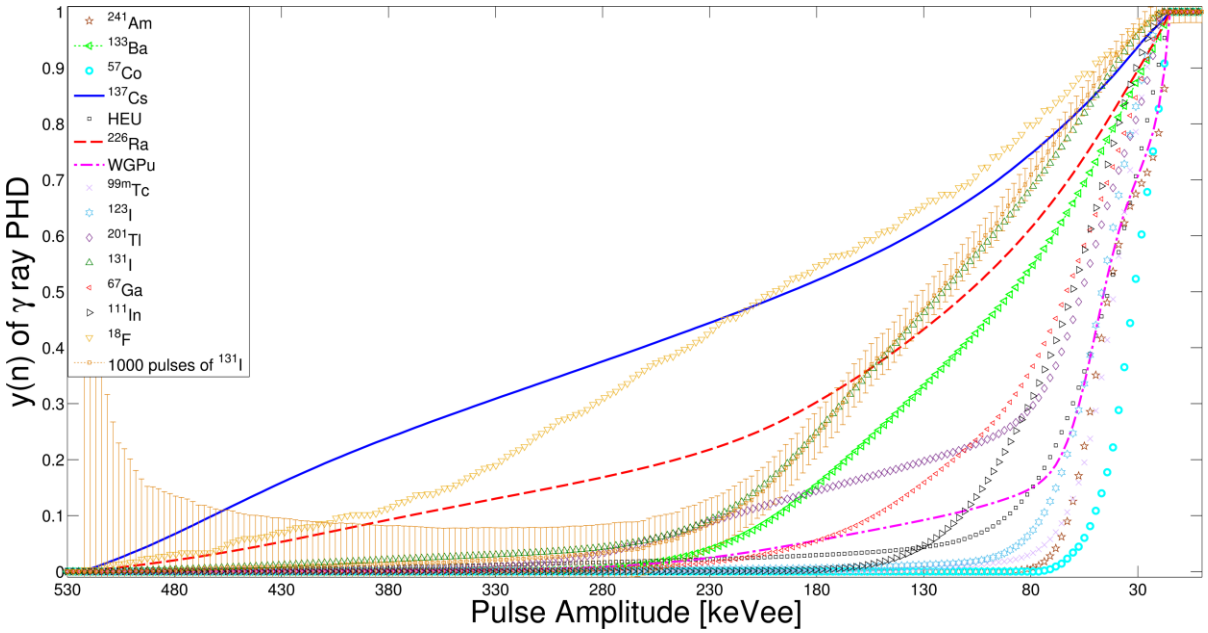

Figure 5-11. High-gain modified CDF library matrix, including medical isotopes, for RPM radionuclide identification with $y(n)$ of measurement of ^{131}I with pedestrian RPM detector at University of Michigan's C.S. Mott Children's Hospital in June 2016 [81].

From Figure 5-11 it becomes clear that the addition of many low gamma-ray photon energy emitting medical radionuclides increases the difficulty of correctly identifying any of the low energy sources. The performance of the least squares comparison identification method with CDFs, introduced in Section 5.4, degrades with the addition of more and more radionuclides to the library, so a more robust identification algorithm is needed.

5.5. Identification Using Power Spectral Density and Spectral Angular Mapping

All of the previously described radionuclide identification algorithms worked well to a degree, but none of them were able to correctly identify nuisance and threat alarms 100% of the time. It would be entirely unacceptable for CBP to misidentify an HEU source as a benign medical source, as it would also be utterly embarrassing for CBP to cause a security panic if a medical isotope was misidentified as WGPu. While the modified CDFs do well at smoothing out the noisiness of the short measurement time PHDs, the least squares comparison does not constitute a robust enough identification metric. Two modified CDFs might look very similar to the naked eye overall. However, a small shift or offset, or an outlier data point in the short measurement time modified CDF could all easily lead to a large residual value computed in the least squares comparison, and thus lead to a probable misidentification of the radionuclide.

In other words, the least squares method compares the exact match of the two modified CDFs point by point, but says nothing about similarities in overall shapes and trends between two modified CDFs. The discrete Fourier transform (DFT) (see Equation 5-2) of $y(n)$ describes how rapidly $y(n)$ changes over its energy domain. A fast Fourier transform (FFT) speeds up the computation of the DFT which converts a signal in time into the frequency domain [82]. However, Fourier analysis can be applied to many other areas, such as image processing, so it could be a power tool in analyzing and comparing measured modified CDFs.

$$DFT(k) = \sum_{n=1}^{N} y(n) \exp\left(-i * 2 * pi * (k-1) * \frac{n-1}{N}\right),\ 1 <= k <= N, \tag{5-2}$$

where *DFT(k)* is the amount of frequency in the signal, *y(n)* is the modified CDF, *n* is the sample energy domain, *N* is the number of samples, and *k* is the sample in the frequency domain.

For a continuous signal, the power spectral density (Equation 5-3) computes how "power" is distributed over frequency of the CDF by computing the square of the DFT:

$$PSD(k) = |DFT(k)|^2. \tag{5-3}$$

In electrical engineering applications this "power" refers to actual physical power, for instance in a circuit, but for more abstract signals, like CDFs from RPMs, "power" has no physical meaning, so one can just think of power spectral density as the square value of the signal. The power spectral density provides a metric now to describe how the CDF behaves over its entire domain. So even though two CDFs might not look identical at first glance, they might behave very similarly thus suggesting they may have both arisen from the same radiation source. Examples of modified CDF, FFT, and power spectral density are shown for a dynamic ^{137}Cs measurement from SCINTILLA pedestrian RPM data in Figure 5-12.

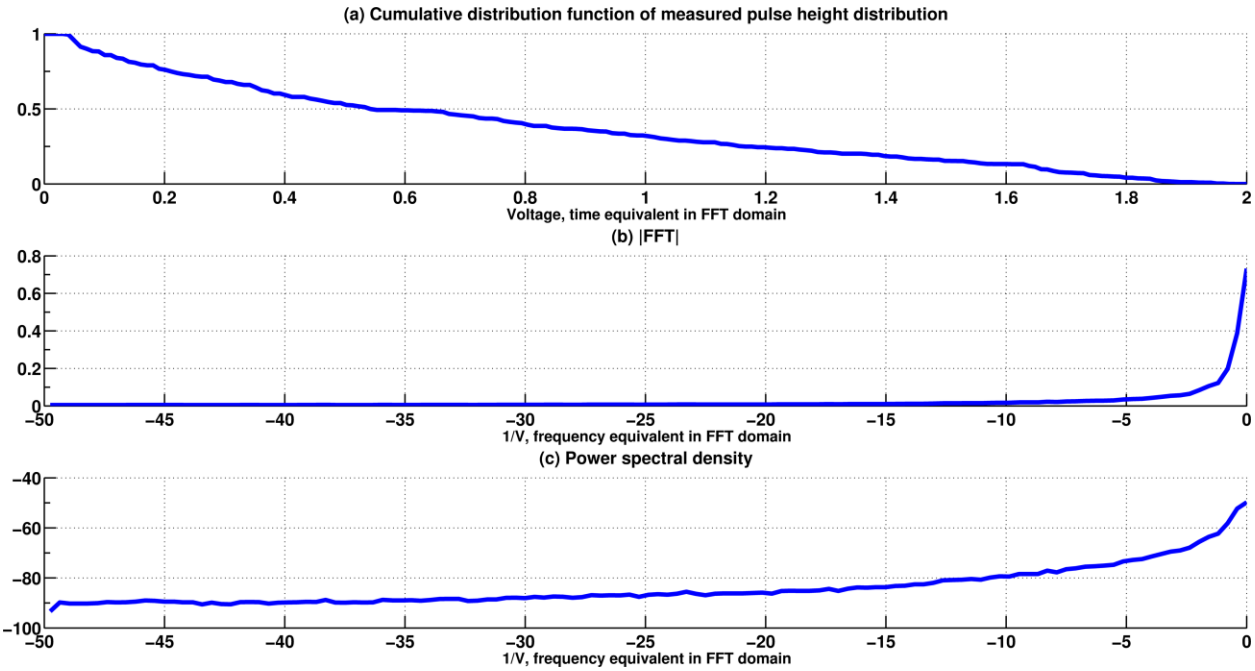

Figure 5-12. Examples of (a) modified CDF ($y(n)$), (b) FFT, and (c) power spectral density for signal from a three second measurement of ^{137}Cs with the pedestrian RPM at the SCINTILLA benchmark at JRC Ispra, Italy, in February 2014.

Spectral angle mapping (SAM) offers a new way of comparing measured and reference spectra for the purpose of identifying radionuclides. SAM computes the spectral angle (in radians, see Equation 5-4) between the power spectral density of the measured spectrum and a matrix of reference power spectral density spectra for the library of radionuclides. A smaller SAM value indicates better agreement between measured and reference spectra:

$$\alpha_i = \cos^{-1}\left[\frac{(PSD(k)\cdot PSD_{matrix}(:,i))}{\|PSD(k)\|\|PSD_{matrix}(:,i)\|}\right], \quad [83] \qquad (5\text{-}4)$$

where we compute the spectral angle α between the power spectral density of a measured spectra and the library power spectral density spectra for any isotope i.

SAM was developed by J. W. Boardman while working for the Center for the Study of Earth from Space (CSES), Cooperative Institute for Research in Environmental Sciences (CIRES), University of Colorado, Boulder USA in the early 1990s. SAM was developed to analyze spectral similarities between measured and reference spectra for imaging spectrometry for creating maps of the distribution of and composition of materials on the Earth's surface [83,84]. The SAM method has since been widely adopted for a variety of image analysis needs [85–88], especially in environmental, earth, and space sciences, but also in limited ways in nuclear security applications [89,90]. SAM has not yet been used for

radionuclide identification. Figure 5-13 shows how SAM could be used to compare a reference spectrum to a measurement spectrum. A measurement spectrum would be compared to all library reference spectra representing the different radionuclides. The match with the smallest SAM value would be picked as the match. The absolute value of this SAM value could then also be used to quantify the confidence of the match being correct. The SAM analysis could be applied directly to the CDFs, as shown in Figure 5-13, or it could be applied to the power spectral densities of the measurement and reference CDFs.

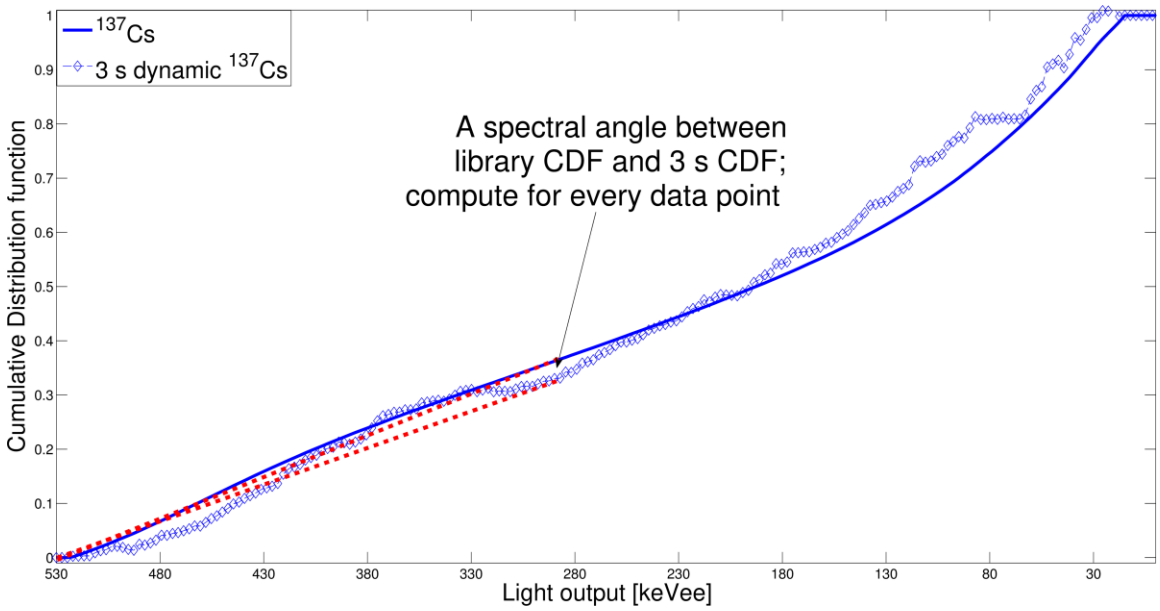

Figure 5-13. Example of SAM angle being computed between a RPM measured CDF and reference CDF of ^{137}Cs. This process would be repeated for all data points in the measured spectrum. SAM values would then be computed for comparisons with all reference CDFs representing all library radionuclides. The overall smallest SAM value gives the likeliest radionuclide to cause the measured CDF.

For the following radionuclide identification analysis all isotopes shown in Figure 5-11, with the exception of ^{18}F, are used. As previously mentioned, ^{18}F is not considered a threat to cause RPM nuisance alarms due to its short half-life [28,30]. That leaves us with two SNM sources, six medical isotopes, and five industrial gamma-ray photon sources. The reference matrix consists of the power spectral densities of the long measurement time CDFs of these sources acquired at the 2nd SCINTILLA benchmark and the University of Michigan's C.S. Mott Children's Hospital with the 7.6 cm diameter cylindrical volume EJ309 organic liquid scintillation detectors.

These reference spectra are compared with the pedestrian RPM data for the 30 trials per gamma-ray photon source at 1.2 m/s source transit speed from the 2nd SCINTILLA benchmark. The corresponding folder numbers from Table B-1 from Appendix B give the full setup information, and are as follows: ^{241}Am (35), ^{133}Ba (28), ^{57}Co (32), ^{60}Co (18), ^{137}Cs (37), HEU (40), and WGPu (22). The

pedestrian RPM, on average, measured between 4,000 and 5,000 gamma-ray photons for the three second measurement time and 1.2 m/s source transit speed case at the 2nd SCINTILLA benchmark. The background contribution to this number, however, is quite high, as the alarm level was set at 3,856 gamma-ray photons. Therefore the net number of detected source gamma-ray photons per three second measurement varied between a few hundred and about a thousand. For the medical isotope data, the number of pulses processed for each of the thirty trials was selected as to result in a similar number of net detected source photons after background subtraction.

For the previously described measurement conditions, the SAM method now gives 100% correct identification for all thirty trials of all thirteen radionuclides. An example of the SAM identification output is shown in Table B-2 in Appendix B for thirty datasets of 1,000 net detected source pulses for ^{99m}Tc. The ^{99m}Tc is identified correctly for every single dataset. It is of great importance to know at what point this identification method starts breaking down. In other words, what is the minimum number of detected source gamma-ray photons needed for a consistently reliable source identification via this algorithm? For ^{99m}Tc it was found that starting at around 400 net detected source pulses, the first misidentifications started occurring. Table B-3 shows that for this scenario two out of thirty ^{99m}Tc datasets were misidentified as ^{123}I, which has a very similar CDF to ^{99m}Tc (see Figure 5-11).

Tables 5-4 and 5-5 list the average α SAM values computed for the correct radionuclide for two different dataset scenarios. Table 5-4 uses the less challenging dataset containing the aforementioned 1.2 m/s source transit speed SCINTILLA datasets and the medical radionuclide datasets containing 1,000 net accepted pulses. Table 5-5 uses a more challenging dataset containing the 2.2 m/s source transit speed SCINTILLA datasets and medical radionuclide datasets containing only 400 net accepted pulses. Two trends can be seen in these tables. First, lower energy sources (^{241}Am, ^{57}Co) exhibit the highest α SAM values, indicating that these sources are the most difficult sources to correctly identify. Second, α SAM values increase in Table 5-5 relative to Table 5-4. This increase confirms that using less data makes correct radionuclide identification more challenging.

Table 5-4. Average and standard deviations of the SAM α values computed for the correct isotope for thirty datasets for each of the 13 tested radionuclides. The SNM and industrial radionuclide datasets come from the datasets from Table B-1 listed previously in this section. The medical datasets consist of 1,000 net detected pulses from the respective medical sources. Examples of full datasets showing SAM α values for all 30 datasets for one isotope for all possible radionuclide identification options are given in Tables B-2 and B-3 in Appendix B [81].

	^{241}Am	^{133}Ba	^{57}Co	^{137}Cs	HEU	WGPu	^{67}Ga	^{123}I	^{131}I	^{111}In	^{99m}Tc	^{201}Tl
α_{avg}	0.0061	0.0040	0.0065	0.0049	0.0047	0.0031	0.0018	0.0030	0.0016	0.0017	0.0020	0.0019
α_{std}	9.8E-04	5.2E-04	9.7E-04	5.3E-04	6.8E-04	3.9E-04	2.0E-4	3.3E-04	9.4E-04	2.0E-04	2.7E-04	1.9E-04

Table 5-5. Average and standard deviations of the SAM α values computed for the correct isotope for thirty datasets for each of the 12 tested radionuclides. The SNM and industrial radionuclide datasets come from the following datasets from Table B-1 in Appendix B: folders 17, 21, 27,31, 34, 36. All of these tests are the same as those used for Table 5-4 except that the source transit speed is increased from 1.2 m/s to 2.2 m/s . The medical datasets consist of 400 net detected pulses from the respective medical sources, which is at the limit of detection for the pedestrian RPM for the background conditions and associated gamma alarm threshold used at the JRC Ispra [81].

	^{241}Am	^{133}Ba	^{57}Co	^{137}Cs	HEU	WGPu	^{67}Ga	^{123}I	^{131}I	^{111}In	^{99m}Tc	^{201}Tl
α_{avg}	0.0072	0.0051	0.0076	0.0060	0.0062	0.0043	0.0034	0.0047	0.0030	0.0017	0.0037	0.0036
α_{std}	8.2E-04	6.9E-04	1.1E-03	5.0E-04	6.6E-04	5.6E-04	3.7E-4	4.9E-04	2.5E-04	2.0E-04	4.7E-04	3.7E-04

One must also take into account that even a nonsensical input will result in an α SAM value. Three such inputs, that should not result in a positive identification of any of the reference spectra, are shown in Figure 5-14. The α SAM values resulting from these inputs are listed in Table 5-6.

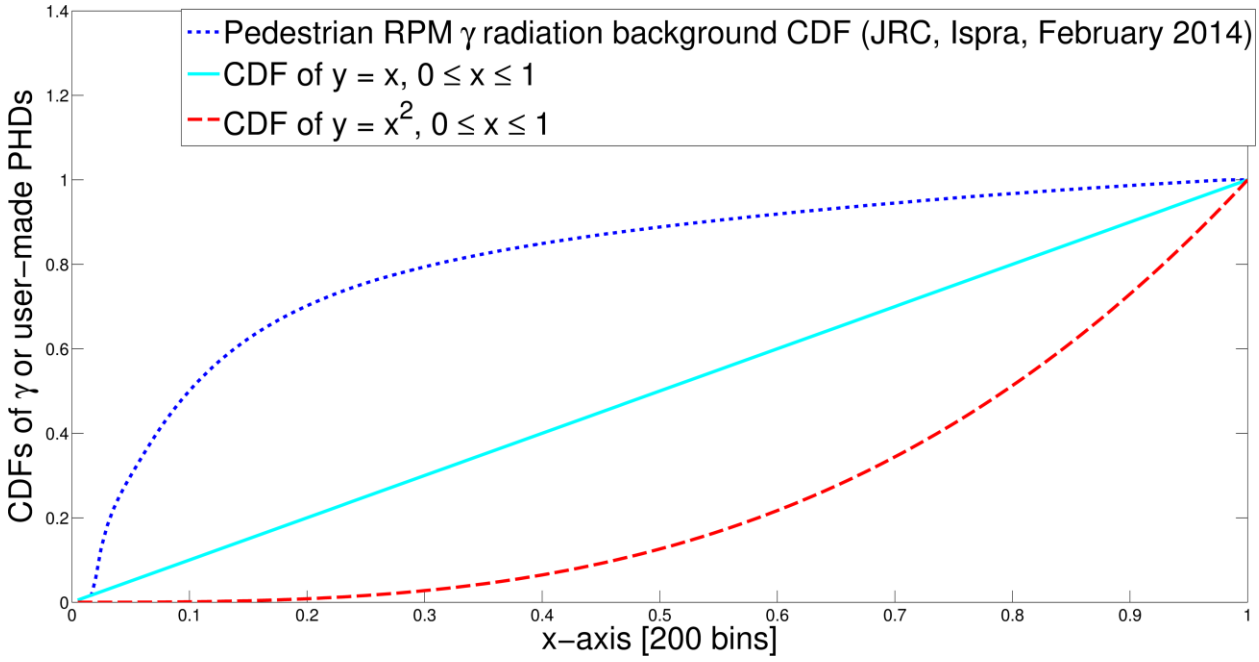

Figure 5-14. Non-source inputs for testing the radionuclide identification algorithms. Test inputs include the CDFs of a gamma ray PHD background measurement, a linear function through the origin, and a square function through the origin. The α SAM values resulting from these inputs are listed in Table 5-4 [81].

Table 5-6. SAM α-values computed for the test cases shown in Figure 5-14. As none of these inputs should match any of the reference spectra, the α SAM values should be larger than, for example, the average α SAM value of 0.003 ± 0.000 for positive identification of WGPu shown in the right most column [81].

Radionuclide	SAM $\alpha_{CDF_{BG}}$	SAM $\alpha_{CDF_{y=x}}$	SAM $\alpha_{CDF_{y=x^2}}$	SAM $\alpha_{CDF_{WGPu_{avg}\pm WGPu_{stdev}}}$
^{241}Am	0.022	0.017	0.013	0.008±0.001
^{133}Ba	0.016	0.010	0.004	0.006±0.000
^{57}Co	0.020	0.014	0.009	0.005±0.001
^{137}Cs	0.012	0.004	0.004	0.009±0.001
HEU	0.020	0.014	0.008	0.005±0.001
^{226}Ra	0.014	0.007	0.003	0.007±0.001
WGPu	0.019	0.013	0.007	0.003±0.000
^{67}Ga	0.020	0.014	0.008	0.008±0.001
^{123}I	0.026	0.020	0.014	0.011±0.001
^{131}I	0.014	0.007	0.003	0.009±0.001
^{111}In	0.022	0.015	0.010	0.009±0.001
^{99m}Tc	0.028	0.022	0.016	0.013±0.001
^{201}Tl	0.020	0.014	0.008	0.008±0.001

Overall, however, the SAM and power spectral density method shows tremendous improvement over the methods described in Sections 5.2 and 5.3. If this new method had been implemented earlier, we would have shown perfect identification results with the pedestrian RPM at the 2nd SCINTILLA benchmark for all sources travelling at 1.2 m/s. Section 5-6 attempts to quantify how the different radionuclide identification algorithms match up against each other.

5.6 Comparison of radionuclide identification methods using F-scores

F-scores provide a statistical measure of radionuclide identification algorithm performance, while also factoring in a system's susceptibility to false negatives, i.e. not even alarming on a present source [91].The F-score (F) (Equation 5-7) utilizes both precision (p) and recall (r) values shown in Equations 5-5 and 5-6. Precision and recall values are based upon the system's true positive alarms and correct IDs (t_p), incorrect IDs or false positives (f_p), and not seeing a present source or false negatives (f_n):

$$p = \frac{t_p}{t_P + f_p}, \tag{5-5}$$

$$r = \frac{t_p}{t_p + f_n}, \tag{5-6}$$

$$F = \frac{(1+\beta^2)pr}{\beta^2 p + r}, \tag{5-7}$$

where β is a weighting factor that can be used to emphasize the importance of precision (higher correct ID rate at cost of more false negatives) versus recall (lower false positive rate at cost of worse correct ID rate). In the former case, a β value of 2 might be chosen, whereas in the latter case a β value of 0.5 might be chosen. A β value of 1 indicates no bias towards either precision or recall.

The three different isotope identification algorithms introduced in Sections 5.2, 5.3, and 5.5 are compared for a mixture of SCINTILLA and medical isotope data in Table 5-7 [81]. The F-scores reveal the CDF method was an improvement over the modified PHD method, while the power spectral density and spectral angular mapper-based identification radionuclide identification algorithm performs best overall. Even this method has its limitation too. Table 5-8 compares F-scores for the dataset used in Table 5-7 with a more challenging dataset for which the 2.2 m/s versus 1.2 m/s source transit speed datasets are used from SCINTILLA and only 400 versus 1,000 good pulses are used for each medical isotope data trial. While the F-scores decrease to 0.91 for this more challenging dataset, the power spectral density and spectral angular mapper-based identification algorithm still manages to outperform the other algorithms' performances even though these inferior algorithms are using a less challenging dataset.

Many different algorithms were explored with the goal of performing on-the-fly radionuclide identification with organic scintillators. The most challenging sources to detect were low energy gamma-ray photon sources, like ^{241}Am and ^{57}Co. The identification algorithm using power spectral density and spectral angular mapper showed the most promise in the end. This algorithm resulted in a very high positive identification rate even for low energy gamma-ray photon sources, and for datasets with very few counts.

Table 5-7. Precision, recall, and F-scores computed for SCINTILLA pedestrian RPM datasets with 1.2 m/s source transit speed, and medical isotope datasets consisting of 1,000 good pulses. The following three isotope identification algorithms are compared: identification using least squares comparison with modified PHDs from Section 5.2 (Method 1), identification using least squares comparison with cumulative distribution functions from Section 5.3 (Method 2), and identification using power spectral density and spectral angular mapper from Section 5.5 [81].

	Method 1	Method 2	Method 3
Precision	0.58	0.70	1.0
Recall	0.99	0.99	1.0
$F(\beta = 1)$	0.73	0.82	1.0
$F(\beta = 0.5)$	0.63	0.74	1.0
$F(\beta = 2)$	0.87	0.92	1.0

Table 5-8. Precision, recall, and F-scores computed for two datasets. Dataset 1 contains SCINTILLA pedestrian RPM datasets with 1.2 m/s source transit speed, and medical isotope datasets consisting of 1,000 good pulses. The more challenging dataset 2 contains the 2.2 m/s source transit speed SCINTILLA datasets and medical radionuclide datasets containing only 400 net accepted pulses. F-scores are computed for both datasets using the identification algorithm using power spectral density and spectral angular mapper from Section 5.5 [81].

	Dataset 1	Dataset 2
Precision	1.0	0.90
Recall	1.0	0.92
$F(\beta = 1)$	1.0	0.91
$F(\beta = 0.5)$	1.0	0.91
$F(\beta = 2)$	1.0	0.91

5.7 Identifying Multiple Isotopes Simultaneously

So far all examples have only involved the presence of a single radionuclide. Correctly identifying two or more present radionuclides simultaneously represents a serious escalation in problem difficulty and complexity. Two scenarios must be addressed for a typical RPM. The first scenario involves the presence of two or more nuisance sources. For example, a truck driver might have recently undergone a nuclear medicine procedure and the truck driver might be transporting a large shipment of NORM-bearing cargo. The resulting mixed radiation signal must be resolved by the RPM and must not result in a misidentification. The second scenario involves an attempt to mask an SNM source with a NORM or medical source. The NORM to

SNM signal ratio would ideally be high as to spoof the RPM operator into believing that only a harmless NORM source is present.

Linear spectral un-mixing (LSU) algorithms are commonly used to dissect a mixed signal into its constituent components [92–94]. This algorithm assumes that the mixed signal M consists of a linear combination of n possible source terms (radionuclides S_i) at different fractions c_i as shown in Equation 5-8:

$$M = c_1 S_1 + c_2 S_2 + \cdots + c_n S_n. \tag{5-8}$$

One then calculates all difference equations simultaneously between M and all reference spectra S_i for all values of c_i constrained to $c_i \geq 0$ (Equation 5-9). One then solves for minima to get best fit values for c_i as shown in Equation 5-10:

$$M - c_1 S_1 - c_2 S_2 - \cdots c_n S_n = min, \tag{5-9}$$

$$\min_c \|\boldsymbol{S} * c - M\|,\ c \geq 0\ . \tag{5-10}$$

The mixed source signal array M and reference matrix S could consist of gamma-ray PHDs, CDFs, or power spectral densities of CDFs. A code was written to test all three data formats with M containing up to three isotopes mixed in user-defined ratios. The simplest scenario involves an un-mixed single source. The results for 1.2 m/s source transit speed pedestrian RPM ^{137}Cs and WGPu data are shown in Table 5-9. The coefficients for the correct radionuclide, in particular in the case of the WGPu, show a high degree of variability between datasets. Overall, however, the coefficient for the correct isotope clearly stands out against the much lower coefficients for absent isotopes.

Table 5-9. Isotope fraction coefficients computed for an LSU algorithm for un-mixing pedestrian RPM data consisting solely of WGPu or ^{137}Cs measurements. The averages and standard deviations of coefficients computed for each possible isotope use 30 three second measurement data sets as inputs. Inputs are either PHDs, modified CDFs ($y(n)$), or power spectral densities of $y(n)$.

	100% WGPu			100% Cs137		
Isotopes	PHD LSU	CDF LSU	CDF PSD LSU	PHD LSU	CDF LSU	CDF PSD LSU
^{241}Am	0.19±0.13	0.11±0.12	0.18±0.14	0.05±0.07	0.01±0.03	0.03±0.05
^{133}Ba	0.07±0.12	0.05±0.08	0.07±0.12	0.01±0.03	0.00±0.01	0.00±0.02
^{57}Co	0.06±0.08	0.02±0.04	0.03±0.06	0.02±0.05	0.00±0.01	0.01±0.02
^{137}Cs	0.01±0.02	0.00±0.00	0.01±0.03	0.75±0.14	0.93±0.12	0.85±0.09
HEU	0.05±0.09	0.00±0.01	0.02±0.04	0.00±0.01	0.00±0.00	0.00±0.01
^{226}Ra	0.01±0.04	0.00±0.00	0.01±0.03	0.00±0.02	0.01±0.05	0.00±0.01
WGPu	0.47±0.29	0.66±0.20	0.53±0.27	0.00±0.00	0.00±0.00	0.00±0.00
^{18}F	0.02±0.04	0.00±0.01	0.01±0.03	0.07±0.07	0.03±0.07	0.08±0.08
^{67}Ga	0.01±0.03	0.03±0.06	0.01±0.04	0.00±0.01	0.00±0.01	0.00±0.00
^{123}I	0.01±0.03	0.01±0.02	0.02±0.04	0.00±0.01	0.00±0.01	0.00±0.00
^{131}I	0.05±0.06	0.04±0.05	0.03±0.05	0.03±0.05	0.01±0.02	0.02±0.04
^{111}In	0.01±0.02	0.01±0.02	0.02±0.03	0.01±0.02	0.01±0.02	0.00±0.00
^{99m}Tc	0.02±0.03	0.02±0.03	0.02±0.03	0.00±0.01	0.00±0.01	0.00±0.00
^{201}Tl	0.03±0.08	0.03±0.05	0.02±0.06	0.01±0.04	0.00±0.00	0.01±0.03

Table 5-10 shows LSU results for two sources mixed in a 1:1 ratio. The 1:1 mixture of the two medical isotopes ^{99m}Tc and ^{67}Ga un-mixes nearly perfectly with the LSU code. The CDFs in question, including the CDF for the mixed source are given in Figure 5-15. The averaged un-mixing results for c_i are shown in pie chart for in Figure 5-16. For the 1:1 mixture of ^{137}Cs and WGPu, the ^{137}Cs is easily identified at approximately the correct percentage, but the WGPu content, while mostly noticeably above any of the absent sources, is significantly underestimated. However, for purposes of RPM operation it is most important that the presence of SNM is detected. The estimate of the exact ratio of which it might be present with other sources is not a consequential measurement parameter.

Table 5-10. Isotope fraction coefficients computed for an LSU algorithm for un-mixing pedestrian RPM data consisting of ^{99m}Tc and ^{67}Ga or ^{137}Cs and WGPu mixed in a 1:1 ratio. The averages and standard deviations of coefficients computed for each possible isotope use 30 three second measurement data sets as inputs. Inputs are either PHDs, modified CDFs ($y(n)$), or power spectral densities of $y(n)$.

	1:1 ^{99m}Tc:^{67}Ga			1:1 ^{137}Cs:WGPu		
Isotopes	PHD LSU	CDF LSU	CDF PSD LSU	PHD LSU	CDF LSU	CDF PSD LSU
^{241}Am	0.00±0.00	0.00±0.00	0.00±0.00	0.14±0.09	0.17±0.07	0.15±0.08
^{133}Ba	0.00±0.01	0.01±0.01	0.00±0.01	0.03±0.06	0.05±0.09	0.02±0.04
^{57}Co	0.01±0.01	0.01±0.01	0.01±0.01	0.06±0.07	0.07±0.08	0.07±0.07
^{137}Cs	0.00±0.01	0.02±0.01	0.04±0.03	0.40±0.11	0.41±0.11	0.52±0.10
HEU	0.00±0.00	0.00±0.00	0.00±0.00	0.03±0.05	0.02±0.05	0.02±0.05
^{226}Ra	0.00±0.00	0.00±0.01	0.00±0.00	0.09±0.13	0.06±0.12	0.07±0.10
WGPu	0.00±0.00	0.00±0.00	0.00±0.00	0.14±0.18	0.05±0.10	0.08±0.12
^{18}F	0.01±0.01	0.00±0.00	0.03±0.02	0.03±0.04	0.04±0.05	0.02±0.04
^{67}Ga	0.41±0.06	0.42±0.05	0.25±0.08	0.00±0.01	0.02±0.04	0.00±0.00
^{123}I	0.01±0.03	0.02±0.04	0.01±0.03	0.00±0.01	0.00±0.01	0.01±0.02
^{131}I	0.02±0.02	0.01±0.02	0.05±0.04	0.04±0.07	0.05±0.07	0.02±0.05
^{111}In	0.02±0.03	0.02±0.03	0.00±0.00	0.01±0.02	0.02±0.04	0.01±0.02
^{99m}Tc	0.50±0.04	0.49±0.04	0.53±0.05	0.02±0.03	0.02±0.03	0.02±0.02
^{201}Tl	0.01±0.03	0.00±0.00	0.08±0.06	0.02±0.04	0.01±0.02	0.01±0.04

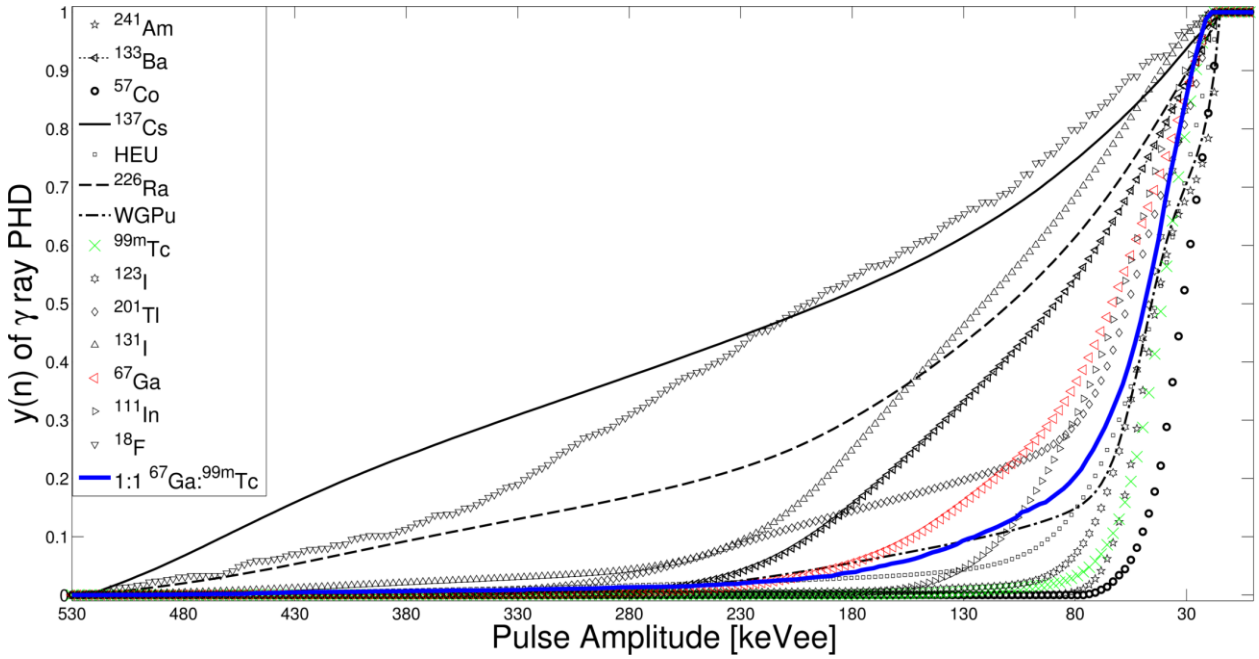

Figure 5-15. Library CDFs and example of RPM data consisting of ^{67}Ga and ^{99m}Tc mixed in a 1:1 ratio.

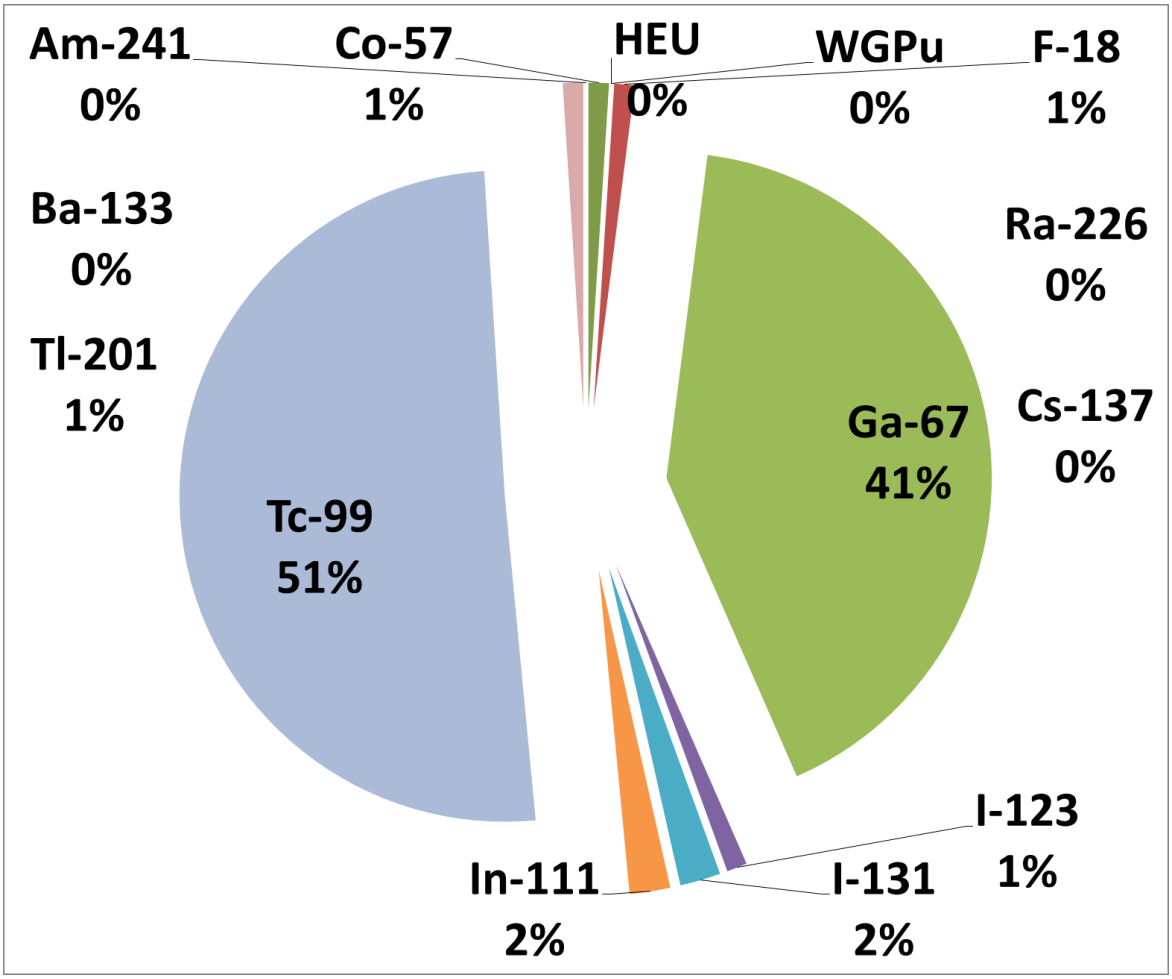

Figure 5-16. Average isotope fraction coefficients, c_i, computed for an LSU algorithm for un-mixing pedestrian RPM data consisting of ^{67}Ga and ^{99m}Tc mixed in a 1:1 ratio. The averages and standard deviations of coefficients computed for each possible isotope use 30 three second measurement data sets as inputs. Inputs are PHDs.

A more challenging scenario involves the mixing of sources in unequal proportions. This represents a masking scenario in which a stronger (benign) source is used to overshadow the signatures of a weaker but illicit radiation source. Table 5-11 shows LSU un-mixing results for ^{137}Cs and WGPu pedestrian RPM data mixed in a 2:1 and 1:2 ratio. The ratios might not reconstruct perfectly in the LSU results, but the trends between the 1:2 versus 2:1 ratio are apparent. Both sources are clearly identified in the 1:2 source ratio scenario, but the WGPu is barely detected in many of the 2:1 ^{137}Cs to WGPu ratio examples.

Table 5-11. Isotope fraction coefficients computed for an LSU algorithm for un-mixing pedestrian RPM data consisting of ^{137}Cs and WGPu in a 2:1 or 1:2 ratio. The averages and standard deviations of coefficients computed for each possible isotope use 30 three second measurement data sets as inputs. Inputs are either PHDs, modified CDFs ($y(n)$), or power spectral densities of $y(n)$.

	2:1 ^{137}Cs:WGPu			1:2 ^{137}Cs:WGPu		
Isotopes	PHD LSM	CDF LSM	CDF PSD LSM	PHD LSM	CDF LSM	CDF PSD LSM
^{241}Am	0.10±0.08	0.13±0.07	0.11±0.08	0.17±0.10	0.20±0.09	0.18±0.10
^{133}Ba	0.03±0.06	0.03±0.07	0.01±0.04	0.05±0.07	0.07±0.12	0.03±0.05
^{57}Co	0.05±0.07	0.06±0.08	0.05±0.07	0.06±0.07	0.08±0.08	0.07±0.07
^{137}Cs	0.56±0.12	0.59±0.13	0.67±0.09	0.24±0.10	0.24±0.08	0.34±0.11
HEU	0.02±0.03	0.01±0.02	0.02±0.05	0.04±0.07	0.03±0.07	0.03±0.06
^{226}Ra	0.06±0.09	0.03±0.10	0.03±0.07	0.09±0.14	0.05±0.11	0.08±0.12
WGPu	0.07±0.10	0.01±0.04	0.03±0.06	0.23±0.22	0.14±0.17	0.17±0.18
^{18}F	0.03±0.04	0.04±0.06	0.03±0.04	0.03±0.04	0.03±0.04	0.02±0.04
^{67}Ga	0.00±0.01	0.01±0.04	0.00±0.01	0.00±0.02	0.01±0.04	0.00±0.00
^{123}I	0.00±0.01	0.00±0.02	0.01±0.02	0.01±0.02	0.01±0.02	0.01±0.03
^{131}I	0.03±0.06	0.04±0.05	0.02±0.04	0.05±0.07	0.07±0.07	0.03±0.07
^{111}In	0.01±0.02	0.03±0.03	0.00±0.01	0.01±0.02	0.02±0.04	0.01±0.01
^{99m}Tc	0.01±0.02	0.01±0.02	0.01±0.02	0.02±0.03	0.02±0.03	0.02±0.03
^{201}Tl	0.01±0.03	0.01±0.02	0.01±0.03	0.02±0.05	0.01±0.03	0.02±0.04

Finally, Table 5-12 contains LSU results for a source consisting of three radionuclides together, namely WGPU (SNM), ^{137}Cs (industrial), and ^{99m}Tc (medical) in 1:3:1 ratio. The CDFs in question, including the CDF for the mixed source are given in Figure 5-17. The averaged un-mixing results for c_i are shown in pie chart for in Figure 5-18.The presence of all three isotopes is clear in the un-mixed identification results, though ^{241}Am is erroneously also identified. This is the lowest energy gamma-ray source considered, and its CDF and PHD lines up with the low energy portion of many other sources, thus causing it to often look similar to other sources. ^{241}Am also contributes heavily as a decay product to the gamma emissions from WGPu. ^{241}Am has a specific intensity of $4.54 * 10^{10} \frac{\gamma}{s\ g}$ for its characteristic 60 keV gamma ray. This value is orders of magnitudes higher than the specific activities for many of the most common plutonium characteristic gamma ray photons. Even though ^{241}Am only accounts for a tenth of a percent of the mass of the JRC WGPu sample, its high specific decay activity results in the ^{241}Am 60 keV

gamma ray accounting for over 97% of the WGPu sample gamma ray emissions. The frequent misidentification of WGPu as ^{241}Am therefore should not be surprising.

Overall, it is unclear whether using PHDs, CDFs, or power spectral densities as inputs for a LSU algorithm will produce the best results. However, with data of high statistical uncertainty and no isotope characteristic photopeaks, it is remarkable to what degree the constituents of a mixed source consisting of up to three radionuclides can be correctly identified.

Table 5-12. Isotope fraction coefficients computed for an LSU algorithm for un-mixing pedestrian RPM data consisting of ^{137}Cs, WGPu, and ^{99m}Tc mixed in a 1:3:1. The averages and standard deviations of coefficients computed for each possible isotope use 30 three second measurement data sets as inputs. Inputs are either PHDs, modified CDFs ($y(n)$), or power spectral densities of $y(n)$.

	1:3:1 ^{137}Cs:WGPu:^{99m}Tc		
Isotopes	PHD LSU	CDF LSU	CDF PSD LSU
^{241}Am	0.12±0.10	0.16±0.08	0.18±0.07
^{133}Ba	0.03±0.07	0.03±0.06	0.00±0.00
^{57}Co	0.06±0.06	0.10±0.10	0.09±0.08
^{137}Cs	0.13±0.07	0.14±0.05	0.32±0.07
HEU	0.03±0.05	0.03±0.07	0.05±0.07
^{226}Ra	0.03±0.08	0.02±0.05	0.01±0.03
WGPu	0.28±0.22	0.17±0.16	0.07±0.11
^{18}F	0.02±0.04	0.02±0.03	0.02±0.03
^{67}Ga	0.01±0.02	0.01±0.03	0.00±0.00
^{123}I	0.01±0.03	0.01±0.02	0.05±0.06
^{131}I	0.04±0.05	0.07±0.06	0.00±0.01
^{111}In	0.01±0.02	0.02±0.03	0.00±0.00
^{99m}Tc	0.19±0.04	0.20±0.04	0.20±0.07
^{201}Tl	0.02±0.05	0.02±0.03	0.02±0.04

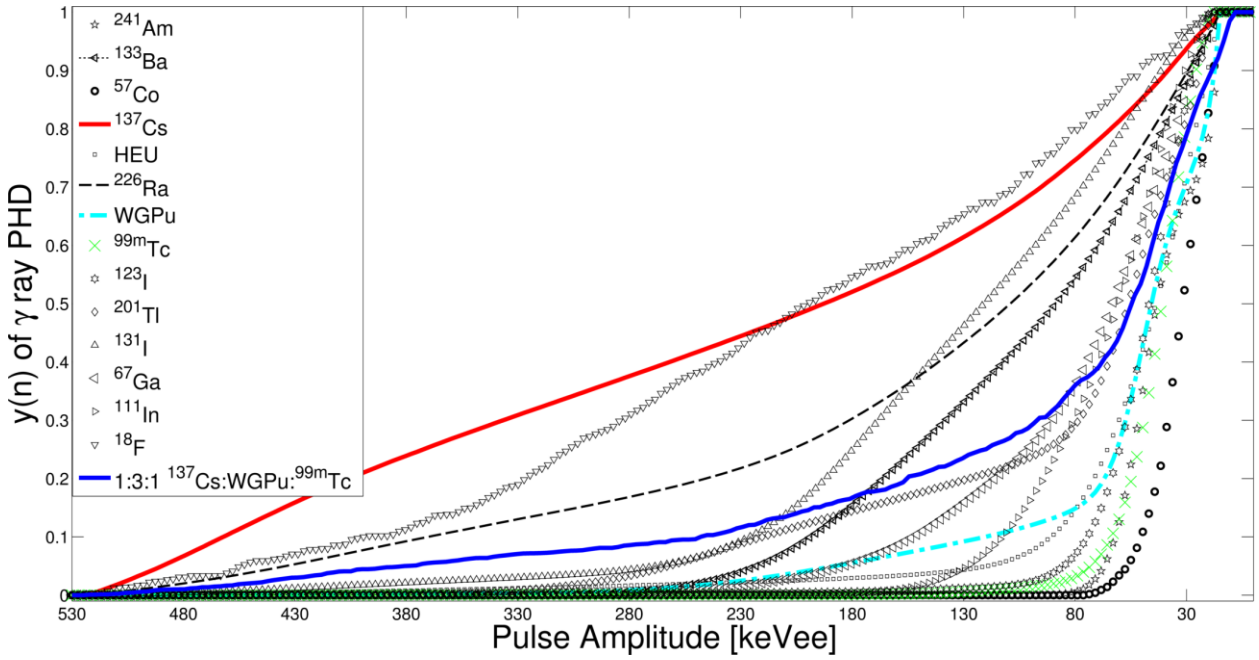

Figure 5-17. Library CDFs and example of RPM data consisting of ^{137}Cs, WGPu, and ^{99m}Tc mixed in a 1:3:1 ratio.

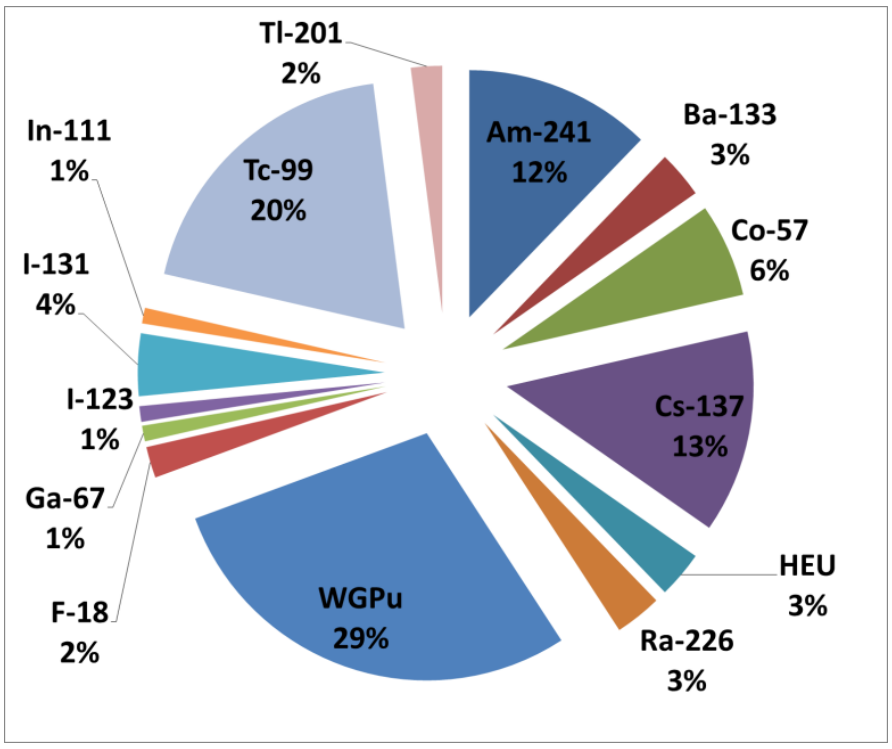

Figure 5-18. Average isotope fraction coefficients, c_i, computed for an LSU algorithm for un-mixing pedestrian RPM data consisting of ^{137}Cs, WGPu, and ^{99m}Tc mixed in a 1:3:1 ratio. The averages and standard deviations of coefficients computed for each possible isotope use 30 three second measurement data sets as inputs. Inputs are PHDs.

Chapter 6. Summary and Conclusions

In the first 2016 United States Presidential debate candidate Hillary Clinton said the following about her opponent and nuclear weapons: "And, in fact, his cavalier attitude about nuclear weapons is so deeply troubling. That is the number-one threat we face in the world. And it becomes particularly threatening if terrorists ever get their hands on any nuclear material [95]." Terrorists getting their hands on nuclear material is one of the major threats that RPMs address by making it difficult for terrorists to move nuclear and radiological material across borders with impunity.

RPMs screen vehicles, cargo, and people by looking for elevated neutron and gamma-ray photon count rates above natural background radiation. However, two challenges are hampering the effectiveness of our globally deployed RPM network. First, supplies of the detector material of choice for neutron detection, ^{3}He, are gradually running out and are becoming prohibitively expensive. Second, the number of actual interdictions of nuclear and radiological materials pales in comparison to the hundreds of thousands of radiation nuisance alarms that RPM operators must sift through annually. Because RPMs only measure radiation count rates, the vast majority of currently deployed RPMs have no way of quickly distinguishing a radiation alarm caused by hidden SNM from radiation alarms caused by NORM-bearing cargo and recent nuclear medicine patients. Processing these nuisance alarms is time and money intensive for the RPM operators, it distracts from their actual mission and lowers the seriousness with which each subsequent RPM radiation alarm is treated, and it's a nuisance to nuclear medicine patients and truck drivers who experience additional delays while crossing a border.

To address these aforementioned issues, we have developed RPMs that use alternatives to ^{3}He for neutron detection, and that can perform on-the-fly radionuclide identification for gamma-ray photon alarms. Modeling and lab-scale experiments were extensively used to investigate the feasibility of this undertaking and to design our RPM. MCNP models and ROC curve analysis were used to develop a pedestrian and a vehicle RPM using organic liquid scintillation detectors [49].

The RPM prototypes were extensively tested at two experimental campaigns at the European Commission Joint Research Centre in Ispra, Italy, at a purpose-built RPM testing facility. This facility allowed for RPMs to be tested with moving radiation sources in a variety of shielding configurations. Sources included a variety of ^{252}Cf neutron sources, industrial gamma-ray photon sources, and, most importantly, actual SNM sources of HEU and WGPu. The RPMs were tested on their ability to not false alarm on occupancies in which only natural background radiation was present. Additionally RPMs were tested for their ability to alarm on the presence of (shielded) neutron and gamma-ray photon sources. Our prototypes performed exceedingly well in all of these categories [39].

Reliable on-the-fly radionuclide identification is one of the cornerstones of this dissertation. The challenge of this undertaking is twofold. First, unlike inorganic scintillators and semi-conductor-based radiation detectors, organic scintillators provide no isotope-specific photo-peak information. Instead organic scintillator output arises from Compton scattering interactions in the detectors. Second, RPM measurement times are incredibly short, on the order of three seconds, so the acquired signal is often poorly converged and exhibits dreadful statistics with so few measured data. Making a positive identification on such poor quality data is incredibly challenging.

In addition to the radionuclides measured in Italy, we measured seven different common medical isotopes at the University of Michigan's C.S. Mott Children's Hospital. Medical isotopes are a growing source of RPM nuisance alarms. In fact, in addition to kitty litter, the medical isotope ^{99m}Tc is the most common source of RPM nuisance alarms[28,30]. Therefore it was crucial to add medical isotopes to our radionuclide identification efforts.

Many radionuclide identification algorithms were explored, developed, implemented, and then later discarded for not producing results with the type of reliability and precision required for such an important task. Initial efforts focused on template matching with reference PHDs using a least squares comparison method between measured and reference spectra. While many ways of improving this method were explored, none could completely overcome the inherent noisiness of the short measurement time PHDs. The next phase of algorithm development focused on using CDFs to smoothen the inherent noisiness of short measurement time PHDs. While this method led to drastic improvements for identifying some isotopes, the CDF method

did not show improvements across the board for all radionuclides. Especially for lower energy gamma-ray photon emitting sources, too many radionuclides' gamma-ray photon emissions resulted in CDFs too similar in appearance to be distinguished reliably through a simple least squares algorithm. Finally, Fourier analysis was used to compute the power spectral densities of CDFs. The power spectral densities of measured and reference spectra were compared with a spectral angle mapper to compute the best matches. This method resulted in near 100% correct identification rates for all SNM, industrial, and medical isotopes with datasets containing as few as 400 detected events from the radiation source.

F-score analysis was used to quantitatively compare the three developed radionuclide identification algorithms. For the less challenging dataset 1, the F-score for $\beta = 1$ improved from 0.72 for the PHD least squares comparison method, to 0.82 for the CDF least squares comparison method, to 1.0 for the power spectral density and spectral angle mapper method. For this final identification algorithm, even the more challenging dataset 2 resulted in a high F-score for $\beta = 1$ of 0.91.

While these radionuclide identification results are excellent, further work must go into handling the presence of multiple different radiation sources as well as the effects of shielding on the identification algorithms. Nevertheless, some degree of success was achieved with a LSU algorithm for identifying the components of mixed sources with up to three constituents.

The designed RPM shows great promise in a lab controlled environment. However, more research and development would be required to bring the developed prototypes to market. Given more time and resources, more investigations into the choice of detector material and detector readout would be appropriate. Due to time and budget constraints, and early decision was made to design the prototypes with liquid organic scintillation detectors which were available to us in abundance. Due to the small probability of leaks developing in liquid scintillator detectors, solid detector materials are favored over liquids for field deployment. Alternative solid organic scintillator detectors should be further investigated for their RPM suitability. These materials include stilbene [43,51,67], a crystalline solid organic scintillator, as well as pulse shape discrimination-capable plastic organic scintillation detectors [96]. Further ROC curve and cost analysis would be required to investigate the feasibility of using these detectors in an RPM.

Furthermore, all measurements in this dissertation were performed in relatively climate controlled laboratory environments. RPMs in the field must cope with a wide range of operating temperatures, air humidity, and other climatic phenomena. Some detector materials, like stilbene, cannot cope with large temperature gradients [43,51,67,97,98]. Therefore, before field deployment all candidate RPM detector material performances would need to be studied in depth in a user controllable environmental chamber.

Another potential area of further improvement and investigation pertains to the detector light readout. Photomultiplier tubes, as used in our RPM prototypes, have two significant drawbacks. Photomultiplier tubes requires high voltage to operate, and they take up a lot of volume relative to the active detector volume. Solid state readouts, like SiPMs, have emerged as a viable alternative to photomultiplier tubes. SiPMs require low voltage to operate, and only take up a small fraction of the volume of photomultiplier tubes [43]. However, each individual SiPM only reads out a small surface area, so there exist associated physical and cost challenges with expanding the use of SiPMs to large arrays of larger volume detectors, as would be likely in an RPM application.

Finally, further studies are needed to investigate the RPM response to high activity gamma-ray photon sources. The digitizer uses an acquisition time window 100s of nanoseconds in length for each pulse above the set energy threshold. In the presence of a high activity source (GBq or higher), the probability of measuring multiple gamma-ray photons within this set time window increases substantially. Such pulses are often referred to as double pulses or pile-up pulses. If not corrected for, double pulses would be treated as a single pulse with a very large tail integral, leading to the misclassification of double pulses from gammas as a single neutron pulse. However, current research into double pulse cleaning and/or recovery could be implemented in the RPM algorithms to deal with the issue of double pulses [99].

Despite these outstanding challenges, several RPM prototypes were developed, built, and tested rigorously under a variety of testing conditions. The results should provide encouragement to the prospects of commercializing ^{3}He-free RPMs, and RPMs capable of distinguishing SNM sources from nuisance radiation sources.

Appendices
Appendix A
RPM XML File Output Example

```
<N42InstrumentData xmlns="http://physics.nist.gov/Divisions/Div846/Gp4/ANSIN4242/2005/ANSIN4242" xmlns:xsi="http://www.w3.org/20
    <Measurement>
        <InstrumentInformation>
            <Manufacturer>DNNG at the University of Michigan</Manufacturer>
            <InstrumentID>8 Liquid Scintillator Array</InstrumentID>
        </InstrumentInformation>
        <DetectorData>
            <StartTime>2014-02-13T11:04:32</StartTime>
            <SampleRealTime>PT3S</SampleRealTime>
            <AlarmSummary>1</AlarmSummary>
            <AlarmDescription>Gamma Alarm!    1.33333 neutron counts/s and 1293.67 gamma counts/s measured.</AlarmDescription>
            <DetectorMeasurement DetectorType="Gamma">
                <GrossCounts>3881</GrossCounts>
            </DetectorMeasurement>
            <DetectorMeasurement DetectorType="Neutron">
                <GrossCounts>4</GrossCounts>
            </DetectorMeasurement>
        </DetectorData>
        <AnalysisResults>
            <NuclideAnalysis>
                <NuclideName>Am-241</NuclideName>
            </NuclideAnalysis>
        </AnalysisResults>
    </Measurement>
</N42InstrumentData>
```

Figure A-1. Example of an XML file output for a single RPM occupancy for the pedestrian RPM tested at the 2nd SCINTILLA benchmark at the European Commission JRC in Ispra, Italy, in February 2014. The standardized XML file contains vital information, including a time stamp, gross neutron and gamma-ray photon counts and count rates, alarm type, and radionuclide identification result in the case of gamma alarms.

Appendix B
Pedestrian RPM Results for 2nd SCINTILLA Benchmark

Table B-1. Overview of test results for pedestrian RPM at 2nd SCINTILLA benchmark at JRC Ispra, Italy, in February 2014. Test results include false alarm test (top left), neutron alarm tests (folders 1-16), as well as gamma-ray photon alarm and ID tests (folders 17-50). The ID results in this table still use a method with weighting masks on the PHDs, thus the discrepancy to values shown elsewhere in Table 5-1 and Table 5-2.

False Alarm Test	0/2739														
Folder Number	Source	Activity (kBq or n/s)	Source ID	Speed (m/s)	Shielding Steel (cm)	Shielding Lead (cm)	Shielding HDPE (cm)	Source Height (m)	# Passages	Date (2014)	All Clears	Gamma Alarms	Neutron Alarms	Correct ID	Comments
1	Cf-252	20000	5549	2.2	1	0.5	0	1.2	30	10-Feb					
2	Cf-252	20000	5549	1.2	1	0.5	0	1.2	30	10-Feb	0	19	30	30	
3	Cf-252	20000	5549	3	1	0.5	0	1.2	30	10-Feb	0	0	30	30	
4	Cf-252	20000	5549	2.2	1	0.5	0	1.9	30	10-Feb	0	0	30	30	Two portals crashed. The test will be repeated.
5	Cf-252	20000	5549	2.2	1	0.5	0	1.9	30	11-Feb	0	0	30	30	Repetition of previous test
6	Cf-252	20000	5549	2.2	1	0.5	0	2.1	30	11-Feb	0	0	30	30	
7	Cf-252	10000	5987	2.2	1	0.5	0	1.2	30	11-Feb	2	0	28	28	
8	Cf-252	10000	5987	1.2	1	0.5	0	1.2	30	11-Feb	0	0	30	30	
9	Cf-252	20000	5549	2.2	1	0.5	8	1.2	30	11-Feb	16	1	14	14	
10	Cf-252	20000	5549	1.2	1	0.5	8	1.2	30	11-Feb	1	0	29	29	
11	Cf-252	10000	5987	2.2	1	0.5	8	1.2	30	11-Feb	30	0	0	0	
12	Cf-252	10000	5987	1.2	1	0.5	8	1.2	30	11-Feb	25	0	5	5	
13	Cf-252	10000	5987	2.2	1	0.5	4	1.2	30	11-Feb	15	0	15	15	
14	Cf-252	10000	5987	1.2	1	0.5	4	1.2	30	11-Feb	13	0	17	17	One portal crashed. No repetition
15	Cf-252	20000	5549	2.2	1	0.5	4	1.2	30	11-Feb	0	0	30	30	
16	Cf-252	20000	5549	1.2	1	0.5	4	1.2	30	11-Feb	1	18	29	29	
17	Co-60	259	591	2.2	0	0	0	1.2	30	11-Feb	0	30	0	5	
18	Co-60	259	591	1.2	0	0	0	1.2	30	12-Feb	0	30	0	17	
19	Co-60	259	591	2.2	0	0	0	2.5	30	12-Feb	1	29	0	0	Vehicular limits
20	Co-60	259	591	1.2	0	0	0	2	30	12-Feb	0	30	0	3	Pedestrian limits
21	WGPu	93%	CBNM93	2.2	0	0	0	1.2	30	12-Feb	0	30	0	13	
22	WGPu	93%	CBNM93	1.2	0	0	0	1.2	30	12-Feb	0	30	0	17	
23	WGPu	93%	CBNM93	2.2	1	0	0	1.2	30	12-Feb	0	30	0	2	
24	WGPu	93%	CBNM93	1.2	1	0	0	1.2	30	12-Feb	0	30	0	0	
25	Ba-133	110	6505	2.2	0	0	0	1.2	30	12-Feb	8	22	0	3	
26	Ba-133	110	6505	1.2	0	0	0	1.2	30	12-Feb	0	30	0	3	
27	Ba-133	110, 95, 96	6505, 6506, 6507	2.2	0	0	0	1.2	30	12-Feb	0	30	0	13	
28	Ba-133	110, 95, 97	6505, 6506, 6508	1.2	0	0	0	1.2	30	12-Feb	0	30	0	29	

29	Ba-133	110, 95, 98	6505, 6506, 6509	2.2	0	0	0	2.5	30	12-Feb	2	28	0	1	
30	Ba-133	110, 95, 99	6505, 6506, 6510	1.2	0	0	0	2	30	12-Feb	0	30	0	10	
31	Co-57	143, 61		2.2	0	0	0	1.2	30	13-Feb	11	19	0	15	
32	Co-57	143, 61		1.2	0	0	0	1.2	30	13-Feb	0	30	0	29	
33	Am-241	1480, 370, 370		2.2	0	0	0	1.2	30	13-Feb					The rail broke down. Runs discarded.
34	Am-241	1480, 370, 370		2.2	0	0	0	1.2	30	13-Feb	12	18	0	13	Repeated measuremen t
35	Am-241	1480, 370, 370		1.2	0	0	0	1.2	30	13-Feb	0	30	0	16	
36	Cs-137	370		2.2	0	0	0	1.2	30	13-Feb	0	30	0	4	
37	Cs-137	370		1.2	0	0	0	1.2	30	13-Feb	0	30	0	17	
38	Cs-137	3700		2.2	3	0	0	2.1	30	13-Feb	0	30	0	0	
39	Cs-137	3700		1.2	3	0	0	1.9	30	13-Feb	0	30	0	0	
40	HEU	51g - 89.9%		1.2	0	0	0	1.2	30	13-Feb	0	30	0	30	
41	HEU + Ra-226	51g - 89.9%, 300		1.2	0	0	0	1.2	30	13-Feb	0	30	0	1	
42	HEU + Co-57	51g - 89.9%, 634		1.2	0	0	0	1.2	30	13-Feb	0	30	0	0	
43	HEU	51g - 89.9%		2.2	0	0	0	1.2	30	13-Feb	0	31	0	26	
44	Cs-137	370000		2.2	0	0	0	1.2	6	14-Feb	0	6	6	6	
45	Cs-137	370000		1.2	0	0	0	1.2	6	14-Feb	0	6	6	6	
46	Cs-137, Cf-252	370000, 20000		1.2				1.2	6	14-Feb	0	6	6	6	
47	Cs-137, Cf-252	370000, 20000		2.2				1.2	6	14-Feb	0	6	6	6	
48	Cs-137	370000		Static 30s	0	0	0	1.2	2	14-Feb	0	8	6	6	
49	WGPu, U-232	93%, 370000		1.2	0	0	0	1.2	30	14-Feb	0	30	1	0	
50	WGPu, Ba-133	93%, 110, 95, 96		1.2	0	0	0	1.2	40	14-Feb	0	40	0	0	Added another 430 kBq in the last 10 passages

Table B-2. Radionuclide identification results using SAM on power spectral densities of measured CDFs of thirty datasets of ~1000 good pulses of ^{99m}Tc measured with the 7.6 cm diameter cylindrical volume EJ309 organic liquid scintillation detector. These measured spectra are compared the reference spectra for each of the thirteen radionuclides measured with the pedestrian RPM. The lowest SAM value corresponds to the best identification match. For this scenario, all thirty measurements of ^{99m}Tc were identified correctly.

Trial	1	2	3	4	5	6	7	8	9	10	11	12	13	14	15	16	17	18	19	20	21	22	23	24	25	26	27	28	29	30
Am241	0.021	0.021	0.021	0.021	0.021	0.021	0.021	0.021	0.021	0.021	0.021	0.021	0.021	0.021	0.021	0.021	0.021	0.021	0.021	0.021	0.021	0.021	0.021	0.021	0.021	0.021	0.021	0.021	0.021	0.021
Ba133	0.013	0.013	0.014	0.014	0.013	0.014	0.013	0.014	0.013	0.014	0.013	0.013	0.013	0.013	0.013	0.013	0.013	0.014	0.013	0.013	0.013	0.013	0.014	0.013	0.013	0.013	0.014	0.013	0.014	0.013
Co57	0.016	0.016	0.016	0.016	0.016	0.016	0.016	0.016	0.016	0.016	0.016	0.016	0.016	0.016	0.016	0.016	0.016	0.016	0.016	0.016	0.016	0.016	0.016	0.016	0.016	0.016	0.016	0.016	0.016	0.016
Co60	0.019	0.019	0.019	0.019	0.019	0.019	0.019	0.019	0.019	0.019	0.019	0.018	0.019	0.019	0.019	0.019	0.019	0.019	0.019	0.019	0.018	0.019	0.019	0.019	0.018	0.018	0.019	0.019	0.019	0.019
Cs137	0.008	0.008	0.008	0.009	0.008	0.008	0.008	0.009	0.008	0.008	0.008	0.008	0.009	0.008	0.008	0.008	0.008	0.009	0.008	0.008	0.008	0.008	0.008	0.008	0.008	0.008	0.008	0.008	0.008	0.008
HEU	0.015	0.015	0.016	0.016	0.016	0.016	0.015	0.016	0.016	0.016	0.016	0.015	0.016	0.016	0.016	0.015	0.016	0.016	0.015	0.015	0.015	0.015	0.016	0.016	0.015	0.015	0.016	0.016	0.016	0.015
Ra226	0.017	0.017	0.017	0.018	0.017	0.017	0.017	0.018	0.017	0.017	0.017	0.017	0.018	0.017	0.017	0.017	0.018	0.018	0.017	0.017	0.017	0.017	0.017	0.017	0.017	0.017	0.018	0.017	0.018	0.017
WGPu	0.019	0.019	0.020	0.020	0.019	0.019	0.019	0.019	0.019	0.019	0.019	0.019	0.019	0.019	0.019	0.019	0.019	0.019	0.019	0.019	0.019	0.019	0.020	0.019	0.019	0.019	0.019	0.019	0.019	0.019
Ga67	0.010	0.009	0.010	0.010	0.010	0.010	0.009	0.010	0.009	0.010	0.010	0.009	0.010	0.010	0.010	0.009	0.010	0.010	0.009	0.010	0.009	0.009	0.010	0.009	0.009	0.009	0.010	0.009	0.010	0.010
I123	0.004	0.004	0.004	0.005	0.004	0.005	0.004	0.005	0.004	0.004	0.004	0.003	0.004	0.004	0.004	0.004	0.005	0.005	0.004	0.004	0.004	0.004	0.005	0.004	0.004	0.004	0.005	0.005	0.005	0.004
I131	0.015	0.015	0.016	0.016	0.016	0.016	0.015	0.016	0.016	0.016	0.016	0.015	0.016	0.016	0.016	0.016	0.016	0.016	0.015	0.016	0.015	0.015	0.016	0.016	0.015	0.015	0.016	0.016	0.016	0.016
In111	0.008	0.008	0.009	0.009	0.009	0.009	0.008	0.009	0.009	0.009	0.009	0.008	0.009	0.009	0.009	0.009	0.009	0.009	0.009	0.009	0.008	0.008	0.009	0.009	0.008	0.008	0.009	0.009	0.009	0.009
Tc99	0.002	0.002	0.002	0.002	0.002	0.002	0.002	0.002	0.002	0.002	0.002	0.002	0.002	0.002	0.002	0.002	0.002	0.002	0.002	0.002	0.002	0.002	0.003	0.002	0.002	0.002	0.002	0.002	0.002	0.002
Tl201	0.010	0.009	0.010	0.010	0.010	0.010	0.009	0.010	0.009	0.010	0.010	0.009	0.010	0.010	0.010	0.009	0.010	0.010	0.010	0.010	0.009	0.009	0.010	0.010	0.009	0.009	0.010	0.010	0.010	0.010
Result	**Tc99**	**Tc99**	**Tc99**	**Tc99**	**Tc99**	**Tc99**	**Tc99**	**Tc99**	**Tc99**	**Tc99**	**Tc99**	**Tc99**	**Tc99**	**Tc99**	**Tc99**	**Tc99**	**Tc99**	**Tc99**	**Tc99**	**Tc99**	**Tc99**	**Tc99**	**Tc99**	**Tc99**	**Tc99**	**Tc99**	**Tc99**	**Tc99**	**Tc99**	**Tc99**

Table B-3. Radionuclide identification results using SAM on power spectral densities of measured CDFs of thirty datasets of ~400 good pulses of ^{99m}Tc measured with the 7.6 cm diameter cylindrical volume EJ309 organic liquid scintillation detector. These measured spectra are compared the reference spectra for each of the thirteen radionuclides measured with the pedestrian RPM. The lowest SAM value corresponds to the best identification match. For this scenario, only 28 of thirty measurements of ^{99m}Tc were identified correctly, and the SAM values for 99mTc are twice as high on average compared to those from Table B-2 .

Trial	1	2	3	4	5	6	7	8	9	10	11	12	13	14	15	16	17	18	19	20	21	22	23	24	25	26	27	28	29	30
Am241	0.017	0.017	0.018	0.018	0.018	0.017	0.018	0.018	0.018	0.018	0.018	0.017	0.017	0.017	0.018	0.017	0.018	0.017	0.017	0.017	0.017	0.017	0.017	0.017	0.018	0.017	0.018	0.018	0.018	0.017
Ba133	0.013	0.012	0.014	0.014	0.013	0.013	0.013	0.014	0.014	0.013	0.014	0.012	0.013	0.013	0.014	0.013	0.013	0.013	0.012	0.012	0.012	0.013	0.013	0.013	0.013	0.013	0.014	0.013	0.013	0.013
Co57	0.011	0.010	0.011	0.012	0.011	0.011	0.011	0.012	0.012	0.011	0.012	0.010	0.011	0.011	0.012	0.011	0.011	0.011	0.011	0.011	0.011	0.011	0.011	0.011	0.011	0.011	0.012	0.011	0.011	0.011
Co60	0.017	0.016	0.018	0.018	0.018	0.018	0.018	0.018	0.019	0.018	0.018	0.017	0.017	0.017	0.018	0.017	0.018	0.018	0.017	0.017	0.017	0.017	0.018	0.018	0.018	0.017	0.018	0.018	0.018	0.018
Cs137	0.010	0.009	0.011	0.012	0.011	0.010	0.011	0.011	0.011	0.011	0.011	0.010	0.010	0.010	0.011	0.010	0.011	0.010	0.010	0.010	0.010	0.010	0.010	0.010	0.011	0.010	0.011	0.010	0.011	0.010
HEU	0.014	0.014	0.015	0.016	0.015	0.015	0.015	0.016	0.016	0.015	0.015	0.014	0.015	0.015	0.015	0.015	0.015	0.015	0.014	0.014	0.014	0.015	0.015	0.015	0.015	0.015	0.016	0.015	0.015	0.015
Ra226	0.012	0.011	0.013	0.013	0.012	0.012	0.013	0.013	0.013	0.013	0.013	0.011	0.012	0.012	0.013	0.012	0.013	0.012	0.012	0.012	0.012	0.012	0.012	0.012	0.013	0.012	0.013	0.012	0.013	0.012
WGPu	0.018	0.017	0.019	0.020	0.019	0.019	0.019	0.019	0.020	0.019	0.019	0.018	0.018	0.018	0.019	0.018	0.019	0.019	0.018	0.018	0.018	0.019	0.019	0.019	0.019	0.018	0.019	0.019	0.019	0.019
Ga67	0.009	0.008	0.010	0.010	0.010	0.009	0.009	0.010	0.010	0.009	0.010	0.008	0.009	0.009	0.010	0.009	0.010	0.009	0.008	0.009	0.009	0.009	0.009	0.009	0.010	0.009	0.010	0.009	0.010	0.009
I123	0.005	0.004	0.006	0.006	0.005	0.005	0.006	0.005	0.005	0.005	0.005	0.004	0.004	0.005	0.005	0.004	0.006	0.005	0.004	0.004	0.005	0.005	0.006	0.005	0.005	0.006	0.006	0.005	0.005	0.005
I131	0.014	0.014	0.016	0.016	0.015	0.015	0.015	0.016	0.016	0.015	0.016	0.014	0.015	0.015	0.015	0.015	0.016	0.015	0.014	0.015	0.015	0.015	0.015	0.015	0.015	0.015	0.016	0.015	0.016	0.015
In111	0.008	0.007	0.009	0.010	0.009	0.009	0.009	0.009	0.009	0.009	0.009	0.007	0.008	0.009	0.009	0.008	0.009	0.009	0.008	0.008	0.008	0.008	0.009	0.009	0.009	0.009	0.009	0.009	0.009	0.008
Tc99	0.004	0.004	0.004	0.005	0.003	0.003	0.004	0.003	0.003	0.004	0.003	0.004	0.003	0.003	0.004	0.003	0.004	0.004	0.004	0.003	0.004	0.003	0.004	0.003	0.004	0.004	0.003	0.003	0.003	0.003
Tl201	0.009	0.008	0.010	0.011	0.010	0.009	0.010	0.010	0.010	0.009	0.010	0.008	0.009	0.009	0.010	0.009	0.010	0.009	0.009	0.009	0.009	0.009	0.009	0.010	0.009	0.010	0.010	0.009	0.010	0.009
Result	**Tc99**	**I123**	**Tc99**	**Tc99**	**Tc99**	**Tc99**	**Tc99**	**Tc99**	**Tc99**	**Tc99**	**Tc99**	**I123**	**Tc99**	**Tc99**	**Tc99**	**Tc99**	**Tc99**	**Tc99**	**Tc99**	**Tc99**	**Tc99**	**Tc99**	**Tc99**	**Tc99**	**Tc99**	**Tc99**	**Tc99**	**Tc99**	**Tc99**	**Tc99**

References

[1] Nuclear Security Summit, (n.d.). http://www.nss2016.org/.

[2] L. Lakosi, N.C. Tam, J. Zsigrai, Revealing smuggled nuclear material covered by a legitimate radioisotope shipment using CdTe-based gamma-ray spectrometry, Appl. Radiat. Isot. 58 (2003) 263–267. doi:10.1016/S0969-8043(02)00314-7.

[3] V.D. Petrenko, Y.N. Karimov, A.I. Podkovirin, N.N. Shipilov, B.S. Yuldashev, M.I. Fazylov, Efforts of Uzbekistan to prevent nuclear terrorism and smuggling of radioactive and nuclear materials, Appl. Radiat. Isot. 63 (2005) 737–740. doi:10.1016/j.apradiso.2005.05.027.

[4] R. Lee, Why Nuclear Smuggling Matters, Orbis. 52 (2008) 434–444. doi:http://dx.doi.org/10.1016/j.orbis.2008.05.007.

[5] R.J. Pfaltzgraff, S. Eisenhower, A.J. Goodpaster, R.G. Card, D.C. Hintz, W.D. Magwood IV, A. Bugat, F.L. "Skip" Bowman, A.C. White, H.N. Wagner Jr, L.F. Brooks, L. Scheinman, P.M. Longsworth, P. Sewell, R.F. Lehman, R.L. Orbach, T.J. Symons, J.A. Bagger, M.S. Turner, A.A. Abrikosov, Nuclear Energy and Science for the 21st Century: Atoms for Peace Plus 50, 2004. http://www.ifpa.org/pdf/DOEFlet.pdf.

[6] IAEA, Iaea Incident and Trafficking Database (Itdb), (2015). http://www-ns.iaea.org/downloads/security/itdb-fact-sheet.pdf.

[7] W.J. Broad, Seismic Mystery in Australia: Quake, Meteor or Nuclear Blast?, New York Times. (1997). http://www.nytimes.com/1997/01/21/science/seismic-mystery-in-australia-quake-meteor-or-nuclear-blast.html?pagewanted=all.

[8] R. Mowatt-Larssen, Al Qaeda Weapons of Mass Destruction Threat : Hype or Reality ?, Harvard Univ. Belfer Cent. Sci. Int. Aff. (2010). http://belfercenter.ksg.harvard.edu/publication/19852/al_qaeda_weapons_of_mass_destruction_threat.html.

[9] IAEA, IAEA Safety Standards: National Strategy for Regaining Control over Orphan Sources and Improving Control over Vulnerable Sources for protecting people and the environment (No. SSG-19 Specific Safety Guide), 2011. http://www-pub.iaea.org/MTCD/Publications/PDF/Pub1510_web.pdf.

[10] BBC, "Dangerous" radioactive material stolen in Mexico, (2015). http://www.bbc.com/news/world-latin-america-32332271.

[11] BBC, Mexico radioactive material found, thieves' lives "in danger," (2013). http://www.bbc.com/news/world-latin-america-25224304.

[12] M. Castillo, Mexico issues alert after radioactive material stolen, CNN. (2016). http://www.cnn.com/2016/02/29/americas/mexico-radioactive-device-missing/.

[13] BBC, Iraq rebels "seize nuclear materials," (2014). http://www.bbc.com/news/world-middle-east-28240140.

[14] A. Rasheed, A. Mohammed, S. Kalin, Radioactive material stolen in Iraq raises security concerns, (2016). http://www.reuters.com/article/us-mideast-crisis-iraq-radiation-idUSKCN0VQ22F.

[15] M. Moran, C. Hobbs, Dirty bomb: Just how worried should we be as ISIS seeks ultimate threat?, (2015). http://www.cnn.com/2015/06/16/opinions/isis-dirty-bomb/.

[16] NNSA, Cooperative Border Monitoring Opportunities for the Global Partnership, (n.d.). http://www.state.gov/documents/organization/202455.pdf.

[17] Congress, SAFE Port Act, (2006). https://www.gpo.gov/fdsys/pkg/PLAW-109publ347/html/PLAW-109publ347.htm.

[18] NNSA, National Nuclear Security Administration Second Line of Defense MEGAPORTS INITIATIVE, (2010). http://nnsa.energy.gov/sites/default/files/nnsa/inlinefiles/singlepages_9-15-2010.pdf.

[19] PNNL, Radiation detectors at U.S. ports of entry now operate more effectively, efficiently, (2016). http://www.pnnl.gov/news/release.aspx?id=4245.

[20] J.L. Jones, D.R. Norman, K.J. Haskell, J.W. Sterbentz, W.Y. Yoon, S.M. Watson, J.T. Johnson, J.M. Zabriskie, B.D. Bennett, R.W. Watson, C.E. Moss, J.F. Harmon, Detection of shielded nuclear material in a cargo container, Nucl. Instruments Methods Phys. Res. Sect. a-Accelerators Spectrometers Detect. Assoc. Equip. 562 (2006) 1085–1088. doi:10.1016/j.nima.2006.02.101.

[21] P.E. Keller, R.T. Kouzes, Influence of Extraterrestrial Radiation on Radiation Portal Monitors, IEEE Trans. Nucl. Sci. 56 (2009) 1575–1583. doi:10.1109/TNS.2009.2019618.

[22] R.J. Livesay, C.S. Blessinger, T.F. Guzzardo, P.A. Hausladen, Rain-induced increase in background radiation detected by Radiation Portal Monitors *, J. Environ. Radioact. 137 (2014) 137–141. doi:10.1016/j.jenvrad.2014.07.010.

[23] R.T. Kouzes, J.R. Ely, A.T. Lintereur, D.L. Stephens, Neutron Detector Gamma Insensitivity Criteria. PNNL-18903, 2009.

[24] R.T. Kouzes, J.H. Ely, A.T. Lintereur, E.K. Mace, D.L. Stephens, M.L. Woodring, Neutron detection gamma ray sensitivity criteria, Nucl. Inst. Methods Phys. Res. A. 654 (2011) 412–416. doi:10.1016/j.nima.2011.07.030.

[25] C.A. Lo Presti, D.R. Weier, R.T. Kouzes, J.E. Schweppe, Baseline suppression of vehicle portal monitor gamma count profiles : A characterization study, Nucl. Instruments Methods Phys. Res. A. 562 (2006) 281–297. doi:10.1016/j.nima.2006.02.156.

[26] R.T. Kouzes, J.H. Ely, A. Seifert, E.R. Siciliano, D.R. Weier, L.K. Windsor, M.L. Woodring, J. Borgardt, E. Buckley, E. Flumerfelt, A. Oliveri, M. Salvitti, Cosmic-ray-induced ship-effect neutron measurements and implications for cargo scanning at borders,

Nucl. Instruments Methods Phys. Res. A. 587 (2008) 89–100. doi:10.1016/j.nima.2007.12.031.

[27] B.D. Geelhood, J.H. Ely, R.R. Hansen, R.T. Kouzes, J.E. Schweppe, R.A. Warner, Overview of Portal Monitoring at Border Crossings, in: Nucl. Sci. Symp. Conf. Rec. 2003 IEEE, 2004: pp. 513–517. doi:10.1109/NSSMIC.2003.1352095.

[28] R.T. Kouzes, J.H. Ely, B.D. Geelhood, R.R. Hansen, E.A. Lepel, J.E. Schweppe, E.R. Siciliano, D.J. Strom, R.A. Warner, Naturally occurring radioactive materials and medical isotopes at border crossings, in: Nucl. Sci. Symp. Conf. Rec. 2003 IEEE, 2003: pp. 1448–1452. doi:10.1109/NSSMIC.2003.1351967.

[29] IAEA, Naturally Occurring Radioactive Material, 2010. http://www-pub.iaea.org/MTCD/Publications/PDF/Pub1497_web.pdf.

[30] R.T. Kouzes, E.R. Siciliano, The response of radiation portal monitors to medical radionuclides at border crossings, Radiat. Meas. 41 (2006) 499–512. doi:10.1016/j.radmeas.2005.10.005.

[31] Ortec, Detective-SPM Systems High Purity Germanium Spectroscopic Radiation Portal Monitors, (n.d.). http://www.ortec-online.com/Solutions/CS-Portal.aspx.

[32] Symetrica, Discovery RPM radiation portal monitor, (n.d.). http://www.symetrica.com/rpm.

[33] D.C. Stromswold, J.W. Darkoch, J.H. Ely, R.R. Hansen, R.T. Kouzes, B.D. Milbrath, R.C. Runkle, W.A. Sliger, J.E. Smart, D.L. Stephens, L.C. Todd, M.L. Woodring, Field Tests of a NaI (Tl) -Based Vehicle Portal Monitor at Border Crossings, in: Nucl. Sci. Symp. Conf. Rec. 2004 IEEE, 2004: pp. 196–200. doi:10.1109/NSSMIC.2004.1462180.

[34] D.E. Sanger, Nuclear-Detection Effort Is Halted as Ineffective, New York Times. (2011). http://www.nytimes.com/2011/07/30/us/30nuke.html?_r=0.

[35] J. Ely, R. Kouzes, J. Schweppe, E. Siciliano, D. Strachan, D. Weier, The use of energy windowing to discriminate SNM from NORM in radiation portal monitors, Nucl. Instruments Methods Phys. Res. Sect. A Accel. Spectrometers, Detect. Assoc. Equip. 560 (2006) 373–387. doi:10.1016/j.nima.2006.01.053.

[36] R.T. Kouzes, A.T. Lintereur, E.R. Siciliano, Progress in alternative neutron detection to address the helium-3 shortage, Nucl. Instruments Methods Phys. Res. Sect. A Accel. Spectrometers, Detect. Assoc. Equip. 784 (2015) 172–175. doi:10.1016/j.nima.2014.10.046.

[37] R.T. Kouzes, J.H. Ely, L.E. Erikson, W.J. Kernan, A.T. Lintereur, E.R. Siciliano, D.L. Stephens, D.C. Stromswold, R.M. Van Ginhoven, M.L. Woodring, Neutron detection alternatives to 3He for national security applications, Nucl. Instruments Methods Phys. Res. A. 623 (2010) 1035–1045. doi:10.1016/j.nima.2010.08.021.

[38] ANSI, American National Standard for Evaluation and Performance of Radiation Detection Portal Monitors for Use in Homeland Security Accredited by the American

National Standards Institute, 2007.

[39] M.G. Paff, M.L. Ruch, A. Poitrasson-Riviere, A. Sagadevan, S.D. Clarke, S. Pozzi, Organic liquid scintillation detectors for on-the-fly neutron/gamma alarming and radionuclide identification in a pedestrian radiation portal monitor, Nucl. Inst. Methods Phys. Res. A. 789 (2015) 16–27. doi:10.1016/j.nima.2015.03.088.

[40] M. Ruch, M. Paff, A. Poitrasson-Riviere, A. Sagadevan, S.D. Clarke, S.A. Pozzi, P. Peerani, Large volume organic liquid scintillation detectors as a vehicle radiation portal monitor prototype at the 3rd SCINTILLA benchmark campaign, in: Proc. 56th Annu. Meet. Inst. Nucl. Mater. Manag. July 12-16, 2015, 2015.

[41] M. Paff, M. Ruch, A. Sagadevan, S.D. Clarke, S.A. Pozzi, P. Peerani, Performance of a EJ309 organic liquid scintillation detector pedestrian radiation portal monitor prototype at the 2nd SCINTILLA benchmark campaign, in: Proc. 55th Annu. Meet. Inst. Nucl. Mater. Manag. July 20-24, 2014, 2014.

[42] G.G. Knoll, Radiation Detection and Measurement, 4th ed., Wiley, 2010.

[43] M.L. Ruch, M. Flaska, S.A. Pozzi, Pulse shape discrimination performance of stilbene coupled to low-noise silicon photomultipliers, Nucl. Instruments Methods Phys. Res. Sect. A Accel. Spectrometers, Detect. Assoc. Equip. 793 (2015) 1–5. doi:10.1016/j.nima.2015.04.053.

[44] N.J. Cherepy, R.D. Sanner, P.R. Beck, E.L. Swanberg, T.M. Tillotson, S.A. Payne, C.R. Hurlbut, Bismuth- and lithium-loaded plastic scintillators for gamma and neutron detection, Nucl. Instruments Methods Phys. Res. Sect. a-Accelerators Spectrometers Detect. Assoc. Equip. 778 (2015) 126–132. doi:doi:10.1016/j.nima.2015.01.008.

[45] J. Dumazert, R. Coulon, G.H. V Bertrand, S. Normand, L. Méchin, M. Hamel, Compensated bismuth-loaded plastic scintillators for neutron detection using low-energy pseudo-spectroscopy, Nucl. Instruments Methods Phys. Res. A. 819 (2016) 25–32. doi:doi:10.1016/j.nima.2016.02.083.

[46] F.D. Brooks, A scintillation counter with neutron and gamma-ray discriminators, Nucl. Instruments Methods Phys. Res. Sect. a-Accelerators Spectrometers Detect. Assoc. Equip. 4 (1959) 151–163.

[47] L.M. Bollinger, G.E. Thomas, Measurement of the Time Dependence of Scintillation Intensity by a Delayed- Coincidence Method, Rev. Sci. Instrum. 32 (1961) 1044–1050. doi:10.1063/1.1717610.

[48] J.B. Birks, The Theory and Practice of Scintillation Counting, International Series of Monographs in Electronics and Instrumentation, 1964. doi:10.1016/B978-0-08-010472-0.50008-2.

[49] M.G. Paff, S.D. Clarke, S.A. Pozzi, Organic liquid scintillation detector shape and volume impact on radiation portal monitors, Nucl. Instruments Methods Phys. Res. Sect. A Accel. Spectrometers, Detect. Assoc. Equip. 825 (2016) 31–39. doi:10.1016/j.nima.2016.03.102.

[50] J.K. Polack, M. Flaska, A. Enqvist, C.S. Sosa, C.C. Lawrence, S.A. Pozzi, An algorithm for charge-integration, pulse-shape discrimination and estimation of neutron/photon misclassification in organic scintillators, Nucl. Instruments Methods Phys. Res. Sect. A Accel. Spectrometers, Detect. Assoc. Equip. 795 (2015) 253–267. doi:10.1016/j.nima.2015.05.048.

[51] N. Zaitseva, A. Glenn, L. Carman, H.P. Martinez, R. Hatarik, H. Klapper, S. Payne, Scintillation properties of solution-grown trans -stilbene single crystals, Nucl. Inst. Methods Phys. Res. A. 789 (2015) 8–15. doi:10.1016/j.nima.2015.03.090.

[52] N. Zaitseva, B.L. Rupert, I. Pawe, A. Glenn, H.P. Martinez, L. Carman, M. Faust, N. Cherepy, S. Payne, Plastic scintillators with efficient neutron / gamma pulse shape discrimination, Nucl. Inst. Methods Phys. Res. A. 668 (2012) 88–93. doi:10.1016/j.nima.2011.11.071.

[53] E. V Van Loef, G. Markosyan, U. Shirwadkar, K.S. Shah, Plastic Scintillators With Neutron / Gamma Pulse Shape Discrimination, IEEE Trans. Nucl. Sci. 61 (2014) 467–471. doi:10.1109/TNS.2013.2282079.

[54] U. Shirwadkar, E.V.D. Van Loef, G. Markosyan, J. Glodo, V. Biteman, A. Gueorguiev, K.S. Shah, S. Pozzi, S. Clarke, M. Bourne, New Generation Plastic Scintillators for Fast Neutron Spectroscopy and Pulse Shape Discrimination, IEEE Trans. Nucl. Sci. (2013) 1–4. doi:10.1109/NSSMIC.2013.6829469.

[55] ELJEN-TECHNOLOGY, NEUTRON/GAMMA PSD EJ-301, EJ-309, (n.d.). http://www.eljentechnology.com/index.php/products/liquid-scintillators/ej-301-ej-309 (accessed January 1, 2016).

[56] CAEN, 2016-2017 Product Catalog: CAEN Waveform Digitizers, (2016). http://www.caen.it/csite/CaenProfList.jsp?parent=360&Type=WOCateg&prodsupp=y (accessed January 1, 2016).

[57] D. Reilly, N. Ensslin, H. Smith Jr., S. Kreiner, Passive Nondestructive Assay of Nuclear Materials, U.S. Government Printing Office, Washington, D.C., 1991.

[58] S.A. Pozzi, E. Padovani, M. Marseguerra, MCNP-PoliMi: A Monte-Carlo code for correlation measurements, Nucl. Instruments Methods Phys. Res. Sect. A Accel. Spectrometers, Detect. Assoc. Equip. 513 (2003) 550–558. doi:10.1016/j.nima.2003.06.012.

[59] E.C. Miller, A. Poitrasson-Riviere, A. Enqvist, J.L. Dolan, S. Prasad, M.M. Bourne, K. Weinfurther, S.D. Clarke, MCNPX-PoliMi Post-Processor (MPPost) Manual, RSICC Package number C00791 MNYCP 00, (2012). www.rsicc.ornl.gov.

[60] S.A. Pozzi, M. Flaska, A. Enqvist, I. Paczit, Monte Carlo and analytical models of neutron detection with organic scintillation detectors, Nucl. Inst. Methods Phys. Res. A. 582 (2007) 629–637. doi:10.1016/j.nima.2007.08.246.

[61] C.C. Lawrence, M. Febbraro, T.N. Massey, M. Flaska, F.D. Becchetti, S. a. Pozzi,

Neutron response characterization for an EJ299-33 plastic scintillation detector, Nucl. Instruments Methods Phys. Res. Sect. A Accel. Spectrometers, Detect. Assoc. Equip. 759 (2014) 16–22. doi:10.1016/j.nima.2014.04.062.

[62] A. Enqvist, C.C. Lawrence, B.M. Wieger, S. a. Pozzi, T.N. Massey, Neutron light output response and resolution functions in EJ-309 liquid scintillation detectors, Nucl. Instruments Methods Phys. Res. Sect. A Accel. Spectrometers, Detect. Assoc. Equip. 715 (2013) 79–86. doi:10.1016/j.nima.2013.03.032.

[63] S. Nyibule, J. Tõke, E. Henry, W.U. Schröder, L. Acosta, L. Auditore, G. Cardella, E. De Filippo, L. Francalanza, S. Gianì, T. Minniti, E. Morgana, E.V. Pagano, S. Pirrone, G. Politi, L. Quattrocchi, P. Russotto, a. Trifirò, M. Trimarchi, Birks′ scaling of the particle light output functions for the EJ 299-33 plastic scintillator, Nucl. Instruments Methods Phys. Res. Sect. A Accel. Spectrometers, Detect. Assoc. Equip. 768 (2014) 141–145. doi:10.1016/j.nima.2014.09.056.

[64] R.M. Cibils, Sensitivity Enhancement in Radiation Portal Monitoring using Adaptive Matched Filtering, IEEE Trans. Nucl. Sci. 63 (2016) 1162–1168. doi:10.1109/TNS.2016.2524627.

[65] A. Sagadevan, M. Ruch, M.G. Paff, S.D. Clarke, S. a. Pozzi, Simulation of an EJ-309 Based Pedestrian Radiation Portal Monitor using MCNPX-PoliMi, in: Proc. 55th Annu. Meet. Inst. Nucl. Mater. Manag. July 20-24, 2014, 2014.

[66] M.G. Paff, S.D. Clarke, S.A. Pozzi, Optimization of organic liquid scintillation detectors in radiation portal monitor applications, in: IEEE Symp. Radiat. Meas. Appl. May 22-26, 2016, Berkeley, CA, USA, 2016.

[67] P. Schuster, E. Brubaker, Characterization of the scintillation anisotropy in crystalline stilbene scintillator detectors, Nucl. Instruments Methods Phys. Res. Sect. A Accel. Spectrometers, Detect. Assoc. Equip. (2016) 1–7. doi:10.1016/j.nima.2016.11.016.

[68] Motion-A Software Motion Detector, (n.d.). http://www.lavrsen.dk/foswiki/bin/view/Motion/WebHome (accessed January 1, 2016).

[69] A. Poitrasson-Rivière, M.C. Hamel, J.K. Polack, M. Flaska, S.D. Clarke, S.A. Pozzi, Dual-particle imaging system based on simultaneous detection of photon and neutron collision events, Nucl. Instruments Methods Phys. Res. Sect. A Accel. Spectrometers, Detect. Assoc. Equip. 760 (2014) 40–45. doi:10.1016/j.nima.2014.05.056.

[70] A. Poitrasson-Rivière, J.K. Polack, M.C. Hamel, D.D. Klemm, K. Ito, A.T. McSpaden, M. Flaska, S.D. Clarke, S.A. Pozzi, A. Tomanin, P. Peerani, Angular-resolution and material-characterization measurements for a dual-particle imaging system with mixed-oxide fuel, Nucl. Instruments Methods Phys. Res. Sect. A Accel. Spectrometers, Detect. Assoc. Equip. 797 (2015) 278–284. doi:10.1016/j.nima.2015.06.045.

[71] IAEA-TECDOC-1312: Detection of radioactive materials at borders, 2002.

[72] G. Eklund, P. Peerani, A. Thompson, Illicit Trafficking Radiation Assessment Program (

ITRAP + 10): Test Campaign Summary Report, 2016.

[73] SCINTILLA: Nuclear Detector Development and Benchmark, (2012). http://www.scintilla-project.eu/ (accessed January 1, 2016).

[74] Saphymo, (n.d.). http://www.saphymo.com/.

[75] E. Fanchini, Performance of an RPM based on Gd – lined plastic scintillator for neutron and gamma detection, in: IEEE Nucl. Sci. Symp. Conf. Rec., 2015.

[76] Symetrica, (n.d.). http://www.symetrica.com/.

[77] P. Peerani, A. Tomanin, G. Eklund, C. de Almeida Carrapico, F. Rosas, M. Caviglia, Third annual SCINTILLA benchmark report, Ispra, Italy, 2014.

[78] ORTEC, Experiment 7 High-Resolution Gamma-Ray Spectroscopy, (n.d.). http://www.ortec-online.com/Solutions/gamma-spectroscopy.aspx.

[79] D. Reilly, N. Ensslin, H. Smith Jr., S. Kreiner, LA-UR-90-732 Passive Nondestructive Assay of Nuclear Materials, 1991. http://www.lanl.gov/orgs/n/n1/panda/.

[80] M.L. Ruch, M. Paff, A. Sagadevan, S.D. Clarke, S.A. Pozzi, Radionuclide Identification by an EJ309 Organic Scintillator - Based Pedestrian Radiation Portal Monitor Using a Least Squares Algorithm, in: Proc. 55th Annu. Meet. Inst. Nucl. Mater. Manag. July 20-24, 2014, 2014.

[81] M.G. Paff, A. Di Fulvio, S.D. Clarke, S.A. Pozzi, Radionuclide identification algorithm for organic scintillator-based radiation portal monitor, Nucl. Instruments Methods Phys. Res. Sect. a-Accelerators Spectrometers Detect. Assoc. Equip. 849C (2017) 41–48. doi:http://dx.doi.org/10.1016/j.nima.2017.01.009.

[82] G.D. Bergland, A guided tour of the fast Fourier transform, IEEE Spectr. 6 (1969) 41–52. doi:10.1109/MSPEC.1969.5213896.

[83] F.A. Kruse, A.B. Lefkoff, J.W. Boardman, K.B. Heidebrecht, A.T. Shapiro, P.J. Barloon, A.F.H. Goetz, The Spectral Image Processing System (SIPS) Interactive Visualization and Analysis of Imaging Spectrometer Data, Remote Sens. Environ. 44 (1993) 145–163. doi:10.1016/0034-4257(93)90013-N.

[84] R.H. Yuhas, A.F.H. Goetz, J.W. Boardman, Discrimination among semi-arid landscape endmembers using the Spectral Angle Mapper (SAM) algorithm, in: JPL, Summ. Third Annu. JPL Airborne Geosci. Work. Vol. 1 AVIRIS Work., 1992: pp. 147–149. http://ntrs.nasa.gov/archive/nasa/casi.ntrs.nasa.gov/19940012238.pdf.

[85] Y. Sohn, N.S. Rebello, Supervised and unsupervised spectral angle classifiers, Photogramm. Eng. Remote Sensing. 68 (2002) 1271–1280.

[86] H. Yagoub, A.H. Belbachir, N. Benabadji, Detection and mapping vegetation cover based on the Spectral Angle Mapper algorithm using NOAA AVHRR data, Adv. Sp. Res. 53 (2014) 1686–1693. doi:10.1016/j.asr.2014.03.020.

[87] X. Zhang, P. Li, Lithological mapping from hyperspectral data by improved use of spectral angle mapper, Int. J. Appl. Earth Obs. Geoinf. 31 (2014) 95–109. doi:10.1016/j.jag.2014.03.007.

[88] E.L. Hunter, C.H. Power, An assessment of two classification methods for mapping Thames Estuary intertidal habitats using CASI data, Int. J. Remote Sens. 23 (2002) 2989–3008. doi:10.1080/01431160110075596.

[89] M.S. Bandstra, T.J. Aucott, E. Brubaker, D.H. Chivers, R.J. Cooper, J.C. Curtis, J.R. Davis, T.H. Joshi, J. Kua, R. Meyer, V. Negut, M. Quinlan, B.J. Quiter, S. Srinivasan, A. Zakhor, R. Zhang, K. Vetter, RadMAP: The Radiological Multi-sensor Analysis Platform, Nucl. Instruments Methods Phys. Res. Sect. A Accel. Spectrometers, Detect. Assoc. Equip. 840 (2016) 59–68. doi:10.1016/j.nima.2016.09.040.

[90] L. Caneve, F. Colao, R. Fantoni, L. Fiorani, Scanning lidar fluorosensor for remote diagnostic of surfaces, Nucl. Instruments Methods Phys. Res. Sect. A Accel. Spectrometers, Detect. Assoc. Equip. 720 (2013) 164–167. doi:10.1016/j.nima.2012.12.009.

[91] M. Sokolova, G. Lapalme, A systematic analysis of performance measures for classification tasks, Inf. Process. Manag. 45 (2009) 427–437. doi:10.1016/j.ipm.2009.03.002.

[92] J. Yang, Y. He, Automated mapping of impervious surfaces in urban and suburban areas : Linear spectral unmixing of high spatial resolution imagery, Int. J. Appl. Earth Obs. Geoinf. 54 (2017) 53–64. doi:http://dx.doi.org/10.1016/j.jag.2016.09.006.

[93] A. V Uhrin, P.A. Townsend, Estuarine , Coastal and Shelf Science Improved seagrass mapping using linear spectral unmixing of aerial photographs, Estuar. Coast. Shelf Sci. 171 (2016) 11–22. doi:http://dx.doi.org/10.1016/j.ecss.2016.01.021.

[94] D. Rommel, A. Grumpe, M. Patrik, C. Wöhler, U. Mall, A. Kronz, Automatic endmember selection and nonlinear spectral unmixing of Lunar analog minerals, Icarus. 284 (2017) 126–149. doi:http://dx.doi.org/10.1016/j.icarus.2016.10.029.

[95] A. Blake, The first Trump-Clinton presidential debate transcript, annotated, Washington Post. (2016). https://www.washingtonpost.com/news/the-fix/wp/2016/09/26/the-first-trump-clinton-presidential-debate-transcript-annotated/.

[96] S.A. Pozzi, M.M. Bourne, S.D. Clarke, Pulse shape discrimination in the plastic scintillator EJ-299-33, Nucl. Instruments Methods Phys. Res. Sect. A Accel. Spectrometers, Detect. Assoc. Equip. 723 (2013) 19–23. doi:10.1016/j.nima.2013.04.085.

[97] A. Chalupka, G. Stengl, H. Vonach, Temperature Dependence of the Pulse Shape Discrimination Properties Of NE 213, Nucl. Instruments Methods Phys. Res. Sect. a-Accelerators Spectrometers Detect. Assoc. Equip. 144 (1977) 167–169.

[98] D. Gehman, M. Smith-Nelson, K. Ianakiev, D. Dinwiddie, B. Rooney, Temperature Dependency Analysis of Light Output from an NE-213 Liquid Scintillator, in: IEEE Nucl.

Sci. Symp. Conf. Rec., 2007.

[99] M.M. Bourne, S.D. Clarke, M. Paff, A. DiFulvio, M. Norsworthy, S.A. Pozzi, Digital pile-up rejection for plutonium experiments with solution-grown stilbene, Nucl. Instruments Methods Phys. Res. Sect. A Accel. Spectrometers, Detect. Assoc. Equip. 842 (2017) 1–6. doi:10.1016/j.nima.2016.10.023.